Winter 1-15-2021

Multifunctional Polydopamine Nanomaterials for Biomedical and Environmental Applications

Hamed Gholami Derami
Washington University in St. Louis

WASHINGTON UNIVERSITY IN ST. LOUIS

Department of Mechanical Engineering and Materials Science

Dissertation Examination Committee:
Srikanth Singamaneni, Chair
Guy Genin
Mark Meacham
Barani Raman
Jonathan Silva

Multifunctional Polydopamine Nanomaterials for Biomedical and Environmental Applications

by

Hamed Gholami Derami

A dissertation presented to
The Graduate School
of Washington University in
partial fulfillment of the
requirements for the degree
of Doctor of Philosophy

January 2021
Saint Louis, Missouri

Table of Contents

List of Figures

List of Tables

List of Abbreviations

4-NP	4-Nitrophenol
AFM	Atomic force microscopy
APC	Antigen presenting cells
ATCC	American type culture collection
AuNPs	Gold nanoparticles
AuNRs	Gold nanorods
BET	Brunauer-Emmett-Teller
BMDC	Bone marrow derived dendritic cells
BNC	Bacterial nanocellulose
Cd	Cadmium
Cu	Copper
DIV	Days *in vitro*
DLS	Dynamic light scattering
E. coli	*Escherichia coli*
EPA	Environmental Protection Agency
FTIR	Fourier-transform infrared spectroscopy
GO	Graphene oxide
HRTEM	High Resolution Transmission Electron Microscopy
MB	Methylene blue
MEA	Microelectrode Array
MO	Methyl orange
mPDA	Mesoporous polydopamine
NIR	Near infrared
Pb	Lead

PBS	Phosphate-buffered saline
PDA	Polydopamine
PDMS	Polydimethylsiloxane
PdNPs	Palladium nanoparticles
PDT	Photodynamic therapy
PEI	Polyethylenimine
PET	Polyethylene terephthalate
Psi	Pound per square
PTT	Photothermal Therapy
R6G	Rhodamine 6G
RB	Rose Bengal
SEM	Scanning electron microscopy
SERS	Surface enhanced Raman scattering
TAA	Tumor-associated antigen
TD	Tetradecanol
TGA	Thermogravimetric analysis
TLR	Toll-like Receptor
UV-vis	Ultraviolet-visible
XPS	X-ray photoelectron spectroscopy
XRD	X-ray diffraction

Acknowledgments

First and foremost, I would like to thank my advisor Prof. Srikanth Singamaneni, without whom none of this would be possible. The dedication and passion I have seen from him during these years is unparalleled. His approach towards problems and scientific discoveries inspired me and motivated me to grow as a person and become a better researcher and more innovative thinker. I would also like to thank my PhD committee members Prof. Barani Raman, Prof. Guy Genin, Prof. Jonathan Silva, and Prof. Mark Meacham for their valuable advice, insightful comments, and inputs on my research.

I would like to thank all the previous and current members of the soft nanomaterials lab: Dr. Qisheng Jiang, Dr. Kengku Liu, Dr. Sirimuvva Tadepalli, Dr. Huzeyfe Yilmaz, Dr. Anushree Seth, Dr. Jingyi Luan, Mr. Prashant Gupta, Mr. Rohit Gupta, Ms. Priya Rathi, Ms. Lin Lin, Ms. Sisi Cao, Mr. Zheyu Wang, Ms. Ting Xu, Mr. Sang hyun Park, Ms. Emily Lu Wang, Mr. Sang hyun Bae, Mr. Abishek Venkatesan Iyer for being friendly and warming, to make our lab an enjoyable place to work in.

I want to thank the funding agencies, National Science Foundation (CBET-1604542) and Air Force Office of Scientific Research (Grant # FA95501910394), that provided financial support for my research.

Thank all my friends in St. Louis who I had some of the most memorable moments with them.

Special thanks to my parents, for their unconditional love and everything they have done for me throughout my life. Their sacrifices made it possible for me to beat the odds and go up the ladder. I am forever in their debt.

Finally, I would like to thank my wife, Mahsa Hajian. She was with me every step of the way, we endured hardships and enjoyed memorable moments, like when our son Ryan was born.

Hamed Gholami Derami

Washington University in St. Louis
January 2021

Dedicated to my parents, who made many sacrifices to help me to be where I am today. And to my wife Mahsa and my son Ryan who were beside me and motivated me throughout this journey.

Abstract of the Dissertation

Multifunctional Polydopamine Nanomaterials for Biomedical and Environmental Applications

by

Hamed Gholami Derami

Doctor of Philosophy in Mechanical Engineering and Materials Science

Washington University in St. Louis, 2020

Professor Srikanth Singamaneni, Chair

Polydopamine (PDA), a synthetic and organic material, has emerged as a promising material platform for various applications in energy, environmental, and biomedical fields. PDA, formed by self-polymerization of dopamine, is rich in catechol and amine groups, which facilitate covalent conjugation and/or other non-covalent interactions with organic and inorganic materials. It is highly biocompatible, biodegradable, has broadband light absorption spectrum and excellent light-to-heat conversion efficiency. Also, it is easy to synthesize and functionalize. The combination of excellent characteristics of polydopamine-based nanomaterials, make them a promising adsorbent agent for environmental wastewater treatment and photothermal agent for biomedical applications.

In the first half of thesis, we utilize the surface chemical functionality of polydopamine nanoparticles and their affinity to heavy metal ions and organic dyes to realize multifunctional filtration membranes that remove heavy metal ions and organic dyes from water through adsorption and catalytic degradation. Polydopamine exhibits high adsorption capacity toward heavy metal ions and organic dyes. Adsorption-based membrane technologies can be ideal for continuous flow water purification and have been extensively employed at industrial scale for

water reclamation. By introducing polydopamine nanoparticles during bacteria-mediated cellulose growth, we fabricated a composite foam and membrane to study the adsorption behavior of the nanocomposites in different environmentally relevant pH and concentrations. The PDA/BNC membrane was used to investigate the removal efficiency of toxic heavy metals ions such as Pb (II) and Cd (II) and organic pollutants such as rhodamine 6G and methylene blue. Furthermore, to improve the range of pH in which the composite membrane is effective for dye removal, we fabricated another novel polydopamine/nanocellulose membrane, which is decorated with palladium (Pd) nanoparticles to remove organic dyes from contaminated water through catalytic dye degradation.

In the second part of thesis, we develop polydopamine-based nanomaterials and experimental setups to be used in biomedical applications such as drug delivery and photothermal stimulation of cells. Using mesoporous silica-coated PDA nanoparticles as drug carrier and tetradecanol (TD) as gate keeper, we demonstrated that we could enhance the immune system response toward Melanoma cancer in mouse model through combination of photothermal and immunotherapy. Polydopamine core works as a photothermal agent to cause localized release of gardiquimod and tumor cell death upon NIR laser irradiation, hence, release of tumor associated antigens. Antigen presenting cells (APCs) including the dendritic cells and macrophages uptake these antigens and be activated around tumor site in response to these signals. Furthermore, these activated APCs, present the antigen to CD8+ cytotoxic T cells to actuate anti-tumor immune response. We have shown that this treatment is effective in reducing the tumor size and eliminating it in majority of cases. Also, the treatment created a memory effect in immune system toward melanoma cancer when second cancer event happened in mice that were treated before.

Finally, we investigated the possibility of controlling the excitable cells' activity through nanoheating. This was made possible by using polydopamine nanoparticles to localize the heat on cell membrane. We demonstrated that by using polydopamine nanoparticle and polydopamine/collagen 3D foam, and by applying NIR laser light, we can reversibly modulate the activity of in vitro cultured neurons and cardiomyocytes. A reduction in firing rate of neurons and an increase in beating rate of cardiomyocytes with different degree of inhibition and excitation was observed. Effect of different parameters on the quality of modulation was investigated.

Chapter 1: Background and Motivation

1.1 Polydopamine-Based Nanomaterials

Inspired by mussel's versatile adhesion capability, including surprisingly strong metal-binding ability, polydopamine has emerged as a promising material platform for various applications in energy, environmental, and biomedical fields.[1-4] Polydopamine, formed by self-polymerization of dopamine, is rich in catechol and amine groups, which facilitate covalent conjugation and/or other non-covalent interactions with organic and inorganic materials.[5-11] Polydopamine is biocompatible and biodegradable, which serves as a great material for reduction of waste in environmental applications. The applications of PDA coating onto various adsorbents, such as graphene, graphene oxide, glass beads, magnetic nanoparticles, and most recently, metal-organic frameworks, was shown to significantly improve their adsorption efficiency toward metal and organic contaminants.[12-16]

1.1.1 Polydopamine/Bacterial Nanocellulose Ultrafiltration Membrane for Adsorption-Based Wastewater Treatment

The growing world's population and socioeconomic development cause significant increase the demand for the fresh and clean water. The ever-growing industrialization around the world brings about more toxic heavy metals and organic contaminants into the natural water resources than ever.[17-19] In response to these impending challenges, various water remediation technologies based on adsorption, chemical precipitation, membrane filtration, and biological treatment have been used to remove contaminants from polluted water.[20-24] Among them, adsorption-based methods have been widely used for removing a variety of pollutants from water because they are simple, low-cost, effective and can be implemented in many parts of the

world.[20] Several different types of adsorbents, such as carbon-based materials, metal oxides, silica, and polymers have been shown to remove heavy metal ions and organic pollutants from contaminated water.[16, 20, 25-26] However, these adsorbents are mostly suitable for small-volume applications and are not compatible with continuous flow water treatment.[22] Alternatively, membrane technologies can be ideal for continuous flow water purification and have been extensively employed at industrial scale for water reclamation.[27-29] Thus, it is of great interest to develop novel adsorbent membranes that are cost-effective, robust and scalable.

1.1.2 Palladium Nanoparticle-Decorated Mesoporous-Polydopamine/Bacterial Nanocellulose Ultrafiltration Membrane for Catalytic Removal of Organic Dyes in Wastewater

Owing to the globally increasing demand for consumer goods, massive amounts of chemical wastes are produced and released into the environment by industries including textiles, paints, printing inks, cosmetics, plastics and paper.[30] These industrial effluents are highly contaminated by organic and inorganic compounds with textile wastewater being the most polluting among all industrial sectors.[31] Modern dyes, which are extensively used in many industries, offer superior color stability because of the high degree of aromaticity and extensive conjugation present in their chemical structures, which also make them harder to remove from water resources via traditional water treatment techniques.[32-33] Presence of these carcinogenic, mutagenic and persistent organic contaminants in natural environment, poses a great health risk for humans and aquatic ecosystems.[34-37] This greatly increases the need for the development of highly proficient and economical dye removal techniques from contaminated water.

Catalytic degradation of organic dyes by noble and transition metal nanostructures has been shown to be highly efficient and practical in water remediation in a wide range of environmental conditions.[38-43] To alleviate the aggregation of metal nanoparticles and achieve prolonged catalytic activity, immobilizing them on various substrates has been proven to be an attractive approach. A wide range of substrates such as polydopamine (PDA)-based nanoparticle, carbon-based nanoparticles, silica, and metal oxides have been employed for this purpose.[24, 44-52] Among these, PDA has emerged as a promising material platform for the development of catalytically-active substrates.[1, 48-49, 52] PDA nanoparticles and PDA-based materials were used as substrates for immobilization of different metals such as silver, gold, palladium and platinum.[48-50, 53] However, the use of these stand-alone catalytically active composite particles is highly limited for practical applications in industrial waste water treatment, due to their colloidal stability, which requires extra steps to remove them from water. One way to overcome this problem is to immobilize the metal nanoparticle on membranes for membrane filtration. However, achieving an ultrafiltration membrane with high water flux and excellent organic dye removal characteristics is still a challenge.

1.2 Photothermal Applications of Polydopamine-Based Nanomaterials

Among various nanomaterials that could transform light energy to heat, polydopamine (PDA) nanomaterials are a particularly promising candidate for photothermal neuronal modulation and cancer therapy due to their excellent photothermal properties, biocompatibility, biodegradability, and facile surface functionalization. [54] PDA-based nanomaterials have been widely investigated as photothermal agents for photothermal cancer therapy.[55-57] Furthermore, due to their

biocompatibility and superior interaction with cells, PDA-based nanomaterials have been shown to be promising candidates for neuronal interfacing. [58-60]

1.2.1 Mesoporous Silicon Oxide-Coated Polydopamine Nanoparticles as Drug Carrier and Photothermal Agent for Combined Photothermal-Immunotherapy Cancer Treatment

To achieve concurrent release of antigen and adjuvant by photothermally ablating the tumor cells for release of tumor associated antigens (TAAs) and simultaneously triggering the release of adjuvant, there is a need for a photothermally active material and a drug carrier. Recently, polydopamine has attracted increased attention as a bio-inspired, biocompatible, and biodegradable photothermal material for various biomedical applications.[1, 3, 61-65] Mesoporous silica, which is employed as shell, exhibits excellent biocompatibility, and complete degradation into non-toxic components making it an attractive candidate as a drug carrier.[66] Mesoporous silica-coated polydopamine nanoparticles could serve as a great drug delivery vehicle and photothermal agent for simultaneous photothermal and immunotherapy treatment.

1.2.2 Polydopamine Nanoparticles and Collagen/Polydopamine 3D Foam for Photothermal Stimulation of Excitable Cells

Among the many methods that aim to modulate the biological processes, a particularly attractive method is photo-regulation, a process in which light is utilized as an external stimulus.[67] Optogenetics, which involves the insertion of light-sensitive ion channels and subsequent stimulation of these neurons for selective control, has received wide attention.[68-69] While optogenetic techniques are promising and have revolutionized basic research aimed at understanding the computational and behavioral role of several different neural populations, there are still several limitations associated with these techniques that remain to be addressed.[70-

[72] To address some of these shortcomings, the use of nanomaterials for non-genetic electrical and thermal stimulation were explored and tested successfully in recent years.[73] Among these, photothermal methods have shown great promise and versatility in stimulating neuronal cells. [74-82] The use of thermal energy as a stimulus to activate neurons could be highly localized to avoid generic effects on neuronal firing and their behavior. Hence, there is a need for novel biocompatible nanomaterials to be used to interface them with excitable cells and are photothermally active to be used for photothermal stimulation of cells.

1.3 Research Goals and Objectives

The goal of this research effort is to synthesize multifunctional polydopamine (PDA) nanoparticles with well-defined structure and optical properties and to demonstrate their versatile applications in: (1) wastewater remediation; (2) combined photothermal and immunotherapy cancer treatment; (3) photothermal activity modulation of neuronal cells. Collectively, by demonstrating the multifunctional nature of the polydopamine nanomaterials and facile material synthesis, we have shown several potential applications that could take advantage of properties of this new class of organic material. We have accomplished several specific technical tasks noted below to realize these objectives:

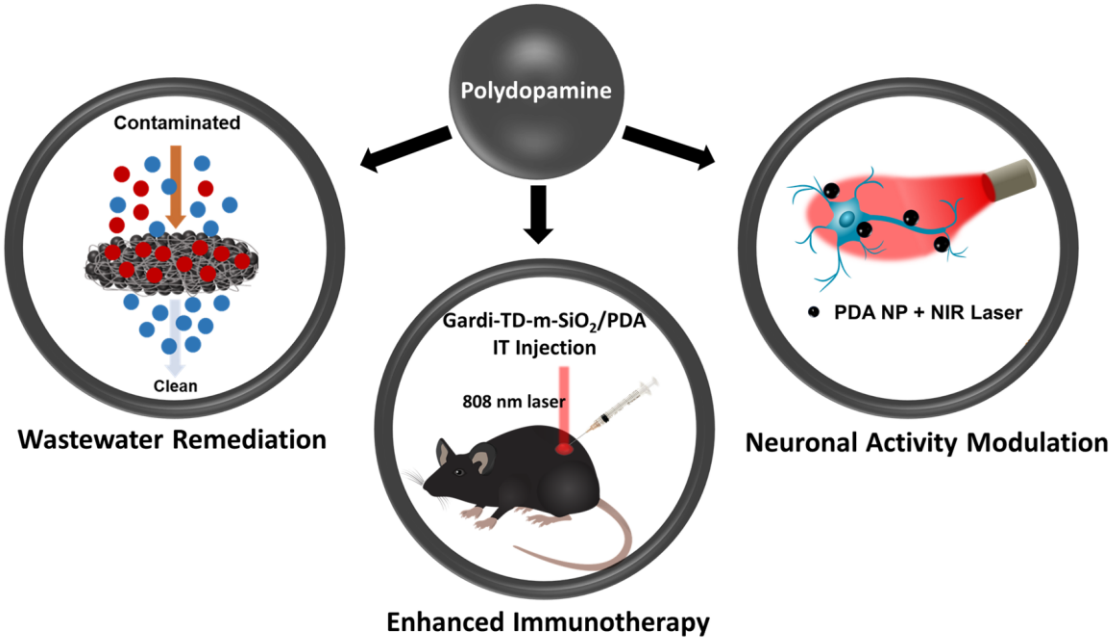

Figure 1.1 Schematic illustration of the overall research goal

1.3.1 Objective 1: Design, fabricate and validate PDA/ bacterial nanocellulose (BNC)-based functional composite membranes for efficient heavy metal ions and organic dyes removal from wastewater

Task 1: Investigate the contaminant removal capacity, water flux properties and the effect of pH and contaminant concentration on the adsorption properties of the PDA/BNC composite foam and membrane.

Task 2: Investigate the catalytic properties of palladium-decorated mesoporous-PDA/BNC membrane, the water flux and membrane's ability to remove organic dyes from wastewater.

1.3.2 Objective 2: Investigate NIR light-triggered photothermal therapy for improved cancer immunotherapy by using mesoporous silica-coated PDA nanoparticles

Task 1: Synthesize biocompatible mesoporous silica-coated PDA nanoparticles loaded with immuno-stimulating agent.

Task 2: Investigate anti-tumor response of photothermally-stimulated mesoporous silica-coated PDA particles loaded with TLR7/8 agonist using mouse melanoma model.

1.3.3 Objective 3: Harness the photothermal properties of PDA nanoparticles to control the electrical activity of neurons and cardiomyocytes *in vitro* locally and focally

Task 1: Devise an experimental setup to photothermally stimulate the primary neuronal cells and cardiomyocytes cultured on microelectrode arrays in presence of PDA nanoparticles using NIR light and investigate the nature of change in cells' activity.

Task 2: Develop a composite foam of collagen-PDA nanoparticle to be used as an add-on patch for photothermal activity modulation of excitable cells and compare its performance to PDA nanoparticle.

Chapter 2: A Robust and Scalable Polydopamine/Bacterial Nanocellulose Hybrid Membrane for Efficient Wastewater Treatment

2.1 Introduction

The growing world's population and socioeconomic development cause significant increase the demand for the fresh and clean water. The ever-growing industrialization around the world brings about more toxic heavy metals and organic contaminants into the natural water resources than ever.[17-19] In response to these impending challenges, various water remediation technologies based on adsorption, chemical precipitation, membrane filtration, and biological treatment have been used to remove contaminants from polluted water.[20-24] Among them, adsorption-based methods have been widely used for removing a variety of pollutants from water because they are simple, low-cost, effective and can be implemented in many parts of the world.[20] Several different types of adsorbents, such as carbon-based materials, metal oxides, silica, and polymers have been shown to remove heavy metal ions and organic pollutants from contaminated water.[16, 20, 25-26] However, these adsorbents are mostly suitable for small-volume applications and are not compatible with continuous flow water treatment.[22] Alternatively, membrane technologies can be ideal for continuous flow water purification and have been extensively employed at industrial scale for water reclamation.[27-29] Thus, it is of great interest to develop novel adsorbent membranes that are cost-effective, robust and scalable.

Inspired by mussel's versatile adhesion capability, including surprisingly strong metal-binding ability, polydopamine has emerged as a promising material platform for various applications in energy, environmental, and biomedical fields.[1-4] Polydopamine, formed by self-polymerization

of dopamine, is rich in catechol and amine groups, which facilitate covalent conjugation and/or other non-covalent interactions with organic and inorganic materials.[5-11] The applications of PDA coating onto various adsorbents, such as graphene, graphene oxide, glass beads, magnetic nanoparticles, and most recently, metal-organic frameworks, was shown to significantly improve their adsorption efficiency toward metal and organic contaminants.[12-16] In membrane technologies, dopamine coating on commercially available PET/PTFE composite membrane was used to improve the oil–water separation.[83] Due to excellent hydrophilicity of dopamine, it was used to modify the hydrophobic PVDF membranes to enhance the water flux and its antifouling performance.[84] Because of its photothermal ability, polydopamine coating was also used on commercial PVDF membranes to achieve localized heating under sunlight for photothermal membrane distillation.[85] Furthermore, it has been shown that PDA particles, as biocompatible materials could be used independently for a removal of heavy metals and organic contaminants with an outstanding efficiency.[20, 86] However, in those system, PDA particles which are dispersed in aqueous solution are barely reusable and difficult to collect. Thus, they are less likely to be suitable for real-world, large-scale applications. For this reason, designing an innovative and environmentally benign composite materials, immobilized PDA particles in foam or membrane structures, can be an attractive solution to ensure sustainable water treatment.

Bacterial nanocellulose is a highly attractive material for realizing multifunctional composites due to its outstanding mechanical strength, diverse chemical functionalization, facile synthesis, and excellent biocompatibility.[87-96] By introducing functional materials into the culture medium during bacteria-mediated BNC growth, scalable and robust functional composites can be achieved. Recently, we have demonstrated a novel, highly scalable and cost-effective strategy to realize BNC-based functional composites.[97-99]

Here, we report the fabrication approach of a low cost, scalable, environmentally friendly, and reusable composite membrane, which combines the mechanical robustness of BNC and the adsorption properties of PDA particles. Heavy metal ions such as lead and cadmium, along with surrogates of organic pollutants such as rhodamine 6G (R6G), methylene blue (MB), and methyl orange (MO) and combination of these pollutants can be efficiently removed from water by simple membrane filtration at a low vacuum pressure (0.7 bar). The novel membrane design introduced here suggest a promising approach for effective water remediation.

2.2 Results and Discussion

The PDA/BNC membrane is fabricated by the addition of PDA particles into *Gluconacetobacter hansenii* broth under aerobic and static conditions (Figure 2.1). PDA particles are synthesized by self-polymerization and air-oxidation of dopamine monomer in water-ethanol-ammonium mixture at room temperature (Figure 2.2A).[10] The size of the PDA particles can be controlled by varying the amount of ammonium present in the reaction solution, with a higher amount of ammonium resulting in smaller particles. Optimal PDA particle size is critical for efficient incorporation of the particles in the BNC fiber network and fabrication of uniform PDA/BNC hybrid composites. Smaller particles leach out of the BNC network easily under operational conditions, which compromises the adsorption efficiency of the membrane and causes unintended contamination of the permeate water. Scanning electron microscopy (SEM) images showed that the PDA particles are spherical and highly uniform with a diameter around 800 nm (Figure 2.2B). The Raman spectrum of PDA particles exhibited two broad bands at 1371 cm^{-1} and 1578 cm^{-1} corresponding to the characteristic aromatic groups of polydopamine, confirming the formation of PDA particles (Figure S2.1).[100] Fourier transform infrared (FTIR) spectrum of the PDA particles showed a broad adsorption band at 3341 cm^{-1}, corresponding to the O–H and

N–H stretching vibrations of catechol group of the PDA (Figure 2.2C).[101] The absorption peak at 1610 cm^{-1} can be attributed to the bending ring vibration of N–H and stretching vibration of aromatic ring, the peak at 1516 cm^{-1} corresponds to shearing vibration of amide group, and the peak at 1290 cm^{-1} corresponds to C-O stretching.[102-103]

The as-produced PDA/BNC hydrogels were either freeze-dried to form foams for adsorption experiments in batch reactors or air-dried to form membranes for flow-through filtration tests. The thickness of the PDA/BNC foam was tuned by simply controlling the duration of the bacterial growth process. The typical thickness of the PDA/BNC foams used in this study was ~1.1 mm (Figure 2.2D). Pristine BNC foam, comprised of an entangled network of nanocellulose fibers with diameters 20–100 nm, exhibited a porous microstructure, while the air-dried BNC membrane showed a compact structure of cellulose fibers (Figure S2.2 and S2.3). We hypothesized that the fibrous network of the BNC matrix can effectively trap 800 nm PDA. Growth of BNC in the presence of PDA particles resulted in high density and uniform distribution of PDA particles inside the BNC fiber network, which is important for reliable and consistent performance of the membrane (Figure 2.2E and F). When the PDA/BNC hydrogels were air-dried, the cellulose fibers and PDA particles were packed into a thin and dense film with a thickness of ~50 μm (Figure 2.2G and I). Figure 2H shows that a few layers of BNC fibers on the surface of the membrane effectively trap PDA particles and prevent them from leaching out of the membrane.

Thermogravimetric analysis (TGA) was used to measure the PDA loading of the PDA/BNC composite. TGA was performed in nitrogen using a TA Instruments Q5000 IR Thermogravimetric Analyzer at a heating rate of 5 ºC min^{-1}. Around 57 % residual weight of PDA was observed after heating to 800°C under Nitrogen. Pristine BNC film showed an initial

mass loss (2–3%) at 100 °C, which is attributed to the loss of residual/adsorbed water, a mass loss (~70%) at ~280 °C is due to the degradation of cellulose and a mass loss (~25%) at ~390 °C is due to the decomposition of cellulose residual, which generates CO_2 and H_2O.[104] In the case of PDA/BNC, the initial mass loss (~8 %) at ~100 °C is due to the loss of residual water. The second mass loss (~30%) at 280 °C is due to the degradation of cellulose and the degradation of PDA particles. After heating to 800 °C, 33% of initial weight of PDA/BNC membrane remained. Based on TGA results, the mass loading of PDA in PDA/BNC is calculated to be ~ 44 wt% (Figure S2.4).

To study the adsorption behaviors of PDA/BNC composites, we performed batch adsorption tests using heavy metal ions and organic dyes (Figure 2.3A). Pb (II) was selected as a model heavy metal ion. In this experiment, the initial pollutant concentration and pH were adjusted and then PDA/BNC or BNC (control) foam was weighed and placed in the known volume of the pollutant solution. The adsorbent was left under gentle shaking until it reached equilibrium condition. Subsequently, pollutant concentrations in the solution were measured to calculate the adsorption capacity. The solution pH affects the surface potential (zeta-potential) of the PDA particles and BNC, thereby changing their adsorption behaviors. In our experimental systems, the isoelectric point (pH_{iep}) of BNC and PDA particles was found to be 2.4 and 3.3, respectively (Figure 2.3B), and the zeta-potential of BNC and PDA particles decreased with an increase in the pH of the solution.

Specifically, the adsorption capacity of BNC and PDA/BNC foams for Pb (II) increased with the pH increased (Figure 2.3C). At pH values below pH_{iep}, the positively charged surface repels the positively charged Pb (II) ions, and hence, lower adsorption capacities were observed at pH < 3

(Figure 2.3C). At pH values above pH_{iep}, the surface of the adsorbent is negatively charged because of the ionization of oxygen-bearing functional groups on the surface. Negatively charged surface provides favorable interactions for adsorption of Pb (II) ions. The adsorption capacity was found to significantly increase for both BNC and PDA/BNC foams at pH values above their isoelectric point and below pH 6 (Figure 2.3C). At pH > 6, hydrolysis of the Pb (II) ions possibly transforms them into metal hydroxides and result in precipitation.[105] The adsorption capacities of BNC and PDA/BNC foams were acquired at pH 6. Upon increasing the Pb (II) ion concentrations, the adsorption capacity for both BNC and PDA/BNC foams increased until they reach a saturation point (Figure 2.3D). Incorporation of PDA particles in the BNC matrix significantly increased the Pb (II) adsorption capacity of the composite from 5 mg g^{-1} for BNC to 16.8 mg g^{-1} for PDA/BNC. This could be mainly due to the presence of active catecholamine functional groups on the PDA surface and their strong affinity to heavy metals.[20] The XPS spectra of the PDA/BNC before and after the adsorption were used to confirm the adsorption of the Pb (II) ions and their interactions with the adsorbents (Figure S2.5). The C 1s, N 1s, and O 2p peaks at ~285.2 eV, ~398.4 eV and ~531.7 eV, respectively, correspond to the elemental composition of PDA/BNC before the adsorption (N 1s spectrum comes from PDA only). The presence of Pb 4f binding energy peak (at 137.4 eV and 142.3 eV) after exposure to Pb salt solution confirmed the successful Pb (II) adsorption onto the PDA/BNC. The Pb 4f spectrum for lead (II) nitrate exhibits two peaks at 138.1 eV and 143 eV (Figure S2.5B). Upon its adsorption onto PDA/BNC, the two peaks shifted to lower energy levels by 0.7 eV, suggesting the reaction of Pb (II) and phenolic groups on the surface of the PDA (Figure S2.5C).[16] Furthermore, we compared the PDA particle's ability to remove Pb (II) with that of activated carbon, which is one of the most commonly used adsorbents (Figure S2.6). The PDA

particles showed 77% higher adsorption capacity compared to activated carbon for lead ions when normalized by the weight of the adsorbents. Although the specific surface area of PDA particles (1446 m^2 g^{-1}) is lower than that of the activated carbon (1594 m^2 g^{-1}), interestingly, PDA particles exhibited superior Pb (II) adsorption capacity compared to activated carbon. These observations indicate the better affinity of the lead ions to the PDA particles over activated carbon, possibly due to the presence of catecholamine groups on the PDA surface.[20]

To examine the organic pollutant removal efficiency of the PDA/BNC foam, R6G was employed as a model positively charged organic contaminant. Over a pH range of 2 to 8, the adsorption capacity of both BNC and PDA/BNC increased with an increase of the pH (Figure 2.4A). With an increase in pH of the solution, the adsorbent surface is more negatively charged and results in higher adsorption of the positively charged dye (R6G). However, above pH 7 due to deprotonation of amine groups of the dye, the interaction weakens, and the adsorption capacity decreases. We tested the adsorption capacity of BNC and PDA/BNC foams at different initial concentrations of R6G at pH 7 (Figure 2.4B). The adsorption capacity for both foams increased with an increase in the concentration of the dye until it reached a saturation point. PDA/BNC showed improved performance with a maximum adsorption capacity of 8.7 mg g^{-1} compared to BNC (1.8 mg g^{-1}). The superior performance by PDA/BNC may be related to the π-π interactions between aromatic moieties of PDA and R6G along with the hydrogen-bonding interactions between catecholamine groups on PDA and amine groups of the R6G.[106]

To analyze the nature of adsorption of heavy metal ions and organic pollutants, the experimental data were fitted using the following Langmuir adsorption isotherm (Equation 2.1).

$$q_e = \frac{Q_{max} C_e}{(1/K_L) + C_e} \quad (2.1)$$

Where q_e is the adsorption capacity (mg g^{-1}) corresponding to equilibrium concentration, C_e (mg L^{-1}). Q_{max} is the maximum uptake (mg g^{-1}), and K_L is the binding constant (L g^{-1}). The fitting parameters corresponding to these curves are provided in Table S1 in supporting information. For both Pb (II) and R6G, the Langmuir model describes the adsorption behavior quite well (R^2>0.97), suggesting that the adsorption of lead ions and R6G occurred on the functional groups on the surface of the adsorbents in a monolayer manner.[16]

Considering that the PDA/BNC foam exhibited high efficiency in adsorbing heavy metal ions and organic dye, we set out to investigate the performance of PDA/BNC as a filtration membrane for continuous and rapid removal of contaminants in feed water (Figure 2.5A). Membranes obtained through air-drying of the PDA/BNC hydrogel were cut into circular pieces with a diameter of 3 cm. The membranes were fixed on a vacuum filtration setup and a vacuum pressure of 0.7 bar was applied. Typical metal ion pollutants (i.e., Pb (II) and Cd (II)) along with organic dyes (i.e., R6G, MB, and MO) were used in membrane filtration tests. The concentration of the pollutants in the feed water was adjusted to match that of polluted water sources and the pH of water was adjusted to match the optimum performance of the membrane for each pollutant (as determined from the batch adsorption measurements, see Figure S2.7 for optimum pH value for Cd (II) and MB). The experiments with pristine BNC membranes did not generate any flow at 0.7 bar (vacuum) due to the small pore size of the BNC membrane. Therefore, no vacuum filtration data was obtained for BNC membrane. Impregnating the BNC matrix with PDA particles, provided additional nanochannels for water to pass through the

membrane. This in turn, enabled filtration with water flux reaching 57 L m^{-2} hr^{-1} at 0.7 bar (10 psi) vacuum pressure (water inlet pressure at the kitchen faucet: 25–75 psi). To measure the upper and lower limits of the pore sizes of the BNC membrane, we performed diffusion test with DL-Tryptophan, R6G, and lysozyme. Within the observation time (5 hours), all of them diffused through the BNC membrane showing that pore size for BNC membrane is larger than ~ 1 nm (Figure S2.8A). To determine the upper limit of the pore size for BNC membrane, diffusion test was performed by using gold nanoparticles (AuNPs) with a diameter of 5 nm. After 24 hours, no AuNP was found on the permeate side, indicating that the pore size for the BNC membrane is less than 5 nm (Figure S2.8A). For PDA/BNC membrane, vacuum filtration at 0.7 bar pressure was used to filter the colloidal solution of 5 nm and 10 nm AuNPs (Figure S2.8B). As evident from the extinction spectrum, 5 nm AuNPs penetrate through the membrane, but 10 nm AuNPs are blocked from passing through the membrane even after 4 hours of filtration. These results indicate the upper limit of the pore size of PDA/BNC to be 10 nm, which is higher than that noted for BNC membranes.

The first heavy metal pollutant tested was Pb (II) with an initial concentration of 58 ppm and pH adjusted to 6. The permeate water concentration was measured repeatedly and the experiment was carried out until a detectable amount of Pb (II) was observed on the permeate side (Figure 2.5B). The Pb (II) concentration in the feed and permeate was determined using inductively coupled plasma optical emission spectrometry (ICP-OES) with a detection limit of 50 ppb. A total amount of 225 ml of 58 ppm Pb (II) aqueous solution was filtered through the membrane with undetectable levels of Pb (II) on the permeate side. The filtration test was carried out for Cd (II) solution with initial concentration of 50 ppm and a total amount of 125 ml was filtered to

a concentration below the limit of the detection of the ICP-OES (Figure 2.5C). The PDA/BNC membrane showed superior performance in removing Pb (II) solution compared to Cd (II).

Furthermore, after each filtration test of heavy metal ions, the PDA/BNC membranes were regenerated to recover their heavy metal ions removal efficiency (inset of Figure 2.5B). Aqueous sodium citrate (0.1 M) solution was employed for regenerating the membrane. Note that sodium citrate is a mild regeneration agent compared to the typically employed strong acids, necessitating multiple wash steps for complete regeneration. The use of such mild regeneration agent preserves the membrane integrity and extends the lifetime of the membrane for repeated use. The regenerated membranes exhibited excellent contaminant removal efficiency even after 10 cycles of filtration (about 90% of the initial performance retained).

For organic pollutants, the initial concentration for each pollutant was adjusted to mimic industrial wastewater source.[22] For R6G and MB as model positively charged dyes, the initial pH was adjusted to 7 and 10, respectively (Figure S2.9A for chemical structure of the dyes). In case of R6G, 105 ml of dye solution was filtered from 51 ppm to below 0.05 ppm (Figure 2.6A). For MB, 120 ml solution with initial concentration of 47 ppm was filtered to a concentration below 0.05 ppm (Figure 2.6B). The last organic pollutant tested was MO as model negatively charged dye (Figure S2.10). At pH 7, it was observed that no MO dye was removed from the water because of the electrostatic repulsion between negatively charged dye and negatively charged membrane. Then, the initial pH value for MO solution was adjusted to ~2.4 for filtration purpose. At this pH, only 25 ml of MO solution with an initial concentration of 55 ppm was filtered with high efficiency (Figure S2.10A). The filtration performance for MO was significantly lower than R6G and MB, suggesting that PDA/BNC membrane, and generally PDA-based adsorbents, are not suitable choices for removing negatively charged pollutants. To

demonstrate the reusability of the membranes, after R6G filtration, the membrane was regenerated using ethanol. The PDA/BNC membrane retained more than 90% of its R6G removal capacity after 10 cycles of filtration and regeneration (inset of Figure 2.6A).

To investigate the versatility of the PDA/BNC membrane when exposed to feed water with multiple contaminants, an inorganic–organic mixed solution of Pb (II), Cd (II), R6G, and MB was prepared and filtered through the PDA/BNC membrane. In this competitive adsorption test, the PDA/BNC membrane removed 5.3 g of Pb (II) from water per square meter of the membrane area (Figure 2.6C). The lowest performance was observed for Cd (II) with 2.1 g of ions removed per square meter of the membrane area, which might be because of lower binding affinity of Cd (II) to carboxylic and phenolic groups compared to lead ions.[107] Organic dyes were also effectively removed from the mixture with total removal capacity of 4.3 g m^{-2} and 3.8 g m^{-2} for R6G and MB, respectively. The strongly green colored cocktail solution became completely colorless after the vacuum filtration demonstrating an efficient filtration process with only a single run (Figure 2.6D and Figure S2.9B). To put this into perspective, 5300 L of water contaminated with lead ions at a concentration of 1 ppm (much higher than EPA recommended safe level of 15 ppb) could be filtered to a safe concentration by using PDA/BNC membrane of 1×1 m^2.

The mechanical stability of the PDA/BNC membrane was investigated by subjecting it to extensive sonication (Cole-Parmer ultrasonic cleaner #8890, 5 hours) and agitation (speed 3 on standard analog shaker, 30 days). The membrane did not exhibit noticeable signs of disintegration or loss of PDA particles from the BNC matrix after the shaking and sonication process (Figure 2.7A). The *in situ* fabrication method adopted here allowed for up to 44 wt% loading of the PDA particles inside the BNC network (Figure 2.7B, detailed thermogravimetric

analysis (TGA) is provided in the supporting information). TGA of the PDA/BNC membrane after sonication (5 hours), demonstrated no discernible change in the weight fraction of the PDA particles inside the PDA/BNC composite, suggesting the high mechanical integrity of the membrane (Figure 2.7B). The absorption spectrum of the bath solution in which PDA/BNC membrane was submerged during 5 hours of sonication did not exhibit light absorption corresponding to the PDA particles, further confirming the high mechanical stability of the PDA/BNC membranes and negligible amount of particle leaching (Figure 2.7C). SEM images of the membrane before and after the sonication exhibited no perceivable change in the structure of the PDA/BNC membrane (Figure 2.7D). Overall, the stability tests proved the excellent mechanical stability of the membranes, which is critical for their real-world applications. The performance of the membrane before and after the stability test was investigated using 100 ppm R6G as feed solution at pH 7. The PDA/BNC membrane retained 81% of its initial efficiency in removing the pollutants. We also noted a ~10% increase in water flux, possibly due to small structural changes that could not be perceived with SEM imaging. While there is a noticeable change in the membrane performance, it is important to note that the stability test performed here is quite harsh and represents an accelerated form of real-world application of the membrane.

2.3 Conclusion

To summarize, we introduced a novel PDA/BNC composite adsorption membrane which has potential to treat wastewater containing multiple inorganic and organic pollutants. The PDA/BNC membrane is fabricated by incorporating high density PDA particles inside BNC matrix during its growth. This fabrication technique is highly versatile and can be easily adapted to incorporate other adsorbents. All the materials used in the membrane fabrication process are biocompatible and biodegradable. The unique fabrication process resulted in a highly uniform

distribution of PDA particles within the BNC matrix. The highly flexible thin film PDA/BNC membrane exhibited excellent aqueous stability and fast water transport (57 L m^{-2} hr^{-1} under 10 psi). The PDA/BNC membrane showed effective contaminant removal from feed water containing heavy metal ions and positively charged organic dyes at high concentrations (40–60 ppm). The membrane was found to be equally effective in removing either a single pollutant or pollutant cocktail (the concentrations of contaminants in permeate side decreased to less than 0.05 ppm). The PDA/BNC membrane can also be regenerated easily and reused for several times without a significant degradation in its adsorption capacity. The facile, inexpensive, and scalable synthesis, excellent mechanical robustness and highly efficient removal of heavy metals and organic dyes under complex conditions and the ability to modify the PDA surface for variety of water treatment systems, collectively make PDA/BNC membrane demonstrated here a promising and powerful candidate for wastewater treatment.

2.4 Experimental Section

Sample Preparation: All chemicals were purchased from Millipore Sigma, St. Louis, USA and used without further modification. Polydopamine particles were synthesized by using a method explained elsewhere.[10] In a typical synthesis procedure of polydopamine particles, 252 ml of deionized (DI) water (resistivity > 18.2 MΩ·cm) was mixed with 112 ml of ethanol in a 1000 ml glass container. Subsequently, 1.12 ml of aqueous solution of ammonia (28–30% NH_4OH) was introduced into the above water/ethanol mixture. After stirring for 30 min, the aqueous solution of dopamine hydrochloride (1.4 g in 28 ml) was added to the above solution. The reaction was left under gentle magnetic stirring for 24 hours with no cap on the glass container. The PDA particles were collected by centrifugation (7000 rpm, 10 min) and washed with DI water three times and dispersed in water (320 ml).

A fabrication technique that we introduced in our previous work was used with some modifications to synthesize the PDA/BNC composite.[108] Bacterium *Gluconacetobacter hansenii* (ATCC®53582) was cultured in test tubes containing 16 ml of #1765 medium at 30 °C under shaking at 250 rpm. The #1765 medium is composed of 2 % (w/v) glucose, 0.5 % (w/v) yeast extract, 0.5 % (w/v) peptone, 0.27 % (w/v) disodium phosphate, and 0.5 % (w/v) citric acid. PDA particle solution (160 ml) was centrifuged, and the pellets were dispersed in the mixture of bacterial culture solution and the bacterial growth solution (1.5 ml and 13.5 ml, respectively). This mixture was then transferred to a petri dish (6 cm diameter). After 1-2 hours that the PDA particles precipitated at the bottom of the petri dish, the excess culture solution was removed. Two days later, a thin uniform layer of PDA-filled BNC was formed. The PDA/BNC hydrogel was collected and washed in boiling water for 2 hours, then dialyzed in DI water for one day. Then, the PDA/BNC hydrogels were either freeze-dried for batch adsorption tests or air-dried for filtration tests. The PDA/BNC fabrication process relies on PDA particles to completely settle down during the first 1-2 hours of the growth process. Hence, particles with the size around 800 nm, that settle down in less than 1 hour were synthesized to incorporate into BNC matrix.

Materials Characterization: Scanning electron microscope (SEM) images were obtained by using a JEOL JSM-7001 LVF Field Emission SEM. Zeta potential measurements were performed using Malvern Zetasizer (Nano ZS). Shimadzu UV-1800 spectrophotometer was employed for light absorption measurements. Raman spectra were obtained using a Renishaw inVia confocal Raman spectrometer mounted on a Leica microscope with 20× objective and 785 nm wavelength diode laser as an illumination source. Versa Probe II X-Ray Photoelectron Spectrometer (XPS) was used to acquire XPS spectra. Fourier-transform infrared (FTIR) spectrum was obtained on Nicolet 470 (Thermo Scientific). The specific surface area was

estimated from nitrogen adsorption/desorption isotherms by using Brunauer–Emmett–Teller (BET) method and a surface area analyzer (Autosorb-1C).

Batch Adsorption Experiments: To evaluate the adsorption behavior of PDA/BNC, batch adsorption tests were conducted at room temperature. To investigate the effect of pH, a small piece of PDA/BNC foam was placed in 5 ml solution of each pollutant and left shaking until it reached equilibrium. For heavy metals, pH values from 2 to 6 and for organic pollutants pH values from 2 to 10 were tested. The solution pH was controlled by adding HCl and NaOH to original solutions. At an optimum pH value for each pollutant, PDA/BNC foam was immersed into solutions with different initial concentrations and left shaking to reach equilibrium. For R6G, methyl orange and methylene blue, UV-vis absorption spectroscopy is used to measure the concentrations before and after the adsorption. Then, an Inductively coupled plasma-optical emission spectroscope (ICP-OES PE Optima 7300DV) was utilized to evaluate the heavy metal concentrations. To compare the PDA with a commonly used adsorbate such as activated carbon, similar weight of each absorbent was added into 15 ml of 200 ppm Pb (II) solution in a glass vial. Glass vials were subjected to mild shaking for a day, and Pb (II) concentrations before and after the test were measured. The removal capacity (q) for each pollutant was calculated by the equation below.

$$q = \frac{(C - C_o)V}{m} \tag{2.2}$$

where, C and C_0 are the initial and final concentration of the pollutant (in ppm), respectively, V is the volume of the contaminated water used (in L) and m is the weight of adsorbents (in gram). Each experiment was replicated three times and error bar for each data point shows the standard deviation of these three runs.

Membrane Filtration Experiments: Filtration experiments were carried out by using a vacuum filtration setup. A concentration of each pollutant was prepared, and the pH was adjusted to the corresponding optimal pH value for each pollutant. At typical pressure of 0.7 bar, vacuum filtration was performed in wet state, until the concentration of the filtered water for each pollutant exceeded the limit of detection of the corresponding measuring system. All the membranes used in vacuum filtration had 3 cm diameter. Then, membrane was regenerated using ethanol for organic dyes and 0.1 M sodium citrate solution for heavy metals. After each filtration test, the membrane was regenerated by placing it in the washing solution and shaking it for 2 hours for each washing cycle. The washing solution was measured each time to estimate the amount of regenerated pollutants. Washing cycles were continued until no pollutant was observed in the washing solution.

2.5 Supporting Information

Supporting Information for chapter 2 is provided in appendix 1.

2.6 Figures

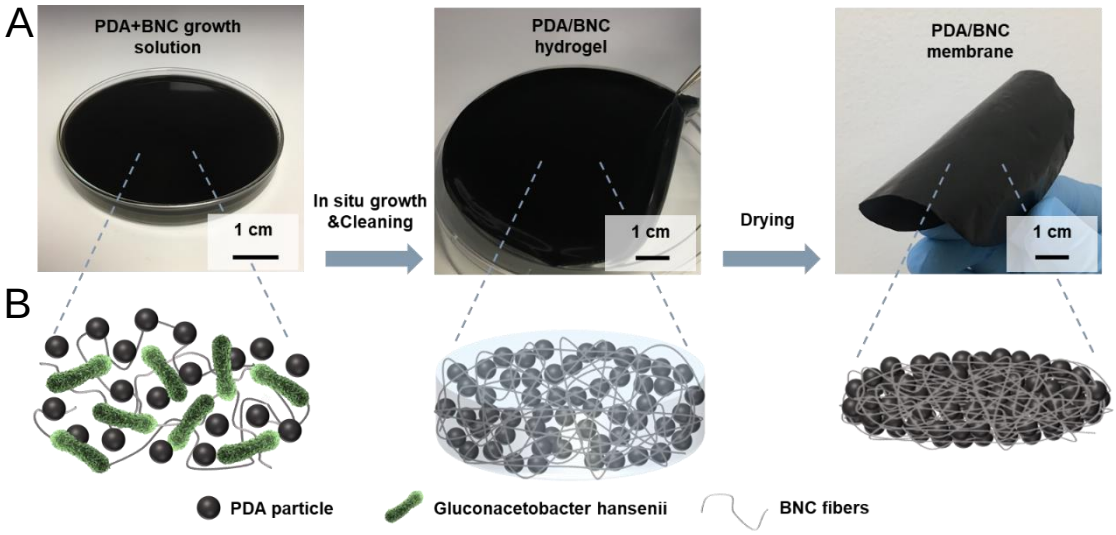

Figure 2. 1 (A) Photographs of PDA/BNC membrane during different fabrication steps. (B) Schematic representation of the fabrication process of PDA/BNC membrane.

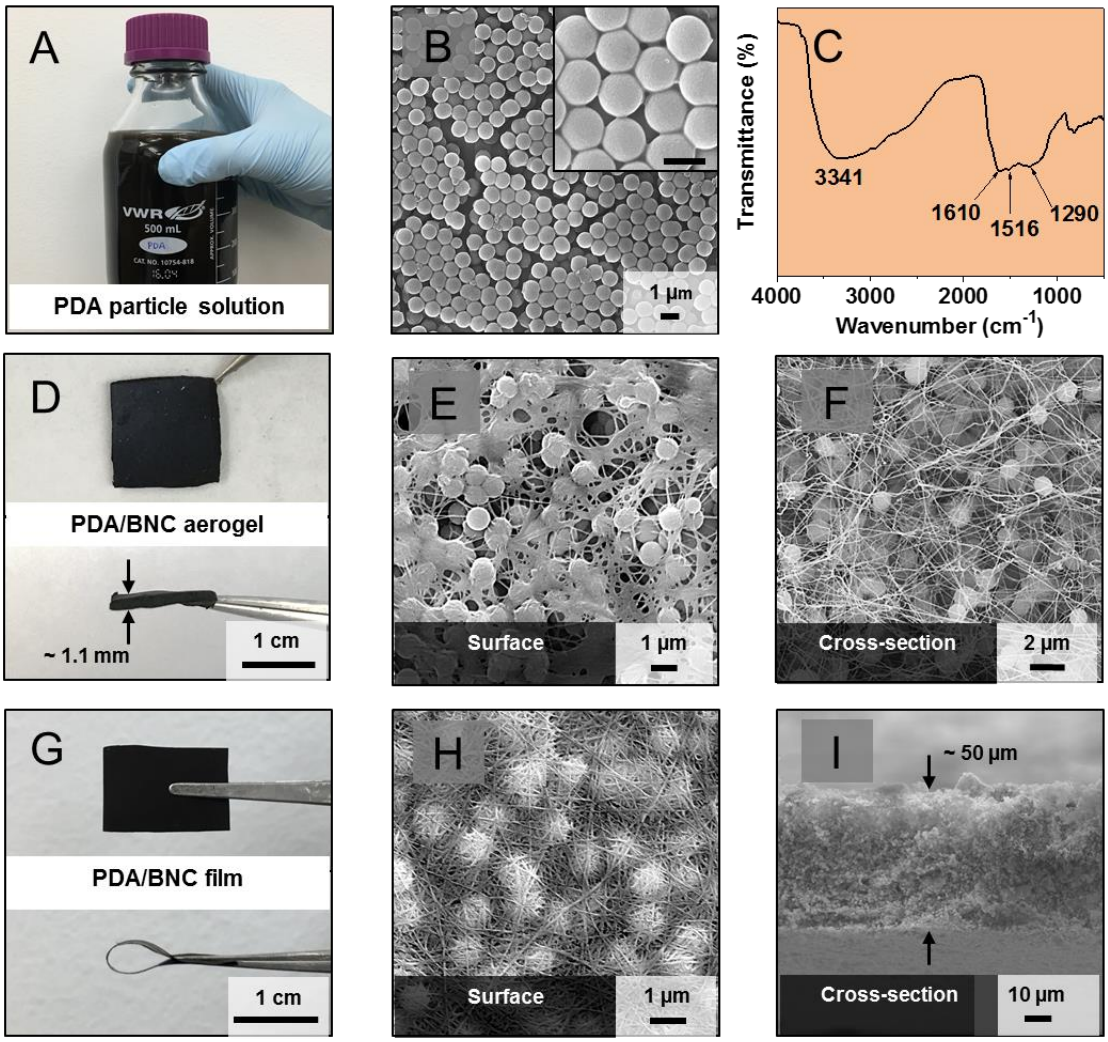

Figure 2. 2 (A) Photograph of the PDA particle solution. (B) SEM images of as-synthesized PDA particles (inset shows the higher magnification SEM image). (C) FTIR absorption spectrum of the PDA particles. Optical images (D), SEM images of the (E) surface and (F) cross-section of the freeze-dried PDA/BNC composite. Optical images (G), SEM images of the (H) surface and (I) cross-section of the air-dried PDA/BNC membrane.

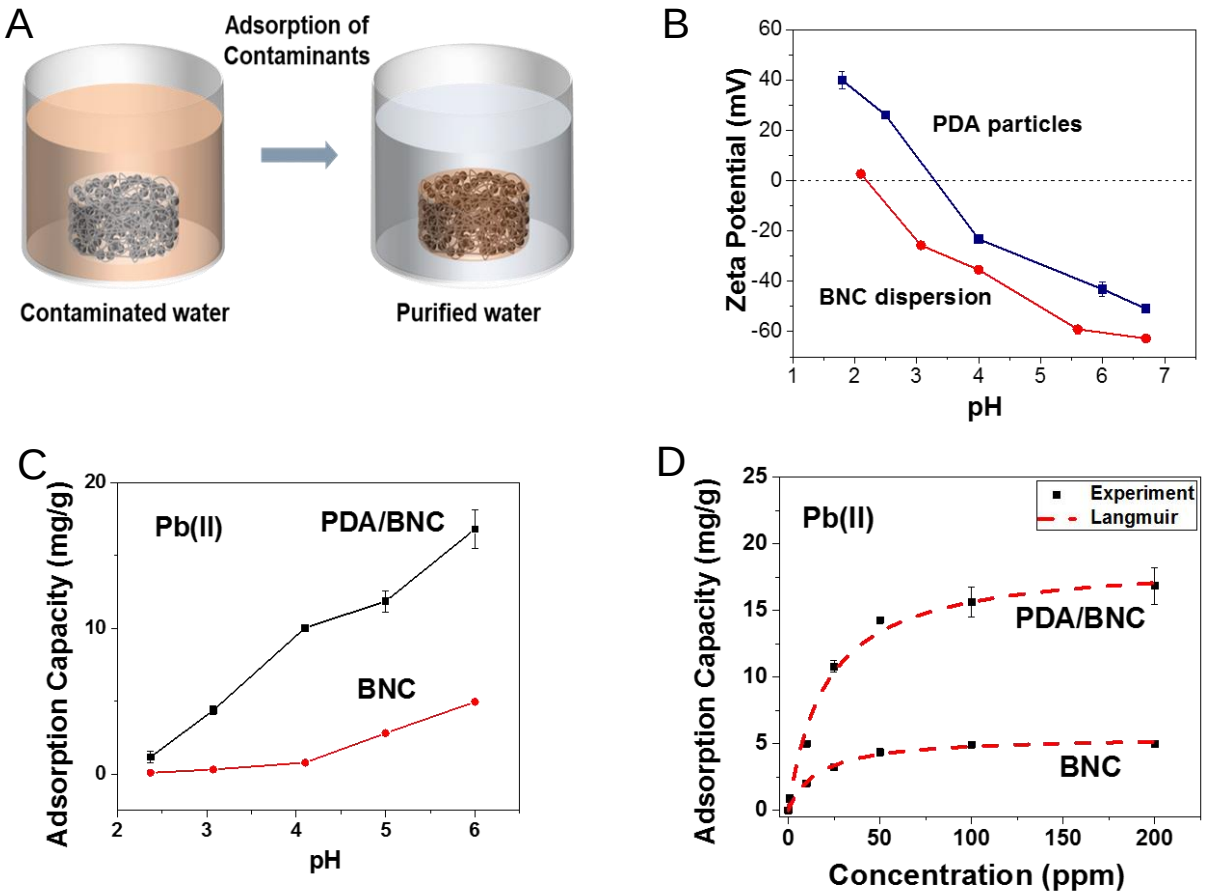

Figure 2. 3 (A) Schematic illustration of the batch adsorption test. (B) Zeta potentials of the PDA particles and BNC dispersion at different pH values. (C) Adsorption capacities of PDA/BNC and pristine BNC foams for Pb (II) at different pH values (experiments carried out at room temperature and the initial concentration of the contaminants was 200 ppm (D) Pb (II) adsorption isotherms of PDA/BNC and BNC foams and curve fitting by Langmuir (dash line) model (The initial pH value was adjusted to 6). (Number of replicates = 3, Error bars for BNC samples are small compared to the graph scale.)

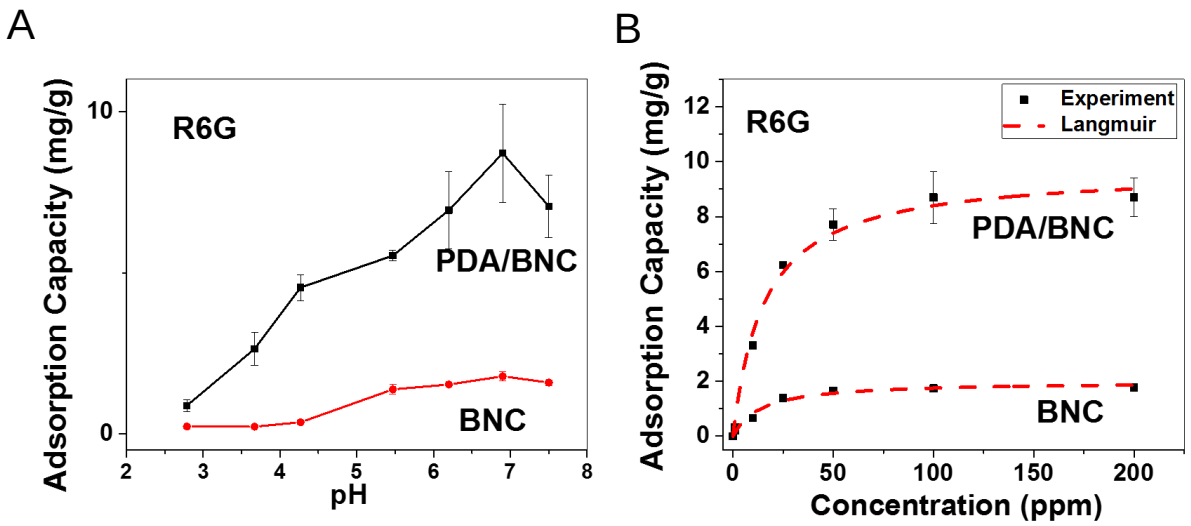

Figure 2. 4 (A) R6G adsorption capacities of PDA/BNC and pristine BNC foams at different pH values (experiments carried out at room temperature and the initial concentration of the contaminants was 200 ppm). (B) R6G adsorption isotherms of PDA/BNC and BNC foams and curve fitting by Langmuir (dash line) model (initial pH value was adjusted to 7). (Number of replicates = 3, Error bars for BNC samples are small compared to the graph scale.)

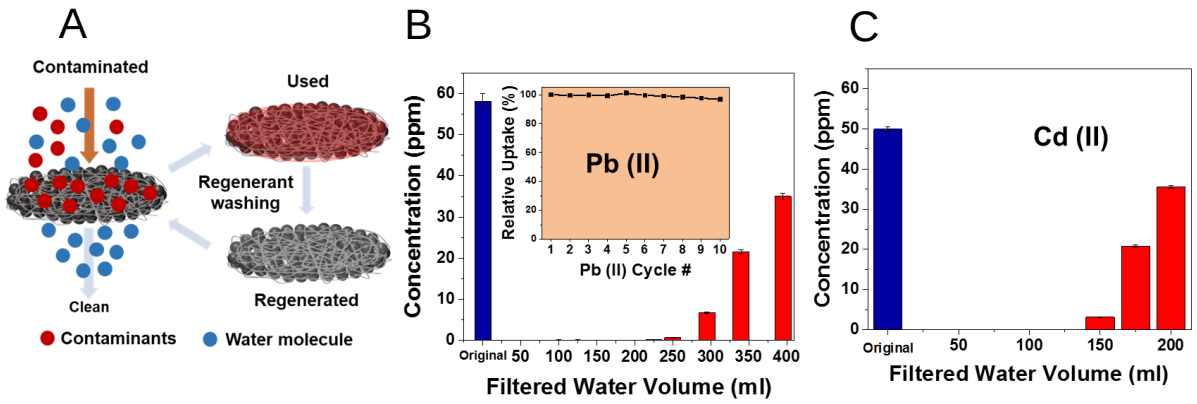

Figure 2. 5 (A) Schematic illustration of membrane filtration experiment. Permeate water concentrations after filtration of (B) Pb (II) with a feed concentration of 58 ppm (inset shows PDA/BNC membrane performance after 10 cycles of Pb (II) filtration-regeneration); (C) Cd (II) with a feed concentration of 50 ppm.

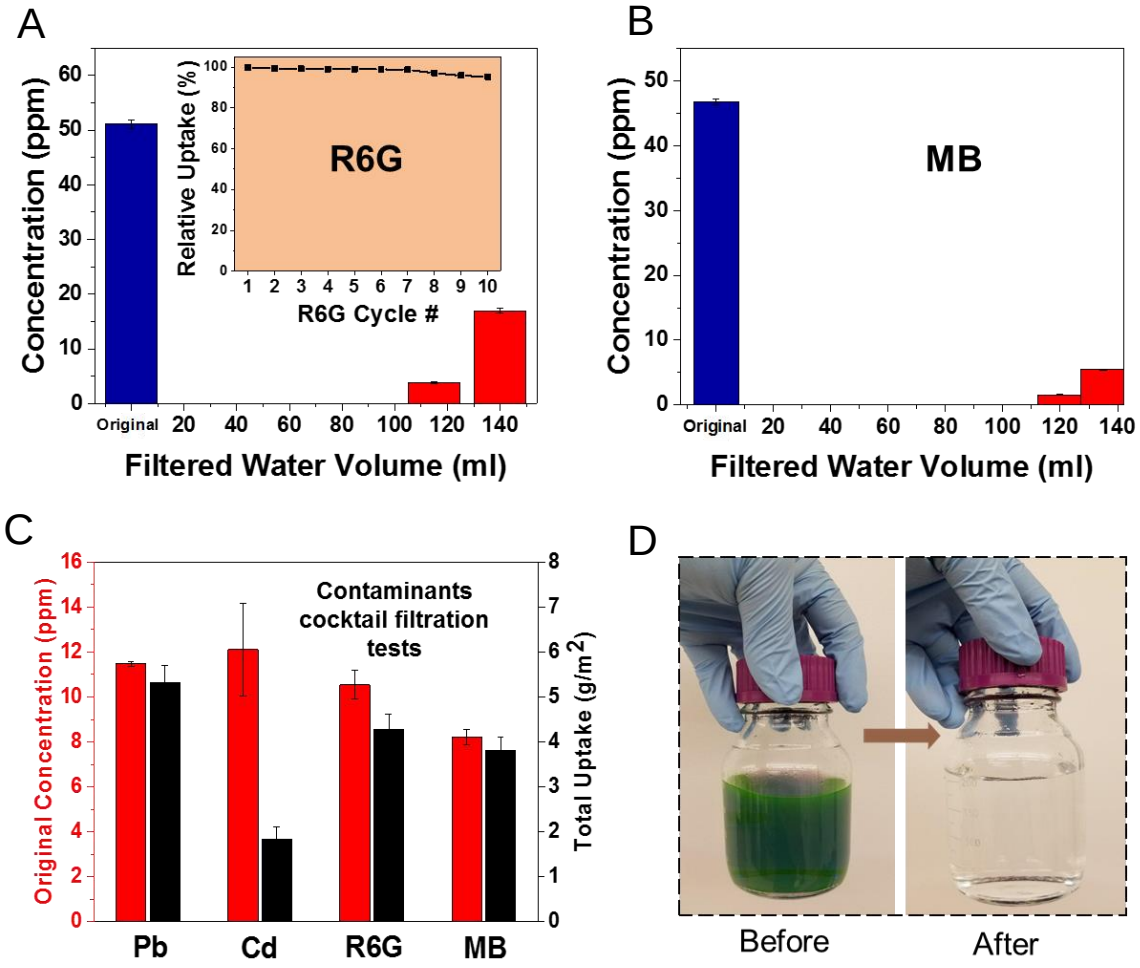

Figure 2. 6 Permeate water concentrations after filtration of (A) R6G with a feed concentration of 51 ppm (inset shows 10 cycles of filtration-regeneration of R6G) and (B) MB with a feed concentration of 47 ppm. (C) Single filtration tests of cocktail solution containing Pb (II) and Cd (II) ions as well as R6G and MB organic dyes (The bars on the left (red) show original concentration, and on the right (black) show total uptake). (D) Optical images of mixture solution before and after the cocktail filtration test.

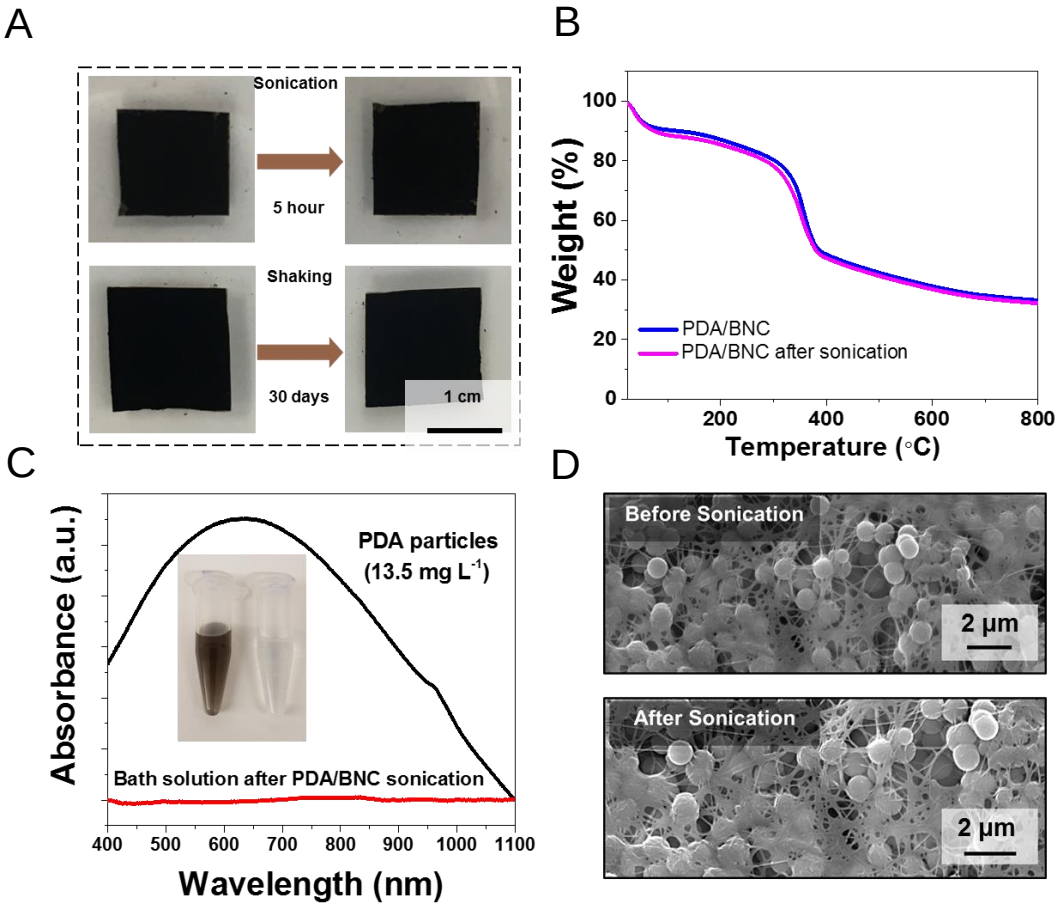

Figure 2. 7 (A) Optical images of the PDA/BNC composite before and after extensive sonication and mechanical agitation. (B) Weight loss profiles of PDA/BNC composite before and after sonication (5 hrs) obtained by TGA. (C) UV-vis spectra of the PDA particles (13.5 mg L^{-1}) and bath solution used for sonicating PDA/BNC membrane for 5 hrs (The inset is the optical image of the PDA particle solution (left) and bath solution used for sonication (right)). (D) SEM images of the PDA/BNC membrane before and after sonication (5 hrs).

Chapter 3: Palladium Nanoparticle-Decorated Mesoporous Polydopamine/Bacterial Nanocellulose as a Catalytically Active Universal Dye Removal Ultrafiltration Membrane

3.1 Introduction

Owing to the globally increasing demand for consumer goods, massive amounts of chemical wastes are produced and released into the environment by industries including textiles, paints, printing inks, cosmetics, plastics and paper.[30] These industrial effluents are highly contaminated by organic and inorganic compounds with textile wastewater being the most polluting among all industrial sectors.[31] Modern dyes, which are extensively used in many industries, offer superior color stability because of the high degree of aromaticity and extensive conjugation present in their chemical structures, which also make them harder to remove from water resources via traditional water treatment techniques.[32-33] Presence of these carcinogenic, mutagenic and persistent organic contaminants in natural environment, poses a great health risk for humans and aquatic ecosystems.[34-37] This greatly increases the need for the development of highly proficient and economical dye removal techniques from contaminated water.

To treat water resources contaminated with organic pollutants, several different technologies such as membrane filtration, catalytic degradation, photocatalytic oxidation and adsorption have been employed.[109-119] Among them, adsorption is one of the most commonly-used method for removing a variety of organic pollutants from water because of its simplicity and low cost.[120] However, adsorption alone cannot remove all the different dyes and not all adsorption-based

techniques are able to operate in a broad range of environmentally-relevant pH conditions.[121-122] Alternatively, catalytic degradation of organic dyes by noble and transition metal nanostructures has been shown to be highly efficient and practical in water remediation in a wide range of environmental conditions.[38-43] Among transition metals, palladium nanoparticles (PdNPs) have attracted special attention for dye degradation owing to its excellent catalytic properties and low environmental impacts.[123-125] Through catalytic degradation, the toxic organic pollutants with intrinsic poor biodegradability can be converted to degradable molecules through the electron transfer between catalysts and pollutants.[49] However, metal nanostructures when used as stand-alone (colloidal state) catalysts, tend to aggregate in solution and cause secondary contaminations, which makes the recovery of these nanostructures challenging.[126-128]

To alleviate the aggregation of metal nanoparticles and achieve prolonged catalytic activity, immobilizing them on various substrates has been proven to be a feasible approach. A wide range of substrates such as polydopamine (PDA)-based nanoparticle, carbon-based nanoparticles, silica, and metal oxides have been employed for this purpose.[24, 44-52] Among these, PDA, mussel-inspired synthetic polymer, has emerged as a promising material platform for the development of catalytically-active substrates.[1, 48-49, 52] PDA nanoparticles and PDA-based materials were used as substrates for immobilization of different metals such as silver, gold, palladium and platinum.[48-50, 53] However, the use of these stand-alone catalytically active composite particles is highly limited for practical applications in industrial waste water treatment, due to their colloidal stability, which requires extra steps to remove them from water.

Membrane technologies are being widely used by different industries due to their stability and ability to be used in continuous flow and high throughput dye removal setups.[27, 29, 129-130] In our

previous work, we demonstrated the use of solid PDA nanoparticle incorporated into nanocellulose matrix (PDA/BNC) as adsorption-based filtration membrane for removing organic dyes and heavy metals.[130] However, PDA/BNC membrane effectiveness in removing organic dyes was limited to cationic dyes and to pH values above 4-5. Incorporating catalytically active composite particles into membrane matrix can provide a highly efficient dye removal membrane for real-world applications. Several different types of membrane such as GO/BNC, PVDF, PET and cellulose acetate have been employed as efficient dye degradation membrane for methyl orange (MO), 4-nitrophenol (4NP), methylene blue (MB), Congo Red and 2,6-dinitrophenol.[44, 131-134] However, achieving an ultrafiltration membrane with high water flux and excellent organic dye removal characteristics is still a challenge.

Herein, we report a facile, scalable and highly efficient catalytically active ultrafiltration membrane based on bacterial nanocellulose (BNC) loaded with mesoporous PDA (mPDA) nanoparticles and palladium nanostructures. Mesoporous PDA nanoparticles are embedded into the BNC matrix during the growth process of BNC to generate mPDA-BNC membrane followed by *in situ* growth of Pd nanoparticles on mPDA nanoparticles and BNC fibers. Although Palladium is expensive, it is a popular catalyst for dye degradation due to its high efficiency and inert nature. Incorporation of bowl-like mPDA particles inside BNC matrix increases the pore size of the composite and provides high surface area for Pd nucleation and growth, which results in higher Pd loading compared to pristine BNC membrane. Moreover, due to the higher porosity of the membrane the water flux for the membrane is significantly higher compared to the existing commercial ultrafiltration membranes with the same range of pore size.[135] The Pd-mPDA-BNC membrane exhibited high degradation efficiency in removing anionic (MO), neutral

(4NP) and cationic (MB) dyes over a wide range of environmentally relevant pH conditions (3-9), making it an outstanding candidate for real-world applications in wastewater treatment.

3.2 Results and Discussion

3.2.1 Preparation of Pd-mPDA-BNC Membrane

Mesoporous polydopamine-bacterial nanocellulose (mPDA-BNC) membrane was fabricated by the addition of mPDA particles into *Gluconacetobacter hansenii* broth under aerobic and static conditions (Figure 3.1). Mesoporous bowl-like polydopamine nanoparticles were synthesized based on formation of block copolymer F127, PDA, and 1,3,5 trimethylbenzene (TMB) micelles at water/TMB emulsion interfaces followed by island nucleation and anisotropic growth on the surface of emulsion droplets.[136] Using this technique, porous polydopamine nanoparticles with the diameter of ~200 nm were formed with mesoscale channels (~11 nm diameter, ~21 nm center-to-center distance) aligned radially from the center to the surface (Figure 3.2A).

To synthesize palladium-decorated mPDA-BNC, we have employed two different approaches: (i) direct growth of Pd nanoparticles in the mPDA nanoparticles followed by their dispersion in bacteria growth solution to create membrane; and (ii) dispersion of mPDA particles into the bacteria growth solution to fabricate a composite membrane, followed by the formation of Pd nanostructures on nanocellulose fibers and mPDA nanoparticles. For the first approach, mPDA nanoparticles were dispersed in palladium chloride ($PdCl_2$) solution, which resulted in loading of the mPDA nanoparticles with Pd^{2+} ions formation of coordination compounds.[137-138] Subsequently, the mPDA nanoparticles were transferred to sodium borohydride ($NaBH_4$) solution to reduce the precursor (Pd (II) ions) to metallic palladium. The Pd nanoparticles were

primarily formed inside the pores of mPDA particles as shown in TEM image (Figure 3.2B). This is probably due to the trapping of Pd (II) ions inside the pores through electrostatic interactions between PDA and heavy metal ions, which prevents their during washing steps.[2] High-resolution transmission electron microscopy (HRTEM) of Pd decorated mPDA nanoparticles (Pd-mPDA) revealed lattice fringes with a lattice spacing of 0.23 nm, corresponding to (111) planes of Pd (Figure 3.2C). To create thin-film membrane, *Gluconacetobacter hansenii* bacterium was utilized to produce a non-woven network of cellulose nanofibers called bacterial nanocellulose. In the past, we have shown that various 2D nanomaterials such as graphene oxide and MoS_2 nanosheets and spherical nanoparticles such as SnO_2 and PDA nanoparticles can be trapped inside the nanocellulose network by adding these nanomaterials into the bacterial culture medium, resulting in a composite multi-functional structure.[130, 139-141] However, addition of the palladium-decorated mPDA particles to the growth solution inhibited the formation of cellulose network due to the antibacterial properties of the Pd nanostructures.[142] Hence, we employed the second approach for the fabrication of the membrane. Pd-mPDA particles were used to compare dye removal efficiency of pristine mPDA and Pd-mPDA nanoparticles. With no additives in bacterial culture medium, under typical growth conditions, a 1 mm thick cellulose hydrogel is formed after 2 weeks. Air-dried pristine BNC membrane is comprised of a dense network of cellulose nanofibers with a diameter of ~20-100 nm (Figure 3.2D). The cross-section SEM images of the pristine BNC membrane showed a uniformly layered structure with overall thickness of 7 μm (Figure S3.1A, supporting information). Addition of mPDA nanoparticles into the bacterial broth solution resulted in trapping of the mPDA nanoparticle within the nanocellulose fiber network. The resulting air-dried membrane exhibited highly porous structure compared to the pristine membrane as the

tight packing of the nanofibers is hindered by the presence of the PDA nanoparticles with hundreds of nanometers in size, which provide physical barriers for fiber-fiber interaction and collapse (Figure 3.2E). The air-drying process removes water from the expanded cellulose fiber network, thus causing the collapse of the 3D open porous network into compact film. The cellulose fibers form extensive inter-fiber hydrogen bonds, which results in small pore size of the membrane and significant loss in swellability upon rehydration.[143] The Pd NPs were *in situ* grown in the mPDA-BNC composite by exposing the mPDA-BNC membrane to Pd (II) precursor (palladium chloride) solution and subsequent reduction using a strong reducing agent, $NaBH_4$. Scanning electron microscopy images revealed that palladium nanostructures were formed on mPDA particles and BNC fibers throughout the membrane (Figure 3.2F).

The Pd growth on the mPDA-BNC membrane is notably different from that on mPDA particles. The size of Pd nanostructures and areal coverage of the Pd nanostructures was significantly higher compared to that observed in free mPDA nanoparticles in solution. This difference in the structure and coverage of Pd nanostructures possibly stems from the more efficient trapping of the Pd precursor within the composite membrane compared to the nanopores of the free mPDA nanostructures. The cross-section SEM images of the Pd-decorated mPDA-BNC (Pd-mPDA-BNC) showed uniform Pd formation with increased membrane thickness of 17 μm (Figure S3.1B, supporting information). This increase in the membrane thickness comes from combination effect of mPDA particle trapping in BNC matrix and growth of Pd nanostructures in situ. For comparison, the same procedure was used to create Pd nanostructures on the pristine BNC membrane (Pd-BNC). The SEM images of the surface of the Pd-BNC membrane showed sparse Pd structures formed on the surface with a large fraction of the surface free of Pd

nanostructures, which may be attributed to the highly dense network structure of pristine BNC membrane compared to mPDA-BNC membrane (Figure S3.2A, supporting information). Atomic force microscopy image of the Pd-BNC further confirmed the low coverage of the Pd nanostructures on the BNC surface (Figure S3.2B, supporting information). The thermogravimetric analysis of the membranes showed that Pd accounts for 20.3 wt% in Pd-mPDA-BNC and 13.6 wt% in Pd-BNC (Figure S3.3, supporting information). The higher Pd loading in Pd-mPDA-BNC compared to pristine BNC membrane shows that the incorporation of mPDA nanoparticles provides higher density of active sites for the *in situ* growth of Pd nanostructures, thereby potentially improving its catalytic properties.

To understand the chemical composition of Pd-mPDA-BNC membrane, we performed X-ray photoelectron spectroscopy (XPS) measurements. The binding energy of Pd $3d_{5/2}$ and Pd $3d_{3/2}$ obtained from the Pd-mPDA-BNC at 333.0 and 338.3 eV can be assigned to Pd (0), indicating the metallic form of Pd. The peaks at 334.1 and 339.1 eV correspond to the oxidized form of Pd (Pd^{2+}) (Figures 3.2G, Figure S3.4, supporting information).[144-145] The Pd(0):Pd(II) ratio is calculated to be around 19.5:10, indicating that a major fraction of Pd in the Pd-mPDA-BNC membrane exists in the metallic form.[146] Energy-dispersive X-ray spectroscopy (EDS) analysis further confirmed the presence of Pd in the membrane with strong peaks at 2.85 eV and 3.01 KeV (Figure 3.2H). Furthermore, the presence of Pd nanoparticles in the membrane was also verified by X-ray diffraction (XRD). The XRD pattern exhibited four peaks at 40.2°, 46.7°, 68.3° and 82.1° corresponding to the (111), (200), (220) and (311) planes of typical face centered cubic Pd, respectively (Figure 3.2I).[147]

3.2.2 Batch Reaction for Wastewater Treatment

The mPDA nanoparticles are used instead of PDA because they provide nanopores for Pd nucleation (Figure 3.2) and higher surface area for efficient adsorption of organic dyes. Figure S5 demonstrates the superior performance of mPDA particles compared to PDA particles with improved dye removal efficiency for all three dyes at all pH values tested. As a proof-of-concept for degradation efficiency, we evaluated the dye removal efficiency of the Pd-mPDA particles. Methyl orange (MO, anionic dye), 4-nitrophenol (4NP, neutral) and methylene blue (MB, cationic dye) were selected as model dyes. The dye removal efficiency of the Pd-mPDA and mPDA particles were compared under a wide range of environmentally relevant pH conditions. Polydopamine is not stable at extremely acidic or alkaline solutions, hence, pH values from 3 to 9 were chosen for the dye removal experiments.[148] Polydopamine adsorbs positively charged organic dyes mainly through electrostatic interactions above pH 4.[130] However, the adsorption efficiency is low for negatively charged and neutral dyes above pH 4, which is attributed to the negatively charged surface of PDA under these conditions (isoelectric point of PDA is 3.2).[130] We hypothesized that this low efficiency can be overcome by incorporating catalytically-active Pd nanoparticles in mPDA nanoparticles. The dye removal mechanism of mPDA is exclusively through adsorption, while that of Pd-mPDA nanoparticles is through the synergistic effect of adsorption and catalytic degradation. The chemical degradation of dye in presence of catalyst involves the adsorption of borohydride ions (BH_4^{-1}) on the surface of the catalyst, releasing hydrogen on its surface. This in turn forms catalyst-H complexes on the surface of the catalyst as follows[149-151]:

$$NaBH_4 + H_2O \rightarrow NaBO_2 + H_2 \quad (3.1)$$

$$C + H_2 \rightarrow H - C - H \quad (3.2)$$

Where, C represents the catalyst. The dye molecules then adsorb on the surface of catalyst via hydrogen bonding. After the adsorption of dye, the catalyst surface transfers the electron from reducing agent ($NaBH_4$ in this case) to the dye molecules, thereby facilitating the degradation of dye.[152-153] The degradation product is then desorbed from the surface of the catalyst and diffuses to the bulk region, thereby evacuating the catalytically active site for next reduction run.[154] Sodium borohydride reacts with water to form sodium borate, both of which are toxic and should not exist in water in large amounts.[151] Although most studies reporting catalytic degradation of organic dyes use sodium borohydride as reducing agent, its concentration should be carefully considered to minimize the possible adverse effect on the environment and human health (more information on environmental impact of sodium borate is provided in Supporting Information).[155]

The catalytic degradation of methyl orange results in the formation of sulfanilic acid and aromatic amines,[156-159] degradation of methylene blue results in leucomethylene blue[149-150, 152-153] and that of 4-nitrophenol results in 4-aminophenol.[160-162] The byproducts of the catalytic degradation are colorless and have various industrial and medicinal applications, although toxic in higher amounts.[149-150, 152-154, 156-158, 160-162] This suggests that the processed water can be utilized by industries for the manufacture of commercially relevant products.[162] The reaction kinetics were monitored using UV-vis spectroscopy. The MO, 4NP and MB exhibit absorption peaks at 465 nm, 400 nm, and 664 nm, respectively (Figure 3.3A, B and C). The MO removal efficiency for mPDA nanoparticles decreased with increasing pH, which results in an increase in the negative surface charge of mPDA nanoparticles, thus weakening the electrostatic adsorption of negatively charged dye (Figure 3.3D). However, the Pd-mPDA nanoparticles in the presence of

NaBH4 exhibited removal efficiency above 99% at all pH conditions, which can be attributed to the synergistic effect of electrostatic adsorption and catalytic dye degradation. In the case of neutral dye 4NP, removal efficiency for mPDA nanoparticles was below 10% at all pH values, however, the Pd-mPDA nanoparticles exhibited more than 99% removal efficiency at all pH conditions (Figure 3.3E). The removal efficiency of positively charged MB increased with pH in case of mPDA nanoparticles due to favorable electrostatic interactions between mPDA nanoparticles and MB at higher pH values (Figure 3.3F). In other words, the MB removal efficiency of pristine mPDA nanoparticles was lower under low pH conditions. On the other hand, the Pd-mPDA nanoparticles exhibited removal efficiency above 99% at all pH values tested. These results systematically demonstrate that incorporation of catalytically active species, such as Pd nanoparticles, with mPDA nanoparticles renders synergistic effect of dye adsorption and degradation, thus significantly improving the overall dye removal efficiency. It is known that sodium borohydride decomposes at different rates in water at different pH. At pH around 10, sodium borohydride is more stable in water. At pH around 7, decomposition rate is much faster (two orders of magnitude) compared to the rate of reaction at pH 10.[163] But, this should not affect the degradation process in our experiments, since all the elements needed for degradation are already available when sodium borohydride is introduced to the solution. This way, sodium borohydride decomposition will help degradation of the dye in presence of catalyst (Pd) at all pH values as is evident from high removal rate (above 99%) for all dyes at all pH values (Figure 3.3).

Having established the synergistic effect of mPDA and Pd nanoparticles, we set out to explore the reaction kinetics of catalytic dye degradation of Pd-mPDA-BNC membrane. For this, a 1x1

cm^2 piece of Pd-mPDA-BNC membrane was immersed into MO, 4NP and MB dye solutions containing $NaBH_4$ (see Experimental section for details). Subsequently, the change in absorbance of each dye was monitored to track the kinetics of the reaction. For MO, the absorption peak at 465 nm decreased rapidly in the first minute and then the rate of change in absorbance decreased (Figure 3.4A). The absorbance continued to decrease slowly due to dye degradation until the solution became completely colorless (not shown in the plot). The MO solution containing $NaBH_4$ without the Pd-mPDA-BNC membrane did not show any sign of color change, indicating the need for the catalyst in the degradation reaction (Figure S3.6, supporting information). For comparison, we have also introduced BNC and mPDA-BNC membranes (1x1 cm^2) and immersed into the MO solution containing $NaBH_4$. However, we noted only small decrease in the absorbance (11%) after 30 minutes, suggesting that without the presence of Pd as catalyst, the degradation reaction proceeds at an extremely slow rate. The batch degradation experiment for 4NP showed similar behavior with Pd-mPDA-BNC membrane degrading the 4NP rapidly during first two minutes followed by slower rate until complete degradation (Figure 3.4B). The BNC and mPDA-BNC membranes did not result in any noticeable change in the 4NP absorbance confirming the catalytic degradation of 4NP in the presence of Pd nanostructures. The degradation kinetics of MB were significantly different compared to the former two dyes in that it exhibited significantly smaller slope but linear degradation over a longer time scale (Figure 3.4C). The significantly different degradation kinetics of MB compared to MO and 4NP possibly stems from the electrostatic attraction between positively charged MB and negatively charged BNC and mPDA .[130] In addition to electrostatic adsorption of MB on negatively charged surface, the constant flux of dye molecules towards the membrane facilitates catalytic degradation. As a result, absorbance of corresponding

to MB completely disappeared within 5 min, which is in stark contrast to the other two dyes tested.

To demonstrate the advantage of using mPDA-BNC composite membrane as the template to grow Pd nanostructure, we investigated the catalytic activity of pristine BNC membrane containing *in situ* grown Pd nanostructures. For all three dyes, the degradation trend was similar to the Pd-mPDA-BNC, however, with a slower reaction rate. Use of mPDA-BNC as a template improved the degradation speed owing to the larger surface area mPDA nanostructures, which facilitated higher Pd nanostructures loading (20% by weight) compared to pristine BNC (13% by weight). The Langmuir–Hinshelwood apparent first-order kinetics was used to estimate and compare the reaction rate constant for different dyes and substrates (Figure 3.4D, E and F). From pseudo first-order kinetics analysis, the rate constant of Pd-mPDA-BNC membrane was higher than Pd-BNC membrane for all three dyes. By using the mPDA-BNC as the template to grow the Pd nanostructures, the rate of the reaction increased by ~100% for all three dyes, suggesting the effectiveness of the Pd-mPDA-BNC in improving the catalytic degradation efficacy.

3.2.3 Membrane Filtration

Now, we turn our attention to the possible application of the Pd-mPDA-BNC membrane as a filtration membrane for treatment of organic dye-polluted water. To test this, the membranes were placed in a benchtop filtration setup under 0.8 bar vacuum pressure. For each dye, varying concentrations of dye contaminated water (from low to high) were filtered through the membranes. Subsequently, the change in absorbance of the dye-contaminated water upon filtration was used to calculate the dye removal efficiency. For MO, the filtered water was completely colorless until 50 ppm with removal efficiency above 99%. Although above 50 ppm

(extremely toxic concentrations) the filtration efficiency gradually decreased, the membrane was still able to remove more than 92% of the MO at 200 ppm (Figure 3.5A). For comparison, 50 ppm MO solution containing $NaBH_4$ was filtered through the pristine BNC membrane with removal efficiency of only 20% (Figure S3.7A, supporting information). In the absence of $NaBH_4$, Pd-mPDA-BNC membrane used to filter 50 ppm MO solution, resulted in only 17% removal efficiency, highlighting the need for presence of both $NaBH_4$ and Pd nanostructures for high removal efficiency (Figure S3.7B, supporting information). It is worth noting that the dye removal efficiency decreases with an increase in the water flux.[135, 164] Although the effect of water flux is not systematically studied here, we noted that by increasing the porosity of the membrane (freeze-drying instead of air-drying), water flux increased, and the degradation efficiency decreased, possibly due to the shortened time of interaction between catalyst and dye.

In the case of 4NP, the Pd-mPDA-BNC membrane removed more than 99% of the contaminant until 100 ppm. The removal efficiency gradually decreased for higher concentrations but remained above 94% up to 200 ppm (Figure 3.5B). For MO and 4NP, the dye removal is caused mainly by catalytic degradation with little or virtually no contribution from dye adsorption. However, in the case of MB, adsorption on Pd-mPDA-BNC also contributes to the overall removal efficiency. The Pd-mPDA-BNC exhibited significantly higher removal efficiency for MB with 99% dye removal efficiency until 300 ppm (Figure 3.5C). It was only at 400 ppm MB concentration that the removal efficiency dropped to 95%. These results indicate the excellent dye removal efficiency of Pd-mPDA-BNC, stemming from the synergistic effect of catalytic degradation and adsorption of three different classes of organic dye molecules. We observed that when Pd-mPDA-BNC membrane is subjected to solution containing dye but without sodium

borohydride, membrane surface turned to blue color, indicating the formation of organic film on the membrane. However, in the presence of sodium borohydride, due to the catalytic degradation of the MB, no significant change in the color of the membrane was observed.

Next, we investigated the recyclability of Pd-mPDA-BNC membranes by washing them with water and alcohol mixture and reusing them for filtration of 50 ppm MO solution.[165-166] The membranes retained their removal efficiency above 96% even after 5 cycles of washing/filtration steps (Figure 3.5D). Furthermore, in order to explore if the removal happens preferentially for certain dyes, a 50 ml cocktail containing MO, 4NP and MB (10 ppm of each dye) in presence of $NaBH_4$ was filtered through a regenerated Pd-mPDA-BNC membrane (Figure 3.5E). All the dyes were effectively removed from the solution and solution turned colorless from its original green color (Figure 3.5F).

For real world applications involving regular filtrations and mechanical agitations, the structural integrity of the membrane is critical. To assess their mechanical stability, Pd-mPDA-BNC membranes were subjected to 30-day mechanical agitation and 1-day harsh ultrasonication. The membrane structure compared to that of the pristine Pd-mPDA-BNC membrane and supernatant color were examined (Figure 3.6A). After 30-day mechanical shaking, there is no sign of particle leakage and damage to the membrane (Figure 3.6B). However, after 1-day of harsh ultrasonication, a small amount of the Pd nanostructures leaked from membrane into the solution as evidenced by the color of the solution (Figure 3.6C).

Ultrasonication is an extreme case, which rarely happens in real-world applications. TGA curves after mechanical shaking showed no signs of weight change in the membrane confirming the

negligible leakage of Pd (Figure 3.6D). However, after 1-day sonication, there was ~3% weight loss in the membrane, indicating Pd loss during the process. Furthermore, to assess the amount of Pd loss during the mechanical shaking, the Pd concentration in the supernatant of Pd-BNC and Pd-mPDA-BNC membranes was measured by inductively coupled plasma mass spectrometry *(ICP-MS)* (Figure 3.6E). The presence of trace amount Pd in the supernatant (122 ppb for Pd-mPDA-BNC and 305 ppb for Pd-BNC) suggest that although there was no measurable weight loss in TGA curves, small fraction of Pd particles leached out during the shaking. These results also indicate that Pd-mPDA-BNC is more stable compared to Pd-BNC, yet another advantage of the composite membrane compared to pristine BNC. The BNC membrane consists of a tightly packed matrix of cellulose nanofibers and Pd nanoparticles only form on the surface of the BNC (Figures 3.2D and S3.2). Hence, the Pd nanostructures that are formed on the surface are not mechanically interlocked and are prone to desorption during mechanical agitation. On the other hand, the mPDA-BNC membrane structure is more porous with Pd nanostructures covering the entire surface of cellulose nanofibers and mPDA particles (Figure 3.2F). The Pd nanostructures interact with both PDA particles and the BNC fibers, which serve as anchoring sites to resist desorption during mechanical agitation.

Considering the importance of metallic Pd in the dye degradation, XRD spectra was collected before and after the dye degradation filtration experiments (Figure 3.6F). The virtually identical XRD spectra before and after filtration further confirmed the stability of the Pd nanostructures in the membrane. The pore size of the Pd-mPDA-BNC membrane was assessed by filtering 5 nm gold nanoparticles solution (Figure S3.8, supporting information).[44, 130] The filtered solution is free of gold nanoparticles with rejection rate of ~100% as determined using UV-vis extinction spectra, indicating that membrane pore size to be smaller than 5 nm. Furthermore, it is expected

from the combined observations of SEM images (Figure 3.2 and Figure S3.2) and particle rejection test that the pore size distribution is in the range of few nanometers to few tens of nanometers. Hence, the Pd-mPDA-BNC membrane falls in the category of ultrafiltration membrane. Finally, the water flux through the Pd-mPDA-BNC membrane was measured to be 137.4 L m-2 h-1 under 0.8 bar vacuum pressure. This is much higher than ~ 15 L m^{-2} h^{-1} at 4 bar which we observed from the commercially available color reduction ultrafiltration membrane (YMGESP3001, Sterlitech) which we tested in our previous study (with 95.2% removal efficiency for 10 mM MO).[44]

3.3 Conclusion

In conclusion, we demonstrated a highly efficient organic dye removal membrane based on BNC loaded with mPDA and Pd nanoparticles for wastewater treatment. Key factors which enable the Pd-mPDA-BNC membrane to be effective in dye removal are as follow: synergistic effect of dye adsorption on mPDA and catalytic ability of Pd nanoparticles in presence of NaBH4; highly porous structure due to the addition of mPDA nanoparticles, which increases the specific surface area for higher adsorption and degradation; and uniform and high loading of Pd nanoparticles within the entire membrane. The membrane fabrication process is simple and is easily scalable. The Pd-mPDA-BNC membrane exhibited excellent dye removal performance (above 99% removal for MB even at extremely high concentration of 300 ppm) as well as the ability for the treatment of multiple contaminants with different chemical structures and charge simultaneously. The membrane exhibited significantly higher water flux (137.4 L m^{-2} h^{-1}) compared to commercially available membranes even under low vacuum pressure of under 0.8 bar. The facile and the scalable fabrication of the membrane along with excellent dye removal efficiency and

higher water flux makes it a highly attractive candidate for wastewater treatment even at industrial scales.

3.4 Experimental Section

Materials: 1,3,5-trimethylbenzene (TMB), block copolymer F-127 (Pluronic F-127), dopamine hydrochloride, 30% ammonium hydroxide solution, glucose, sodium borohydride ($NaBH_4$), palladium chloride ($PdCl_2$), methyl orange, 4-nitrophenol and methylene blue were purchased from Sigma-Aldrich. Yeast extract, peptone and disodium phosphate were purchased from Fisher Scientific and citric acid was purchased from Alfa Aesar. *Gluconacetobacter hansenii* was obtained from ATCC (ATCC® 53582). 190 proof ethanol was obtained from Decon Labs, Inc. All the chemicals were used with no further purification. Nanopure water (≥18.2 MΩ) was used for the preparation of all solutions unless otherwise stated.

Synthesis of mesoporous polydopamine particles: Mesoporous polydopamine (mPDA) particles with radially oriented mesoporous channels were synthesized via emulsion-induced anisotropic assembly technique.[136] In a typical synthesis, 1.5 g of dopamine hydrochloride, 1 g of the block copolymer F-127 and 2 ml of TMB were dispersed in 100 ml of 1:1 ethanol-water mixture via ultrasonication to form an emulsion. To this emulsion solution, 3.75 ml of 30% ammonium hydroxide solution was added dropwise under moderate stirring. The mPDA particles were collected via centrifugation after 2 hours and washed three times with water and ethanol. Then the particles were redispersed in 20 ml of 1:1 ethanol-water mixture and heated at 100 ^{o}C for 24 hours in a sealed Teflon-lined autoclave to stabilize the mesostructure. The resulting mPDA particles were washed three times with ethanol and water and then redispersed in water for further use.

Synthesis of Pd decorated mDA particles: The mPDA particles were dispersed in $PdCl_2$ solution (2.5 wt% in 5 wt% of HCl) and incubated for 2 hours, followed by washing in water to remove excess $PdCl_2$. Subsequently, Pd^{2+} ions were reduced to metallic Pd in $NaBH_4$ solution (100mM) for 10 min to achieve *in situ* formation of Pd nanoparticles on mPDA. The resultant Pd decorated mPDA nanoparticles were washed three times in water and redispersed in water for further use.

Fabrication of mPDA-BNC membrane: The fabrication technique introduced in our previous work was employed with slight modifications to synthesize mPDA-BNC membrane.[130] *Gluconacetobacter hansenii* (ATCC®53582) was cultured in test tubes containing 16 ml of #1765 medium at 30 °C under shaking at 250 rpm. The #1765 medium was composed of 2% (w/v) glucose, 0.5% (w/v) yeast extract, 0.5% (w/v) peptone, 0.27% (w/v) disodium phosphate, and 0.5% (w/v) citric acid. The as synthesized mPDA particles (14 ml of 0.1 wt%) was centrifuged and redispersed in #1765 medium and centrifuged again to obtain a wet mixture of mPDA and medium after decanting the supernatant. Subsequently, this wet mixture was dispersed in a mixture of *Gluconacetobacter hansenii* culture solution and fresh medium (2 ml and 12 ml, respectively). This mixture was then transferred to a petridish (6 cm diameter) and left undisturbed at room temperature for 2 weeks. The membrane fabrication process can be modified to significantly reduce the fabrication time to around three days.[44] After 2 weeks, the mPDA-BNC hydrogel was first washed in boiling water for 6 hours and then dialyzed in nanopure water for 1 day. Then the cleaned mPDA-BNC hydrogel was air dried in an oven at 60 ^{o}C for 12 hours to obtain mPDA-BNC membrane. Pristine BNC membrane was also obtained using an identical procedure except for the addition of mPDA particles.

Formation of Pd Nanostructure on mPDA-BNC membrane: The mPDA-BNC membrane was immersed in $PdCl_2$ solution (2.5 wt% in 5 wt% of HCl) and incubated for 1 hour. This $PdCl_2$ soaked membrane was then immediately immersed in 100 mM $NaBH_4$ solution for 10 min to achieve *in situ* formation of Pd nanoparticles on membrane fibers and mPDA surface. The obtained Pd-mPDA-BNC membrane was then air dried in an oven at 60 ^oC for 2 hours.

Materials Characterization: Scanning electron microscopy (SEM) images were obtained by using a JEOL JSM-7001 LVF Field Emission scanning electron microscope at an accelerated voltage of 10kV. Transmission electron microscopy (TEM) images were obtained using JEM-2100F (JEOL) field emission STEM at an operating voltage of 200 kV. X-ray photoelectron spectroscopy (XPS) analysis was performed using Physical Electronics® 5000 VersaProbe II Scanning ESCA (XPS) Microprobe. The X-ray diffraction (XRD) patterns of the membranes were obtained using a Bruker D8-Advance X-ray powder diffractometer using Cu Kα radiation (λ = 1.5406 Å). TGA was performed in nitrogen atmosphere using a TA Instruments Q5000 IR Thermogravimetric Analyzer at a heating rate of 10 ^oC/min. The optical absorption spectra of dye-contaminated water were obtained using a Shimadzu UV-1800 UV-Vis spectrometer. Trace amounts of Pd was measured using ICP-MS: PerkinElmer NexION 2000 in duplicates of three different dilutions and the average of all 6 measurements was reported.

Evaluation of dye removal performance of Pd-mPDA particles: The dye removal performance of Pd-mPDA particles was evaluated by incubating Pd-mPDA particles (200 µg/ml, final concentration) with dye-contaminated water (10 ppm, final concentration) in the presence of $NaBH_4$ (1.2 mM, final concentration) at different pH (3,5,7,9) under constant stirring. In these experiments, pH of the dye solution was adjusted to desired value using NaOH or HCl, then it was mixed with Pd-mPDA nanoparticles, followed by addition of the $NaBH_4$. After 10 minutes,

the mPDA particles were centrifuged down and the optical spectra of the dye solutions before and after the particle incubation was monitored. The dye removal efficiency of the particles was calculated using the following equation:

$$Dye\ removal\ efficiency\ (\%) = \frac{c_o - c_f}{c_o} \times 100 = \frac{A_o - A_f}{A_o} \times 100 \quad (3.3)$$

Where, c_o and c_f are the initial and final dye concentration, A_o and A_f are the initial and final dye optical absorbance, respectively.

Evaluation of catalytic kinetics of Pd-mPDA-BNC membrane: The catalytic kinetics of the Pd-mPDA-BNC membrane was evaluated by monitoring the evolution of catalytic dye-degradation reaction with time. $NaBH_4$ (1.5 mM, final concentration) was rapidly added into the dye solution (15 ppm, final concentration) under constant stirring and subsequently, Pd-mPDA-BNC membrane (1 cm X 1 cm) was placed in 1.5 ml of the above solution to initiate the catalytic reaction. The concentration of the reactant (dye) obtained from UV-Vis spectra of the solution was monitored every 30 sec for 11 minutes. The rate constant of the degradation reaction of dye using Pd-mPDA-BNC as a catalyst was estimated via Pseudo-first-order kinetics as follows:[167]

$$\ln\left(\frac{c_o}{c_t}\right) = kt \quad (3.4)$$

Where, c_o is the initial reactant concentration, c_t is the reactant concentration at time t, k is the reaction rate constant and t is the reaction time. In this reaction, the ratio of c_t and c_o was calculated from the relative absorbance intensity of A_t/A_o.

Evaluation of dye removal performance of Pd-mPDA-BNC ultrafiltration membrane: The dye removal performance of the Pd-mPDA-BNC ultrafiltration membrane was evaluated via filtering dye-contaminated water through the membrane using a benchtop vacuum filtration setup. The diameter of all the membranes used in vacuum filtration is 3 cm. 10 ml of varying concentrations of dye solutions (0 – 200 ppm) were filtered through the membrane placed in a benchtop vacuum filtration setup under 0.8 bar in the presence of $NaBH_4$ (2.5 mM, final concentration). The optical absorption spectra of the solutions before and after filtration was monitored and the dye removal efficiency of the membrane was calculated as follows:

$$Dye\ removal\ efficiency\ (\%) = \frac{A_o - A_f}{A_o} \times 100 \quad (3.5)$$

Where, A_o is the initial dye optical absorbance and A_f is the final dye optical absorbance after filtration.

Flux and particle rejection test: Water flux of the Pd-mPDA-BNC membrane was estimated using a benchtop vacuum filtration setup under 0.8 bar by filtering 200 ml of water through a fixed cross-section area of membrane and the total time for filtration was recorded. The water flux was calculated as follows:

$$Water\ flux = \frac{Volume\ of\ water\ filtered}{Area \times Time} \quad (3.6)$$

Gold nanoparticles (AuNPs) with a diameter around 5 nm were synthesized using previously reported successive seed-mediated growth synthesis.[168] 10 ml of the as-synthesized AuNP

solution was then filtered through Pd-mPDA-BNC membrane using the above mentioned benchtop vacuum filtration setup under 0.8 bar. The optical extinction spectra of feed and permeate solutions were monitored and the rejection rate was determined as follows:

$$Rejection\ rate = \frac{E_f - E_p}{E_f} \times 100 \quad (3.7)$$

Where, E_f and E_p are the optical extinction of feed and permeate solutions, respectively.

3.5 Supporting Information

Supporting Information for chapter 3 is provided in appendix 2.

3.6 Figures

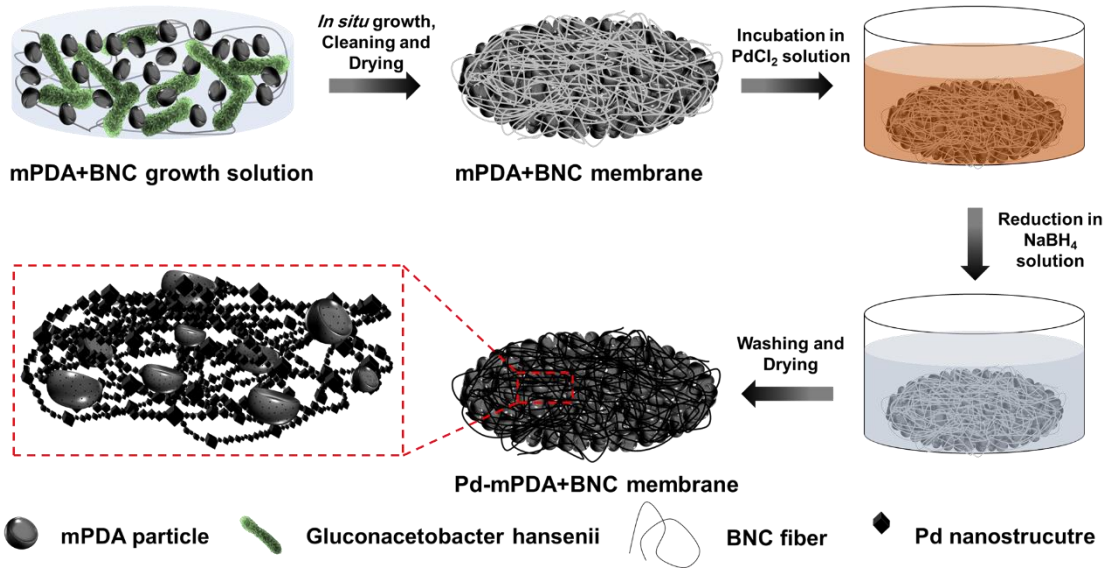

Figure 3. 1 Schematic illustration showing the preparation of the catalllically active Pd-mPDA-BNC membrane. Bacteria produces cellulose nanofibers in the presence of the mPDA particles to create mPDA-BNC hydrogel. The mPDA-BNC hydrogel is incubated in $PdCl_2$ solution, subsequently transfereed to $NaBH_4$ solution to create metalic palladium nanostructures on the cellulose fibers and mesoporous polydopamine nanoparticles.

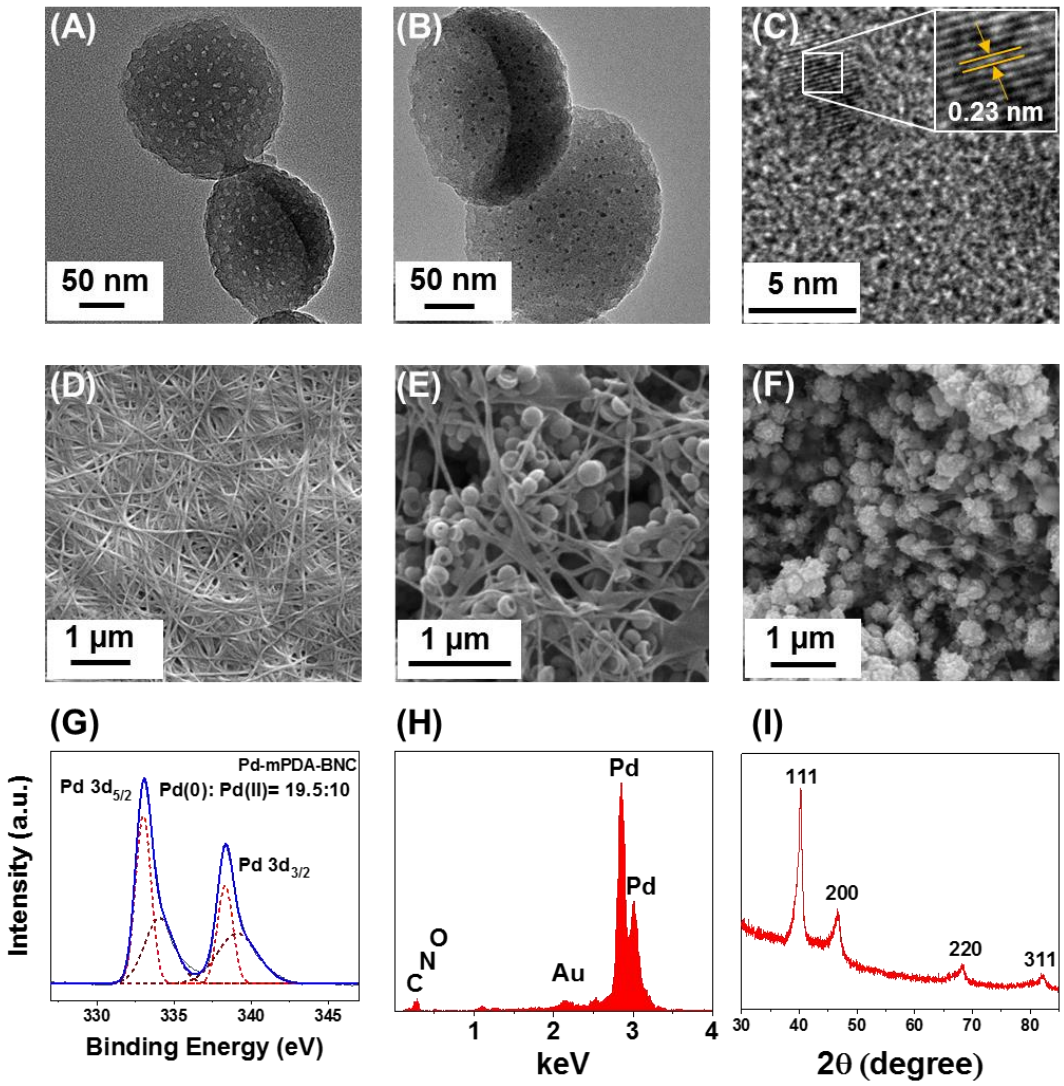

Figure 3. 2 Transmission electron micrographs of (A) mesoporous polydopamine nanoparticles and (B) palladium nanoparticle (Pd NP)-loaded mesoporous polydopamine nanoparticles (black dots represent Pd nanoparticles). (C) HRTEM image of a single Pd NP on the mPDA nanoparticle. Scanning electron micrographs of top surface of the (D) BNC membrane, (E) mPDA-BNC membrane and (F) Pd NP-loaded mPDA-BNC membrane. (G) XPS spectra of Pd 3d peak after reduction of Pd on the mPDA-BNC membrane. (H) EDX spectrum of Pd-mPDA-BNC showing the formation of metallic palladium. (I) XRD spectrum of the Pd-mPDA-BNC membrane showing the peaks corresponding to palladium nanocrystals.

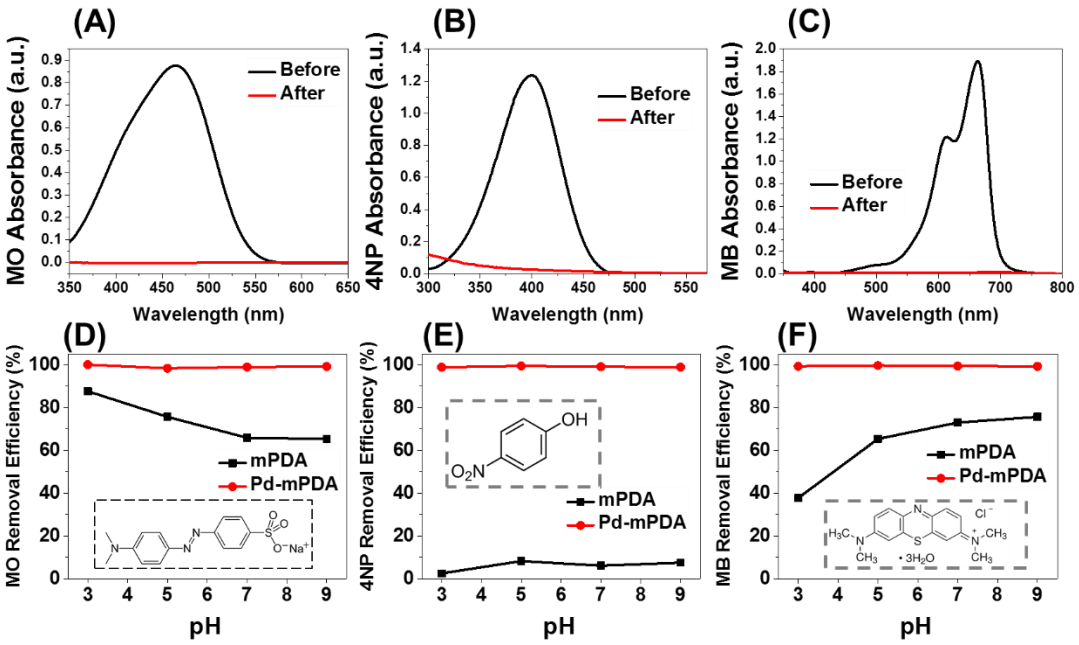

Figure 3. 3 UV–vis spectra showing the degradation of (A) MO, (B) 4NP and (C) MB in the presence of $NaBH_4$ and Pd-mPDA nanoparticles at pH=7. Dye removal performance of the pristine mPDA and Pd-mPDA nanoparticles at different pH for different dyes: (D) negatively charged methyl orange (MO), (E) neutral 4-nitrophenol (4NP) and (F) positively-charged methylene blue (MB) (insets show the chemical structure of each dye molecule).

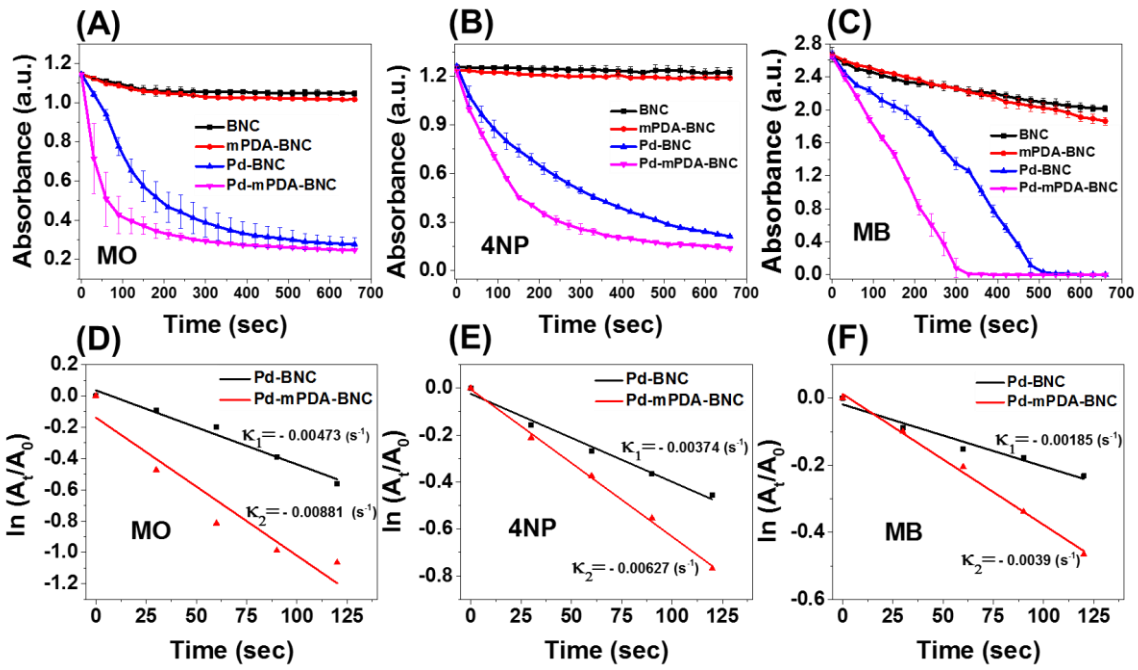

Figure 3. 4 Plots showing the degradation of different membranes for (A) MO, (B) 4NP and (C) MB in the presence of $NaBH_4$ over time. Langmuir–Hinshelwood apparent reaction rate constant for degradation of (D) MO, (E) 4NP and (F) MB in the presence of Pd-mPDA-BNC and Pd-BNC.

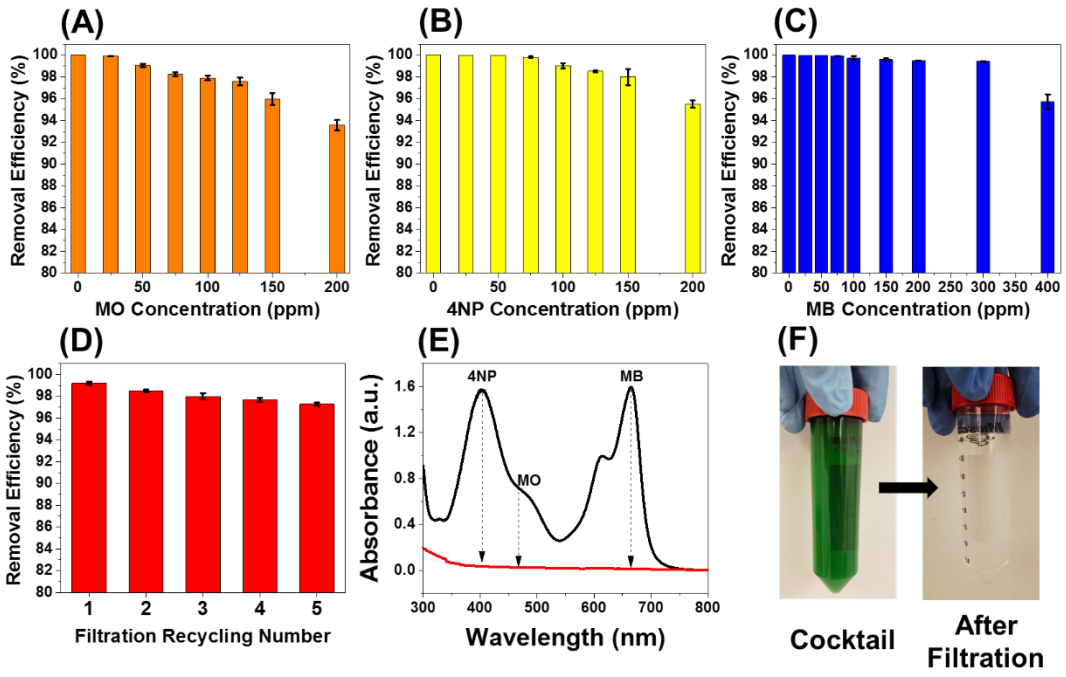

Figure 3. 5 Dye removal efficiency of Pd-GO-BNC membrane at different (A) MO, (B) 4NP and (C) MB concentrations. (D) Dye removal efficiency of the Pd-mPDA-BNC membrane over multiple cylces of filtration/regenarations showing the reusability of the membranes. (E) UV–vis spectra showing the dye removal from a cocktail (50 mL) of organic contaminants: MO, 4-NP, and MB (each with a concentration of 10 ppm) in the presence of $NaBH_4$ (2.5 mM). (F) Photographs showing the organic dye cocktail before and after filtration treatment.

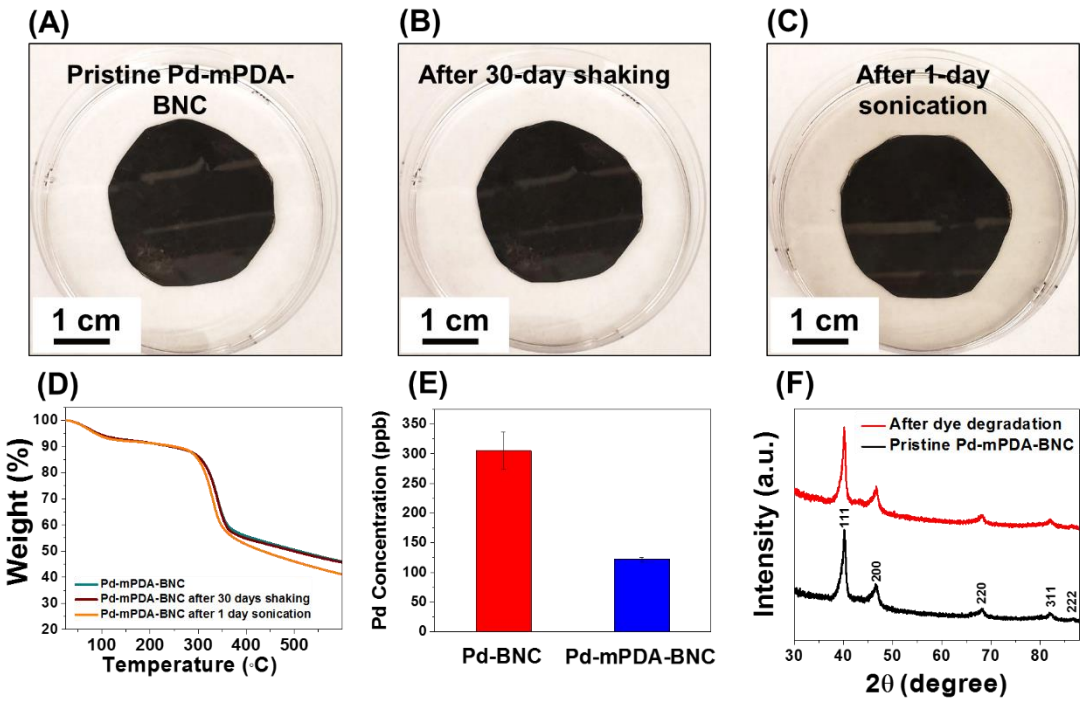

Figure 3. 6 Optical images of (A) Pristine Pd-mPDA-BNC membrane, (B) after 30-day mechanical shaking and (C) after 1-day ultrasonication. (D) TGA of pristine Pd-mPDA-BNC, after 30-day mechanical shaking and 1-day sonication showing the Pd particle loss percentage during the process. (E) Concentration of Pd leaked into solution after mechanical shaking of Pd-BNC and Pd-mPDA-BNC membranes showing better stability of the latter membrane compared to the former. (F) The XRD spectra before and after the dye degradation filtration experiment showing the intact Pd nanocrystals, which serve as the catalyst.

Chapter 4: Polydopamine-Mesoporous Silica Core-Shell Nanoparticles for Combined Photothermal-Immunotherapy

4.1 Introduction

Immunotherapy has proven to be a successful therapeutic approach for cancer with long-lasting effects. However, only a limited fraction of patients is completely cured by standalone immunotherapy. A primary cause of the low response rate is the "immunoediting" employed by cancer in an immuno-competent host to escape surveillance.[169-171] Cancer cells downregulate antigenic proteins and peptides, upregulate immune-inhibitory receptors and express/secrete immuno-suppressive factors to effectively create a pro-tumor microenvironment.[172] The primary goal of immunotherapeutic interventions is to restore the lost immunogenicity and reverse the immuno-suppressive microenvironment in the tumor.[173-174] Toll-like receptor (TLR) agonists and immunomodulatory vaccine adjuvants such as polyinosinic:polycytidylic acid (Poly(I:C)), cytosine-phosphorothioate-guanine (CpG), imiquimod, and resiquimod reprogram the tumor microenvironment (TME). These TLR agonist act either alone or in combination with other treatment modalities such as chemotherapy, photodynamic therapy (PDT), radiotherapy or photothermal therapy (PTT) for generation of potent anti-tumor immune response.[175-180]

An ideal combination immunotherapy involves a "tumor killing" modality including PTT, PDT, or chemotherapy, that should partially ablate the tumor and release tumor-associated antigens (TAAs) and damage associated molecular patterns (DAMPs). The released TAAs and DAMPs synergize with immunomodulatory drugs to create a tumor-inhibitory environment. In previous studies, the two components-i) chemo/photothermal/photodynamic agents; and ii) the

immunomodulators, are co-delivered either in the form of a simple physical mixture or co-encapsulated in a drug delivery vehicle.[181-185] With these therapeutic approaches, there is no external control over the release profile or the bioavailability of the therapeutic agents once the formulation is administered inside the body. The lack of external control over the cargo release leads to differential release kinetics of antigen and adjuvant. This compromises the efficacy of the innate immune response and subsequent adaptive immune response. For eliciting cytotoxic anti-tumor immune response, the internalized antigen must undergo cross-presentation, which includes MHC I-restricted presentation to $CD8^+$ T cells.[186-187] For optimum cross-presentation by APCs, the antigen and adjuvant should preferentially be exposed simultaneously to the APCs.[188] If the APCs are exposed to adjuvant first, it leads to their activation and maturation, which in turn leads to down-regulation of phagocytosis and cross-presentation compromising the overall anti-tumor immunity.[189-190] On a contrary, if the APCs are exposed to antigen first in the absence of adjuvants, then the APCs cross-present the antigen in the absence of co-stimulatory receptors (e.g., CD40, CD80), which leads to generation of immunological tolerance and anergy.[191-193] Both of these scenarios (antigen first in the absence of adjuvant and *vice versa*) result in sub-optimal anti-tumor immune response, thus underscoring the importance of innovative delivery approaches for spatiotemporally orchestrating the availability of antigens and adjuvant for APCs.

Here, we aim to achieve concurrent release of antigen and adjuvant by photothermally ablating the tumor cells for release of TAAs and simultaneously triggering the release of adjuvant. Towards this goal, we have designed and synthesized polydopamine (core) - mesoporous silica (shell) nanostructures that enable photothermal tumor ablation owing to the photothermal properties of the PDA nanostructures and simultaneous release of the adjuvant contained in the mesoporous silica shell. Recently, polydopamine has attracted increased attention as a bio-

inspired, biocompatible, and biodegradable photothermal material for various biomedical applications.[1, 3, 61-65] Mesoporous silica, which is employed as shell, exhibits excellent biocompatibility, and complete degradation into non-toxic components making it an attractive candidate as a drug carrier.[66] We harnessed mesoporous silica shell for controlled release of gardiquimod, a toll-like receptor 7/8 (TLR 7/8) agonist, known to improve cell-based or combination immunotherapies for various cancers.[194-197] Mesoporous silica was loaded with a mixture of gardiquimod and a phase change material, 1-tetradecanol, which served as a "gate keeper" for near infrared (NIR) light-controlled release of the cargo. We engineered the core-shell nanoparticles to generate locoregional heat to ablate the tumor cells and simultaneously release the adjuvant through melting of the phase change material upon heating caused by NIR irradiation (Figure 4.1A). The concurrently released antigens (upon tumor ablation with NIR irradiation) and adjuvant causes effectual activation of dendritic cells, which in turn activate the $CD8^+$ T cells in the tumor draining lymph nodes. The activated cytotoxic effector T cells not only eliminate the residual primary tumor but also inhibits recurrent secondary tumors (Figure 1B). Using these multifunctional nanoparticles, we demonstrate robust photothermal-immunotherapeutic response using NIR light as an external trigger.

4.2 Results and Discussion

4.2.1 Synthesis and characterization of mesoporous silica-polydopamine nanoparticles (PDA@mSiO$_2$)

Spherical PDA nanoparticles are synthesized by oxidative self-polymerization of dopamine monomer in water−ethanol−ammonium mixture at room temperature.[10] By controlling the

amount of ammonium hydroxide, spherical PDA particles with a diameter of 260 ± 32 nm were synthesized (Figure 4.2A, E). Subsequently, silica shell was formed around the PDA nanoparticles using modified Stöber method.[198] For forming nanoscale pores within the silica shell, cetyltrimethylammonium bromide (CTAB), which serves as a porogen, was added to the reaction mixture. Following the formation of the shell, CTAB was removed through ion exchange.[199] The resulting core-shell nanostructures exhibited highly porous structure with buckled surface (Figure 4.2B, F). The as-prepared silica-coated PDA nanoparticles did not exhibit buckling on their surface (Figure S4.1). The surface buckles appeared after refluxing the core-shell particles in ammonium nitrate solution to remove the porogen (*i.e.* CTAB). The differential thermal stresses at the core-shell interface developed during reflux process (at 45°C for 24 hours) possibly result in the buckled surface morphology of the nanostructures. The thickness of the mesoporous silica coating was found to be ~100 nm as measured by dynamic light scattering (Figure 4.2C). Both PDA and PDA@mSiO_2 exhibited negative zeta-potential (~-30 mV) at physiological pH of 7.4 (Figure 4.2D). The pore size distribution of the PDA@mSiO_2 nanoparticles exhibited a sharp peak at 3.1 nm, confirming the mesoporous nature of the shell (Figure 4.2G). Scanning transmission electron microscopy-energy dispersive X-ray spectroscopy elemental mapping of N and Si delineated the PDA core and silica shell, as evidenced by the presence of N and Si in the core and shell, respectively (Figure S4.2). Thermogravimetric analysis (TGA) of the pristine PDA nanoparticles and PDA@mSiO_2 nanoparticles indicated that silica shell corresponds to about 53% of the weight of the PDA@mSiO_2 nanoparticles (Figure 4.2H).

4.2.2 Photothermal and controlled release properties of PDA@$mSiO_2$ nanoparticles

Polydopamine and PDA@$mSiO_2$ nanoparticles exhibited broad light absorption over visible and NIR parts of the electromagnetic spectrum (Figure S4.3A). To explore the NIR-induced heating of PDA@$mSiO_2$ nanoparticles and dynamics of the temperature increase, different concentrations of PDA@$mSiO_2$ nanoparticles in water were subjected to 808 nm laser irradiation at a power density of 14 mW/mm^2. For 300 seconds of laser irradiation, the temperature increased monotonically and reached to a maximum of 57°C for PDA@$mSiO_2$ nanoparticles solution with a concentration of 1000 µg/ml (Figure 4.3A). As expected, the maximum temperature increased with an increase in the nanoparticle concentration (Figure 4.3B). Temperature rise of the core-shell nanoparticle solution under NIR irradiation ranged from 10°C to 30°C for concentrations ranging from 100-1000 µg/ml. In contrast, temperature of de-ionized water increased by only 2°C under identical NIR irradiation conditions. Following the NIR irradiation for 20 min, no discernable changes in the shape or pore structure of the core-shell nanoparticles were observed, indicating the stability and applicability as drug carriers for controlled release (Figure S4.3B). The photothermal efficiency was calculated and found to be 56.8% (See discussion in Supporting Information).

Next, we investigated the loading and controlled release of cargo from core-shell nanostructures using 1-tetradecanol as gate keeper. 1-Tetradecanol, a biocompatible phase changing material, exhibits melting temperature of 38-39°C, which is slightly above the normal human body temperature. Consequently, 1-tetradecanol can contain the cargo in the nanoparticles at body temperature with minimal leakage and enable triggered release of the contents by external

heating.[200] A model dye, Rose Bengal (RB), mixed with 1-tetradecanol was loaded into the nanostructures. As discussed above, under NIR irradiation, PDA@$mSiO_2$ nanoparticles exhibited temperature rise, enough to melt 1-tetradecanol and release the cargo. The RB-loaded PDA@$mSiO_2$ nanoparticles solution was concentrated to 4 mg/ml and subjected to NIR laser (14 mW/mm^2) to trigger the release. During the first 5 minutes of the treatment, the solution temperature raised steadily followed by saturation at ~70°C for the subsequent 15 min of irradiation (Figure 4.3C). As the temperature increased to above the melting point of the 1-tetradecanol within 1 minute, the optical absorbance of RB in the surrounding aqueous medium started to increase, indicating the NIR-triggered release of the dye from the nanoparticles (Figure 4.3C, D). The cumulative absorbance of the dye steadily increased for the subsequent 20 min indicating the continuous release of the dye from the nanostructures. In stark contrast, the RB-loaded PDA@$mSiO_2$ nanoparticles solution incubated at room temperature (25°C) for 1 day exhibited a leakage of only 1.5%, which shows their excellent ability to contain and release the payload only under an external trigger. Successful loading and controlled release of the payload from PDA@$mSiO_2$ nanoparticles was further confirmed using a fluorescent dye (see Figure S4.5A and discussion in Supporting Information).

4.2.3 Photothermal therapeutic efficacy and immune-stimulatory effect of gardi-mPDA nanoparticles

Now we evaluated the *in vitro* photothermal therapeutic efficacy of the gardiquimod-loaded PDA@$mSiO_2$ (called gardi-mPDA henceforth) nanoparticles. The encapsulation efficiency of gardiquimod in nanoparticles was determined to be 11 ± 3 μg/mg (see Experimental section).

B16-F10 melanoma cells were incubated with different concentrations of gardi-mPDA nanoparticles, followed by 10 minutes of laser irradiation (14 mW/mm^2). For all concentrations of gardi-mPDA nanoparticles, a significant decrease in viability was observed in NIR treated cells compared to cells without NIR treatment (Figure 4.3E). Importantly, without NIR irradiation, no toxicity was observed, indicating that the adjuvant-loaded particles by themselves are not cytotoxic. For efficient photothermal cytotoxicity the nanoparticles should physically interact with cancer cells. The nanoparticle-cell interaction was assessed by incubating B16-F10 cells with LT680-loaded PDA@$mSiO_2$ (LT680-mPDA) followed by confocal fluorescence microscopy. We observed punctate-like LT680 signal from the cells confirming physical nanoparticle-cell interaction (Figure S4.5B).

After confirming the *in vitro* photothermal therapeutic efficacy of the gardi-mPDA nanoparticles, we investigated their immuno-stimulatory potential upon NIR-triggered release of gardiquimod. Bone marrow derived dendritic cells (BMDCs) were treated with supernatants collected from gardi-mPDA (100 μg/ml) subjected to 10 minutes of NIR treatment. Concentration of secreted interleukin 6 (IL-6) and tumor necrosis factor-α (TNFα), which indicate the activation of BMDCs, were measured and compared to secretion levels of BMDCs treated with free gardiquimod. There was a significant increase in cytokine secretion following the treatment of BMDCs with supernatant of NIR treated gardi-mPDA nanoparticles compared to supernatant without NIR treatment (Figure 4.3F, G). Similar results were observed for upregulation of maturation markers (CD40 and CD80), where supernatants collected from NIR-treated nanoparticles led to significant increase in BMDC maturation as compared to without NIR treatment (Figure S4.4). It is important to note that CD40 and CD80 serve as co-stimulatory signal for efficient activation of $CD8^+$ T cells. These results indicate that gardiquimod can be

released with external trigger and the photothermally released gardiquimod is therapeutically active.

4.2.4 Combined photothermal-immunotherapy effect of gardi-mPDA nanoparticles

After confirming the *in vitro* photothermal therapeutic efficacy of PDA@mSiO$_2$ nanoparticles and immuno-stimulatory effect of gardi-mPDA nanoparticles independently, we set out to answer two key questions: (i) Does the NIR treatment of cancer cells incubated with gardi-mPDA nanoparticles release both the TAAs and adjuvant concurrently; and (ii) is the released adjuvant from the cancer cells capable of causing immunostimulatory effect? To address these questions, B16-F10 cells were treated with LT680-mPDA and then loaded with a cell-permeable protein-labelling dye, carboxyfluorescein succinimidyl ester (CFSE). Here, LT680 serves as model drug loaded in mPDA and CFSE labelled intracellular proteins serve as representative tumor antigen. The cells were harvested and divided into two groups: with and without NIR treatment (Figure 4.4A). The supernatants collected from both groups were analyzed for LT680 and CFSE fluorescence. The NIR treatment demonstrated significant increase in fluorescence intensity of both LT680 and CFSE as compared to without NIR treatment (Figure 4.4B, C). These results indicate the ability of PDA@mSiO$_2$ nanoparticles to simultaneously release the loaded drug and protein antigen from the cells when treated with NIR light. Next, we incubated B16-F10 cells with gardi-mPDA nanoparticles and subjected them to NIR treatment to induce the release of gardiquimod from internalized and cell surface bound nanoparticles. Subsequently, BMDCs were treated with the above mentioned B16-F10 cell culture supernatant to assess the activation ability of the released gardiquimod. Clearly, the cell culture supernatant resulted in activation of BMDCs as evidenced by the increase in the secreted IL-6 concentration, further

confirming the NIR-assisted release of gardiquimod from within the cancer cells and its immunomodulatory effects (Figure 4.4D).

4.2.5 In vivo photothermal efficiency and externally triggered release of payload

To further investigate the photothermal efficacy of the PDA@mSiO$_2$ nanoparticles *in vivo*, subcutaneously inoculated B16-F10 mouse melanoma model was used. One day after the administration of the nanoparticles, tumors were irradiated with an NIR laser for 5 minutes (laser power 6 and 14 mW/mm^2). Mice without nanoparticle injection were employed as control group. After laser irradiation at a power density of 14 mW/mm^2 for 5 minutes, the tumor temperature for the control group without nanoparticle injection reached 40°C. In contrast, under identical irradiation conditions, the tumor temperature for the mouse injected with PDA@mSiO$_2$ nanoparticles, increased to 81 °C, indicating the high photothermal efficiency of PDA@mSiO$_2$ nanoparticles in converting NIR light to heat and inducing locoregional cell ablation (Figure S4.6A, B). *In vivo* fluorescence imaging of the tumors after injection of LT680-mPDA revealed nearly two-fold increase in fluorescence after subjecting the tumors to NIR irradiation for 5 minutes as compared to without NIR treatment, confirming that the dye encapsulated in nanoparticles, is diffusing outward and restoring fluorescence after successful NIR triggered release from the nanoparticles (Figure S4.6C, D).

4.2.6 In vivo therapeutic efficacy of gardi-mPDA

After confirming *in vitro* photothermal therapeutic efficacy and successful release of payload under NIR irradiation, we investigated the therapeutic potential of gardi-mPDA *in vivo.* The release of tumor antigen after photothermal ablation of tumor cells and concurrent release of

adjuvant is critical for robust anti-tumor immune response. We employed B16-F10 melanoma model and intra-tumorally injected the gardi-mPDA nanoparticles followed by NIR treatment (808 nm, 14 mW/mm^2) (Figure 4.5A). The first step was to assess the biocompatibility of nanoparticles for which the body weight of the mice was monitored. No significant difference was observed in the body weight of the mice treated with PDA@$mSiO_2$ or gardi-mPDA nanoparticles indicating that the nanoparticles did not cause any severe systemic toxicity (Figure 4.5B). Tumor growth was monitored for different treatment groups and we noted that the gardi-mPDA nanoparticles treated with NIR resulted in significant inhibition of tumor growth compared to gardi-mPDA nanoparticles without NIR, PDA@$mSiO_2$ nanoparticles with NIR and PBS group (Figure 4.5C). The survival rate of mice treated with gardi-mPDA nanoparticles and NIR was ~57% at day 43, while all the other groups had 0% survival rate at day 30 (Figure 4.5D). Notably, the tumors for mice treated with PDA@$mSiO_2$-NIR exhibited inhibition in tumor growth (due to photothermal tumor ablation) until day 10-11 while the tumors for mice treated with PBS or gardi-mPDA without NIR demonstrated constant growth (Figure 4.5E, F, G). However, the effect of PDA@$mSiO_2$-NIR was not long-lasting as the tumor cells, which survived photothermal ablation started growing, ultimately resulting in the formation of tumors equivalent in size to that of gardi-mPDA group at day 19. Although PDA@$mSiO_2$-NIR group is expected to release abundant tumor associated antigens during photothermal ablation, the presence of antigen without adjuvant resulted in sub-optimal therapeutic effect. In the other control group where the mice were treated with gardi-mPDA, adjuvants were available to tumor resident antigen-presenting cells (APCs) as the nanoparticles are eventually expected to be uptaken by APCs followed by their activation (Figure 4.6).

The gardi-mPDA treated mice showed moderate inhibition in tumor growth, which is possibly due to the reversal of immuno-suppressive microenvironment in tumor caused by TLR7/8 agonism.[201] More specifically gardiquimod is known to impart tumor-killing potential to plasmacytoid dendritic cells.[202] The moderate inhibition of tumor growth observed in mice treated with PDA@mSiO_2-NIR and gardi-mPDA without NIR was not robust and short-lived as it eventually lead to 100% mortality until day 30. Mice treated with gardi-mPDA-NIR demonstrated dramatic inhibition in tumor growth emphasizing the role of simultaneous release of antigen and adjuvant (Figure 4.5H). The released antigen and adjuvants from the photothermally ablated tumor cells are available to APCs, which are expected to migrate to the tumor draining lymph nodes where they activate the $CD8^+$ T cells. These effector immune T cells are capable of eradicating the residual tumors, which survive the primary photothermal ablation. The mice surviving primary tumor challenge were able to significantly inhibit growth of secondary tumors indicating the generation of long-term memory response, when compared to age-matched naïve mice (Figure 4.5I). The biocompatibility of these nanoparticles was further confirmed by histopathological staining. We observed no signs of cell death, confirming no systemic toxicity in the visceral organs of the mice after treatment with gardi-mPDA-NIR (Figure 4.5J).

Since the primary tumors were temporarily attenuated by photothermal effect caused by PDA@mSiO_2-NIR, we reasoned if the increase in NIR treatment duration from 5 minutes to 10 minutes could result in complete ablation of tumor growth without the need for immunotherapy. We treated the mice with PDA@mSiO_2 and gardi-mPDA followed by NIR treatment for 10 minutes (Figure S4.9A). NIR treatment for 10 minutes was well tolerated by mice as it did not cause any decrease in the body weight of the mice (Figure S5.9B). Interestingly, both

PDA@mSiO$_2$-NIR and gardi-mPDA-NIR resulted in significant inhibition of tumor growth (Figure S4.9C). While less than half (40%) of the mice in PDA@mSiO$_2$-NIR group survived at, 80% of mice in gardi-mPDA-NIR survived at day 46 with no observable signs of primary tumor (Figure S4.9D). In order to evaluate the long-term efficacy of both photothermal therapy and photothermal-immunotherapy the tumor-free mice from primary challenge were subjected to secondary tumor challenge on the opposite flank. It was observed that the mice treated with concurrent photothermal-immunotherapy had better resistance to tumor growth as compared to just photothermal therapy (Figure S4.9E). Taken together, these results emphasize the significance of both specificities associated with the tumor-associated antigens and immune-stimulatory capabilities of the adjuvant for generation of robust and long-lasting anti-tumor immune response.

4.2.7 In vivo immune status in tumor draining lymph node

The population and activation status of immune cells in the tumor draining lymph nodes was assessed to understand the role of immune cells in therapeutic effect. Increased percentage of both T cells and dendritic cells (DCs) was observed in tumor draining lymph nodes of mice treated with gardi-mPDA-NIR. Specifically, presence of $CD3^+CD8^+$ T cells was analyzed, and we observed that while PDA@mSiO$_2$-NIR resulted in a modest increase in T cells, gardi-mPDA nanoparticles irrespective of the presence or absence of NIR resulted in almost two-fold increase in T cell count compared to PBS (Figure 4.6A). Maturation of DCs was assessed by measuring the expression levels of maturation markers (CD40, CD80, MHC II). We observed higher activation of DCs with gardi-mPDA treated groups compared to PDA@mSiO$_2$-NIR or PBS group. PDA@mSiO$_2$-NIR has relatively mild immuno-stimulatory potential in the absence of potent adjuvants. Despite having significant immuno-stimulatory effect, the influence of gardi-

mPDA is non-specific because of lack of specific tumor associated antigen (Figure 4.6B, S4.7, S4.8). This signifies that the presence of both antigen and adjuvant is critical for generation of long-lasting immune response. Externally triggered NIR facilitated the release of both antigen and adjuvant simultaneously, thus orchestrating a highly potent tumor-specific immune response.

4.3 Conclusion

To summarize, we designed and synthesized a core-shell nanostructure based on highly biocompatible and completely biodegradable components, where the photothermal property of the core was integrated with NIR-responsive drug release properties of the shell for ultimately generating a robust and long-lasting anti-tumor immune response. PDA nanoparticles were employed as a photothermal core and mesoporous silica shell was used as the carrier for a mixture of phase-change material (1-tetradecanol) and immune-stimulating agent (gardiquimod). These nanoparticles were effectively uptaken by cancer cells and led to concurrent release of both antigen and adjuvant from the cancer cells upon NIR irradiation. The external trigger NIR facilitated spatiotemporal control of the therapeutic events for ultimately mounting a potent anti-tumor immune response. The core-shell nanoparticle design is universal and is amenable for loading other types of immunomodulatory or chemotherapeutic drugs or their combinations for synergistic effects. The versatility and unique design of these multifunctional nanoparticles can be harnessed for improved photothermal-immunotherapeutic treatments acting as a powerful platform for cancer treatment.

4.4 Experimental Section

Preparation of PDA nanoparticles coated with mesoporous silica shell (PDA@mSiO2): All chemicals are purchased from Millipore Sigma, St. Louis, MO, USA and used without further

purification, unless or otherwise mentioned. Polydopamine nanoparticles were synthesized by using a method reported previously.[10] Briefly, 112 mL of ethanol was mixed with 252 mL of deionized (DI) water (resistivity of 18.2 MΩ·cm) in a glass container. Subsequently, 4.2 mL of aqueous solution of ammonia (28−30% NH_4OH) was added into the above water/ethanol mixture. After stirring for 30 minutes, dopamine hydrochloride (1.4 g in 28 mL water) was added to the reaction mixture. The reaction was left under gentle magnetic stirring for 24 hours. The PDA particles were collected by centrifugation (9000 rpm, 10 minutes) and washed with DI water five times and dispersed in water.

To form mesoporous silica shell on PDA particles, 0.8 ml of polydopamine solution (8 mg/ml in water) was mixed with 0.4 ml of cetyltrimethylammonium bromide (CTAB, 0.1 M) and stirred at 30 ºC for 10 minutes. Then, 0.2 ml tetraethyl orthosilicate (TEOS, 17% v/v in ethanol) was added to the mixture under vigorous stirring. After 10 minutes, 5 µl of ammonium hydroxide (NH_4OH, 30% in water) was added and the mixture was left stirring at room temperature for 15 hours. The core-shell particles were washed three times with water and then three times with ethanol and dispersed in ethanol. To remove the template of CTAB, particles were dispersed in ammonium nitrate solution (NH_4NO_3, 60 ml, 10 mg/ml in ethanol) and refluxed at 45 ºC for 24 hours. The mesoporous silica-coated PDA nanoparticle were washed five times with ethanol and dispersed in ethanol.

Drug Loading : Loading of drugs into PDA@mSiO_2 nanoparticles using 1-tetradecanol (TD) as gatekeeper was carried out following previous reports with some modifications.[203] Typically, 1-tetradecanol (4 mg) was mixed with gardiquimod 1-(4-amino-2-ethylaminomethylimidazo-[4,5-c]quinolin-1-yl)-2-methylpropan-2-ol (50 µl, 5 mg/ml in ethanol) in a round-bottom glass tube. The glass tube was heated to 75 ºC under mild stirring and left for 20 minutes. Subsequently,

PDA@$mSiO_2$ nanoparticle solution (8 mg in 200 µl ethanol) was added to the mixture and temperature was increased to 90 ºC. The mixture was stirred for about 1 hour until the ethanol completely evaporated. The particles were resuspended by adding hot water (1 ml, 80 ºC) followed by sonication for 5 seconds. The mixture was immediately centrifuged (9000 rpm, 10 min) and supernatant discarded. Drug-loaded particles were dispersed in cold water and washed with water 10 times to remove free drug in solution. The loading amount of gardiquimod was measured by dispersing the gardiquimod-loaded nanoparticles in acetone followed by 20 minutes of sonication to extract the gardiquimod and TD into acetone. The UV-vis absorption at 329 nm was used to estimate the amount of loaded gardiquimod. The drug loading efficiency was calculated according to the following equation:

$$\text{Encapsulation efficiency} = \frac{\text{mass of drug loaded (µg)}}{\text{mass of nanoparticle (mg)}}$$

To load the Rose Bengal and LT680 dyes, similar procedure was followed. The loading amount for Rose Bengal (UV absorption at 545 nm) was found to be 11.25 µg/mg.

Nanoparticle characterization

Transmission electron microscope (TEM) images were obtained using a JEOL JEM-2100F field emission microscopy. Scanning electron microscopy (SEM) images were obtained using a JEOL JSM-7001 LVF field-emission scanning electron microscope. High resolution transmission electron microscope (HRTEM) images and EDX elemental mappings were obtained using a JEOL JEM-2100F field-emission STEM. Thermogravimetric analysis (TGA) was performed in nitrogen using a TA Instruments Q5000 IR thermogravimetric analyzer at a heating rate of 5 ºC $minute^{-1}$. Dynamic light scattering (DLS) and zeta potential measurements were performed using

Malvern Zetasizer (Nano ZS). Shimadzu UV-1800 spectrophotometer was employed for light absorption measurements. The pore size distribution was estimated from nitrogen adsorption/ desorption isotherms by using Barrett-Joyner-Halenda (BJH) method and a surface area analyzer (Autosorb-1C).

NIR-induced heating and drug release profiles

Aqueous solutions of pristine PDA@$mSiO_2$ nanoparticles at different concentrations (0-1000 µg/ml) were prepared in a 1 ml cuvette. NIR laser (808 nm) was placed on top of the cuvette at a distance of ~10 cm to deliver 14 mW/mm^2 power density to the top of the solution. The temperature rise for different particle concentrations was monitored over 9 minutes by an IR camera (ICI 7320 USB camera). Temperature rise of water under identical irradiation conditions was recorded for comparison.

For probing the NIR-triggered release profile, Rose Bengal (RB) was used as a model dye. 1 ml of RB-loaded PDA@$mSiO_2$ nanoparticles was concentrated to 400 µl solution. 200 µl of the concentrated particles was irradiated by NIR laser (808 nm) at power density of 14 mW/mm^2. At specific times during laser treatment, 15 µl of the solution was extracted and diluted to 400 µl in water and centrifuged immediately. The optical absorbance of RB within the supernatant was measured using UV-vis spectrometer. The corresponding solution temperature for each time point was measured using an IR camera. Similar procedure was followed for NIR-triggered release of LT680 (fluorescent dye) from PDA@$mSiO_2$ nanoparticles. The LICOR Odyssey CLx scanner was used to measure the fluorescence intensity of the supernatant.

Cell culture, BMDC isolation and animal model

The B16-F10, a murine melanoma cell line, was purchased from American type culture collection (ATCC). Cells were maintained in Dulbecco's Modified Eagle's Medium (DMEM, Gibco) with 10% fetal bovine serum (FBS, Gibco), 100 U/ml penicillin and 100 µg/ml streptomycin. Female C57BL/6 (H-2b) mice that were 6 to 8 weeks of age were purchased from Jackson Labs (Bar Harbor, ME, USA). The mice were maintained under pathogen-free conditions. All experiments employing mice were performed in accordance with laboratory animal protocol approved by the School of Medicine Animal Studies Committee of Washington University in St. Louis. Mouse were euthanized using CO_2 asphyxiation and cervical dislocation. The euthanized mouse was kept in 70% (v/v) ethanol for 1 min. Both the femurs and tibiae were isolated, and the muscle attachments were carefully removed using gauze pads. Both ends of the bones were cut with scissors and the marrow was centrifuged in an adapted centrifuge tube (0.6 ml tube with a hole inserted in 1.5 ml tube) at 1000 rpm for 10 seconds. The pellet was resuspended by vigorous pipetting in RPMI 1640 media. The cells were passed through a 70 µm cell strainer to prepare a single cell suspension. After one wash (1200 rpm, 5 min), red blood cells were depleted with RBC lysis buffer (Sigma-Aldrich). The bone marrow cells were collected and cultured in 100-mm Petri dishes containing 10 ml RPMI medium supplemented with 10% heat-inactivated FBS, 50 IU/ml penicillin, 50 µg/ml streptomycin, and 20 ng/ml mouse recombinant granulocyte- macrophage colony-stimulating factor (GM-CSF, R&D Systems, MN, USA).

Photothermal cytotoxicity assay

For probing the photothermal efficacy of PDA@mSiO_2 nanoparticles, $1x10^4$ B16-F10 cells in 100 µl of media/well were seeded in a 96-well plate and kept at 37^oC with 5% CO_2 for 12 hours. Cells were incubated with different concentrations of PDA@mSiO_2 nanoparticles for 6 hours

after which they were subjected to 808 nm laser for 10 minutes at a power density of 14mW/mm^2. After 24 hours, MTS assay was performed as per manufacturer protocol.

BMDC activation and maturation

BMDCs (1x10^6) were seeded on a 6-well plate in 1 ml of media. The cells were treated with supernatants collected after centrifuging 100 µg/ml gardi-mPDA nanoparticles at 8000 rpm for 10 minutes. For gardi-mPDA-NIR, the particles were treated with 10 minutes of 808 nm laser (14mW/mm^2) right before centrifugation. The collected supernatants were added to BMDCs and incubated for 24 hours. The cells were harvested using a cell scraper and centrifuged at 1000 rpm for 5 minutes. The supernatant was used for assessment of cytokine (IL-6 and TNFα) levels using ELISA (R&D Systems, Minneapolis, USA). The cells were fixed using 10% neutral buffered formalin (NBF) for 20 minutes at room temperature and then washed with PBS. The cells were then blocked using CD16/CD32 (Mouse BD Fc Block™) and stained for APC-CD40 and PE-CD80 followed by analysis using flow cytometry (Acea Novocyte, San Diego, USA).

Uptake of nanoparticles

For studying the uptake of the nanoparticles, BMDCs were treated with 100 µg/ml of LT680-mPDA. After incubating for 1 hour, the cells were washed and fixed with 10% NBF (20 minutes) followed by washing three times with PBS. NIR laser was treated for 2 minutes to release some dye and prevent the LT680 self-quenching. The cells were then stained with DAPI using manufacturer's protocol. The images were acquired using Zeiss LSM 880 Confocal fluorescence microscope.

In vitro combined photothermal and immune-stimulation study

For probing the combined photothermal and immune-stimulation efficacy of nanoparticles, 1×10^6 B16-F10 cells per well were seeded in a 6 well plate followed by incubation with either LT680-mPDA or gardi-mPDA nanoparticles (100 µg/ml). After incubating with the nanoparticles for 1 hour, cells were harvested and washed three times with PBS (1100 rpm, 5 minutes). The cells were then stained with 1 µl of CellTrace™ CFSE (Invitrogen™, Carlsbad, USA) for 20 minutes at room temperature. The cells were then washed with complete media and divided into two groups of $2x10^6$ cells in 100 µl of culture medium. The first group was subjected to 10 minutes of 808 nm laser (14 mW/mm^2) treatment, followed by dilution of cells in 1 ml of culture medium. The second group was directly diluted in 1 ml of medium and the cells from both the groups were seeded in a 6-well plate for incubation at 37°C for 12 hours. Cells from both the groups were harvested and centrifuged at 1100 rpm for 5 minutes. The LICOR Odyssey CLx scanner was used to measure the fluorescence intensity of the LT680 and fluorescence plate reader (Molecular devices, SpectraMax ID3) was used to measure the fluorescence intensity of CFSE in the supernatant. For immune-stimulation study B16-F10 cells were treated with gardi-mPDA instead of LT680-mPDA as described above. The supernatants collected from the two groups were treated on BMDCs ($1x10^6$) seeded in a 6-well plate. Supernatant from BMDCs was collected 24 hours post-treatment and the IL-6 secretion was measured using ELISA (R&D Systems, Minneapolis, USA).

In vivo photothermal efficacy and drug release

Photothermal treatment was performed 1-day post-injection of PDA@$mSiO_2$ nanoparticles into the tumor site. Mouse injected with gardi-mPDA was anaesthetized and subjected to 808 nm laser (power density of 14 mW/mm^2 and laser spot size of 5 mm). The body hair was removed from the tumor site to eliminate the external factors affecting the photothermal heating. The

tumor injected with gardi-mPDA nanoparticles was irradiated with laser for 5 minutes. The corresponding tumor surface temperature was measured using an IR camera. Identical NIR irradiation was performed on a tumor-inoculated mouse without particle injection to collect the tumor surface temperature during treatment, as a control.

For drug release experiment, 7 days after B16-F10 tumor inoculation, mice were scanned using LICOR scanner for background fluorescence. Then 10 µl of LT680-mPDA were adminstered intratumorally, followed by fluorescence imaging one immediately and the other 10 minutes after adminstration. The mice were then subjected to 14 mW/mm^2 808 nm laser treatment for 5 minutes and then imaged. Fluorescence intensity (FI) after particle injection was considered as a reference and the fold increase was calculated for 10 minutes without NIR and with NIR.

In vivo tumor model

Six to eight weeks old C57Bl/6 mice were inoculated on the right flank with $1x10^6$ B16-F10 cells (s.c) in 100 µl of HBSS. On day 6, mice bearing tumor with a diameter of 4-6 mm were selected, numbered and divided into 4 groups (n=7). The mice in different groups were administered 50 µl of PBS, gardi-mPDA, PDA@$mSiO_2$ and gardi-mPDA intra-tumorally. 24 hours after injection, PDA@$mSiO_2$ and one gardi-mPDA group was treated with 808 nm laser (14 mW/mm^2) for 5 minutes. 24 hours allows diffusion within the tumor and uptake of injected nanoparticles by the cancer cells. The body weight and tumor diameters were measured every other day till day 19 after tumor implantation using a sliding caliper. Tumor volume was calculated as following: tumor volume = length × $(width)^2/2$. For survival study, the treated animals were observed for at least 42 days. For secondary tumor challenge, tumor-free mice at day 28 were re-challenged with $5x10^5$ B16-F10 cells on the opposite flank. For histopathological analysis, the heart, kidney,

liver, spleen and lungs were harvested 2 weeks after immunization and processed for hematoxylin−eosin staining.

In vivo flow cytometry analysis

To assess the population of immune cells in tumor draining lymph nodes, the inguinal lymph node from the tumor bearing side was isolated and digested using 0.5 mg/ml collagenase I and 0.1 mg/ml DNAase in DMEM at 37^{o}C for 1 hour. Nylon mesh filter (70 µm) was used to prepare single cell suspension followed by washing three times with PBS. The cells were subjected to blocking using CD16/CD32 (Mouse BD Fc Block™), followed by staining with FITC-CD11c, PE-Dazzle-CD3, FITC-CD8, APC-CD40, PE-CD80 and Per CP-MHC II (eBiosciences, San Diego, USA) for 1 hour at room temperature in dark. The cells were washed three times with PBS and then analyzed using flow cytometry (Acea Novocyte, San Diego, USA).

Statistical analysis

For analyzing the statistical difference between two groups, unpaired two-tailed t-test with Welch's correction was used. For analyzing the statistical difference between more than two groups, one-way ANOVA with post-hoc Tukey’s honest significance test was used. Statistical significance of the data was calculated at 95% ($p < 0.05$) CIs. For analyzing statistical significance in survival data log-rank (ManteleCox) test was used. All values are expressed as mean ± standard deviation from three or more independent or repeated experiments. GraphPad Prism 6 (San Diego, CA, USA) was used for all statistical analysis and Origin and GraphPad was used for creating all figures.

4.5 Supporting Information

Supporting Information for chapter 4 is provided in appendix 3.

4.6 Figures

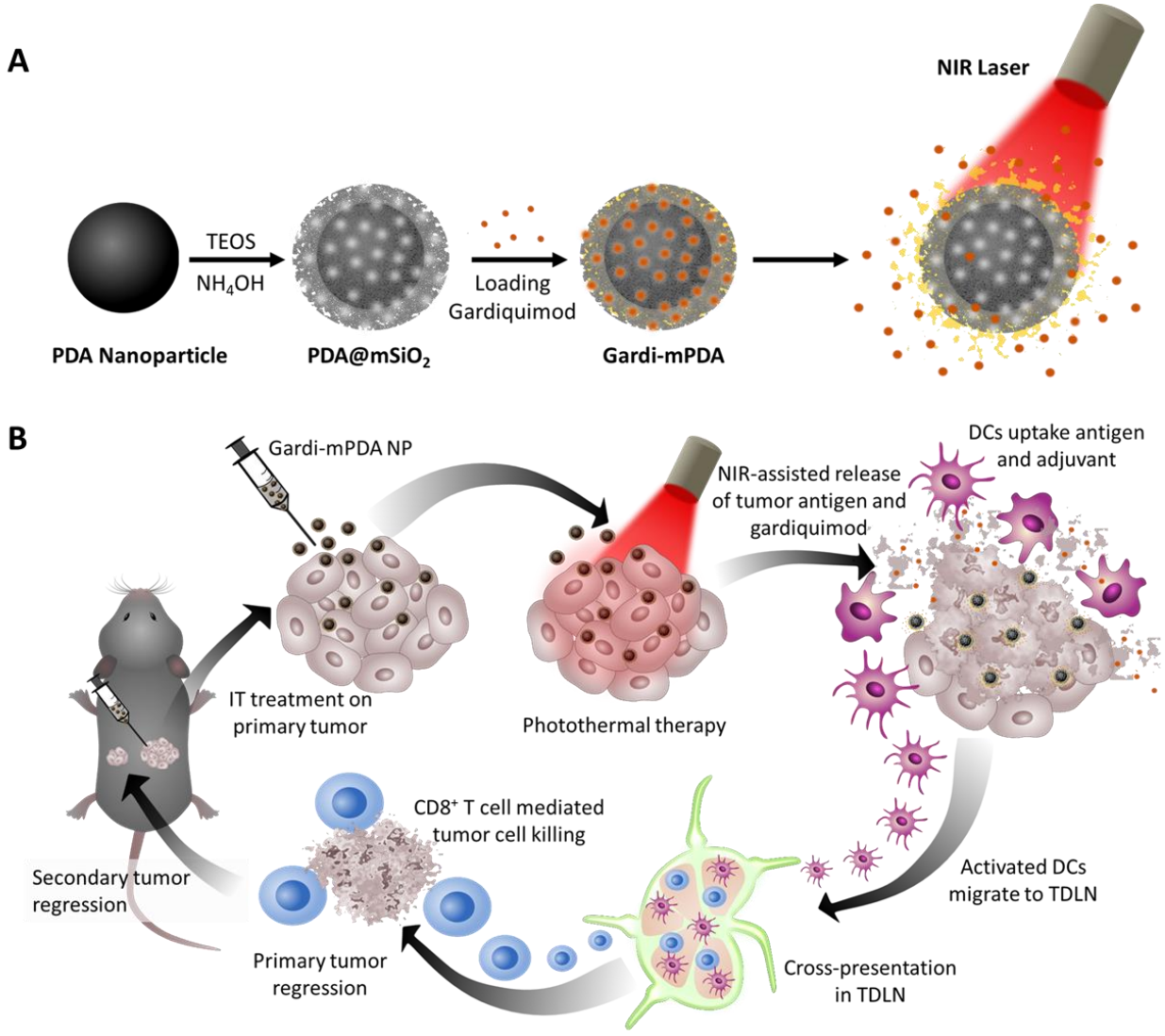

Figure 4. 1 Schematic illustrations depicting (A) Synthesis of gardiquimod-loaded mesoporous silica coated polydopamine nanoparticles (gardi-mPDA) and NIR-assisted drug release. (B) Tumor ablation and drug release under NIR irradiation followed by activation of DCs and effector T cells in tumor draining lymph nodes for regression of primary and secondary tumors.

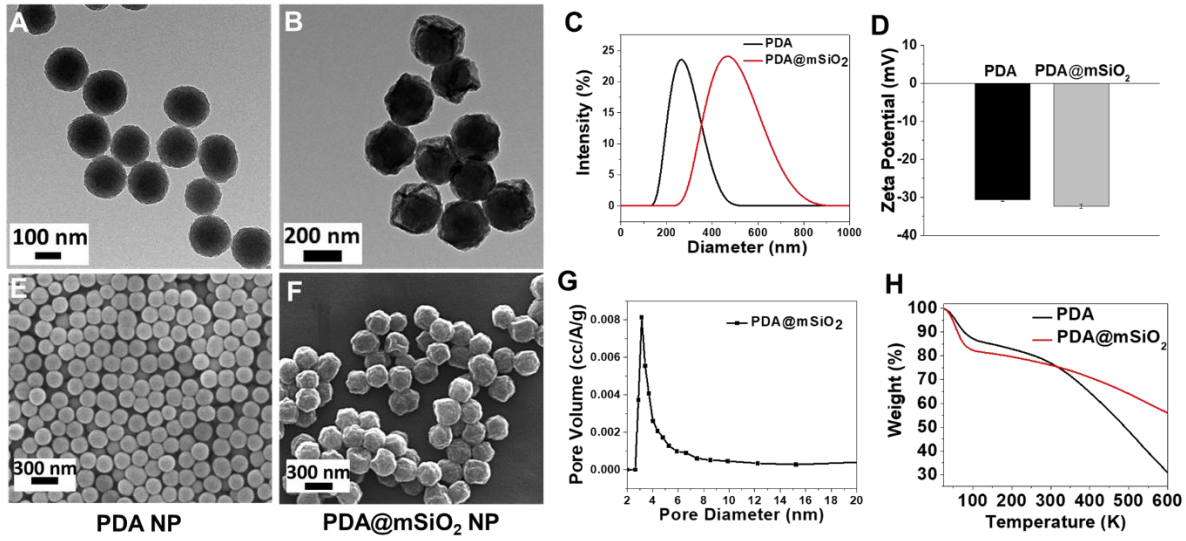

Figure 4. 2 TEM images of the (A) PDA and (B) PDA@mSiO$_2$ nanoparticles. (C) hydrodynamic diameter and (D) zeta potential of the PDA and PDA@mSiO$_2$ nanoparticles. SEM images of the (E) PDA and (F) PDA@mSiO$_2$ nanoparticles. (G) Pore size distribution of PDA@mSiO$_2$ nanoparticles obtained by nitrogen adsorption and using Barrett-Joyner-Halenda (BJH) method. (H) Weight loss profiles of PDA and PDA@mSiO$_2$ nanoparticles as measured by thermogravimetric analysis.

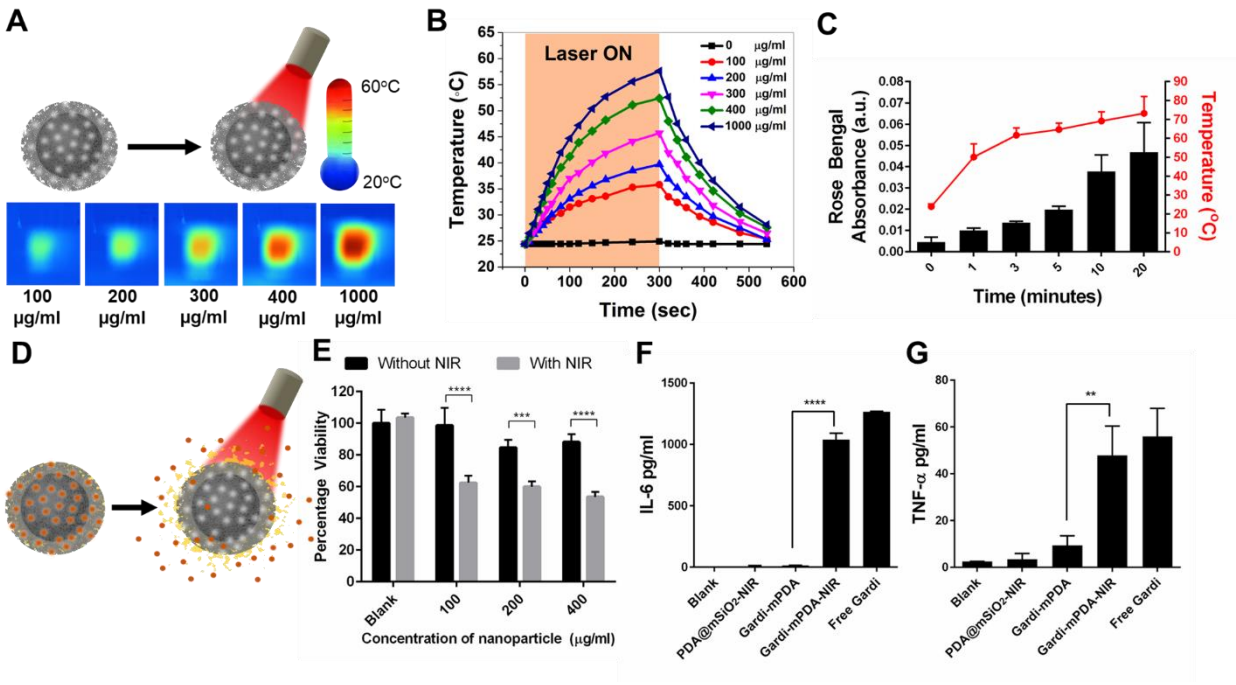

Figure 4. 3 (A) Schematic representation of NIR irradiation of pristine PDA@mSiO$_2$ nanoparticles and IR images of temperature rise with increase in particle concentration after 5 minutes of NIR laser treatment. (B) Temperature profile and effect of PDA@mSiO$_2$ particle concentration on temperature rise when aqueous solutions were subjected to laser power density of 14 mW/mm^2. (C) Cumulative release of model dye from the PDA@mSiO$_2$ nanoparticles after different laser irradiation durations and their corresponding solution temperature (laser power density, 14 mW/mm^2). (D) Schematic representation of gardiquimod loaded PDA@mSiO$_2$ (gardi-mPDA) nanoparticles and release of cargo with NIR treatment. (E) Cancer cell viability after treatment with gardi-mPDA with and without NIR. BMDC activation indicated by cytokine secretion (F) IL-6 and (G) TNFα. Data represented as mean ± SD. ** $p<0.01$, *** $p<0.001$ and **** $p<0.0001$ by one-way ANOVA with Tukey's posttest.

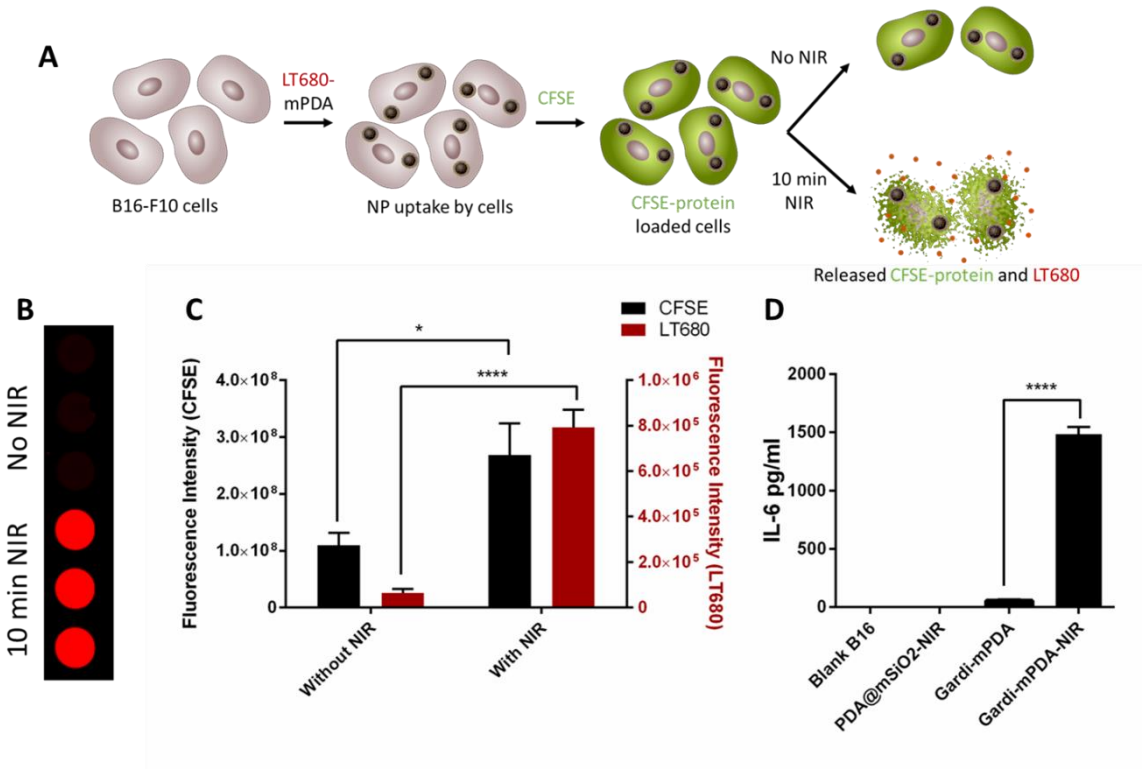

Figure 4. 4 Combined photothermal-immunotherapy effect in the presence of NIR. (A) Schematic illustration describing the experiment. Briefly, B16-F10 cells were treated with LT680-mPDA followed by labelling with CFSE. The labelled cells were divided into 2 groups and one group was given NIR treatment for 10 min. The supernatant of 2 groups were collected after 12 hours and fluorescence intensity was measured. (B) Fluorescence images (LT680) of supernatants collected from cells treatment with and without NIR, (C) Fluorescence intensity of CFSE and LT680 with and without NIR, (D) IL-6 secretion by BMDCs treated with supernatants released from B16-F10 cells. Data represented as mean ± SD. * $p<0.05$ and **** $p<0.0001$ by one-way ANOVA with Tukey's posttest.

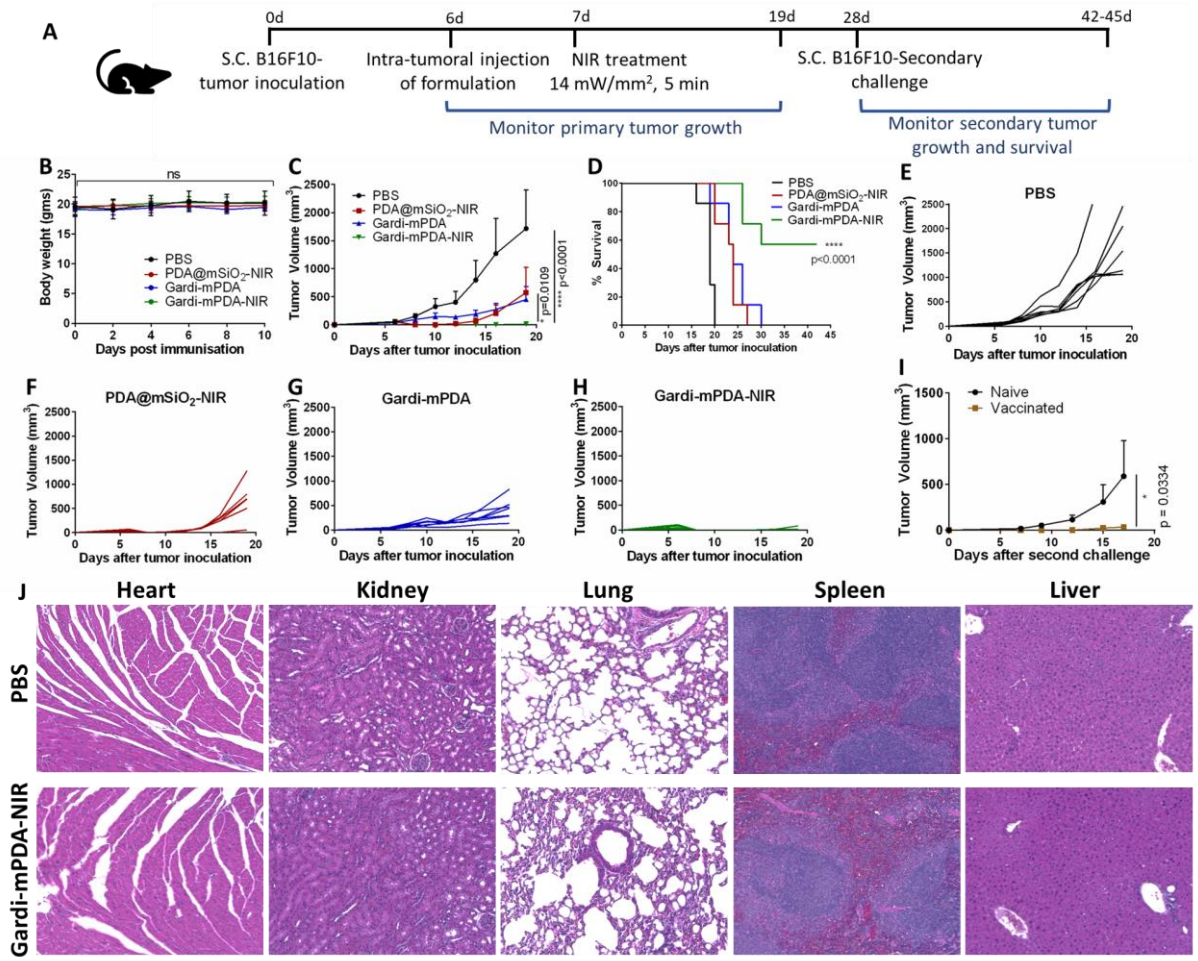

Figure 4. 5 *In vivo* photothermal-immunotherapeutic effect of gardi-mPDA.(A) Timeline of experiment. (B) *In vivo* toxicity of gardi-mPDA and NIR assessed by change in body weight of the mice, (C) tumor growth profiles, (D) survival curve of mice given different treatments (n=7). Tumor growth curves of individual mouse after treatment with (E) PBS, (F) PDA@mSiO$_2$-NIR, (G) gardi-mPDA and (H) gardi-mPDA-NIR. (I) Tumor volume after secondary challenge in mice surviving after gardi-mPDA-NIR treatment (vaccinated mice) and age matched naïve mice (n=3). (J) Hematoxylin−eosin (H&E) staining images of major mice organs after treatment with PBS and gardi-mPDA-NIR. Data represented as mean ± SD. * $p<0.05$ and **** $p<0.0001$ by one-way ANOVA with Tukey's posttest and Log-rank (Mantel-Cox) test for survival curve.

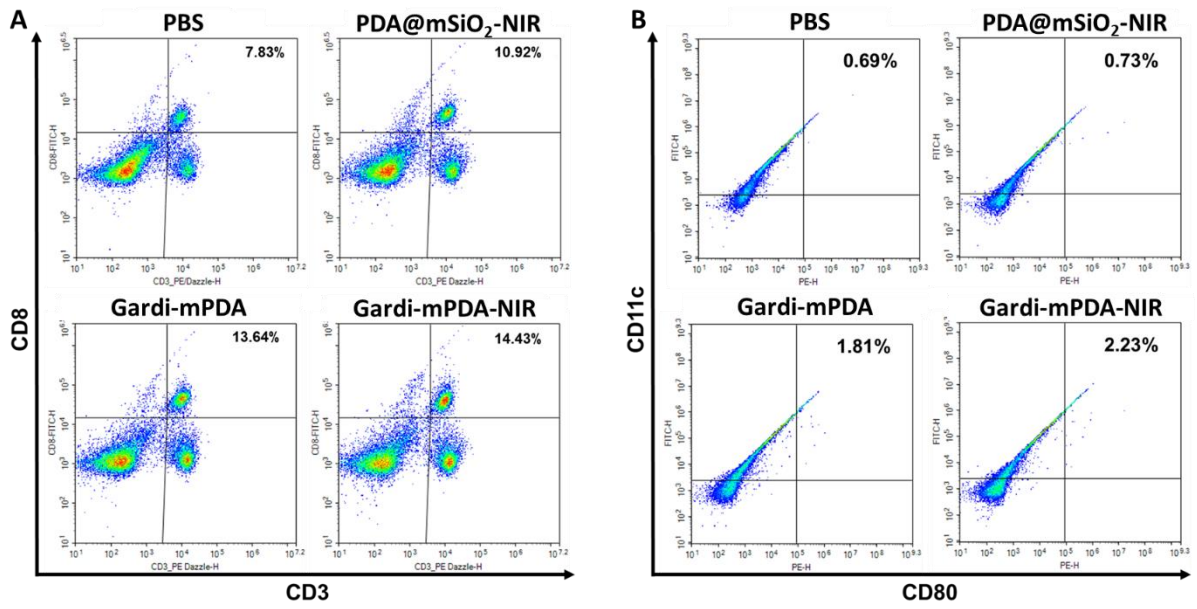

Figure 4. 6 Relative populations and activation status of immune cells in tumor draining lymph node at day 16. Representative flow cytometry plots of (A) $CD3^+$ $CD8^+$ T cells, (B) $CD11c^+$ $CD80^+$ dendritic cells. Percentage positive cells are displayed on top right corner.

Chapter 5: Reversible Photothermal Modulation of Electrical Activity of Excitable Cells using Polydopamine Nanoparticles

5.1 Introduction

Controlling a selective population of neurons to understand and establish a causal link between the neural activity and overall behavioral outcomes is a grand challenge in systems neuroscience. Harnessing the unique properties of matter at the nanoscale to tackle this grand challenge has received increased attention over the past few years.[204-208] Among the many methods that aim to modulate the biological processes, a particularly attractive method is photo-regulation, a process in which light is utilized as an external stimulus [67]. Since cells by themselves are not sensitive to photo-stimulation, insertion of light-sensitive ion channels and subsequent stimulation of these neurons for selective control (i.e. optogenetics), has become an increasingly popular and staple tool for numerous investigations.[68-69] While optogenetic techniques are promising and have revolutionized basic research aimed at understanding the computational and behavioral role of several different neural populations, there are still several limitations associated with these techniques that remain to be addressed.[70-72] These include: (i) ability to excite neurons that are embedded deep in the tissue; (ii) ability to be widely used in different model organisms with or without a rich repertoire of genetic tools; (iii) graded control of neurons; (iv) ability to control different subset of neurons in a concurrent fashion; (v) reversibility of the proposed approaches to return the controlled neurons to their original configuration; and more importantly (vi) feasibility of developing a non-invasive approach. To address some of these shortcomings, the use of nanomaterials for non-genetic electrical and thermal stimulation were explored and tested

successfully in recent years.[73] Among these, photothermal methods have shown great promise and versatility in stimulating neuronal cells [74-82].

It has been reported that the absorption of the infrared (IR) light by water, converting it to thermal energy reversibly alters the electrical capacitance[209] and therefore the excitability of nerve cells. However, direct IR stimulation is a non-specific approach that excites (or inhibits) many neurons in the area where optical illumination targets. The use of thermal energy as a stimulus to activate neurons could be highly localized to avoid generic effects on neuronal firing and their behavior. Plasmonic nanostructures such as gold nanorods (AuNRs), which serve as locoregional photothermal transducers, have been employed to modulate (inhibit/stimulate) neural activity *in vitro* using NIR light[74, 76, 81-82, 210]. Radio-frequency magnetic-field based heating of magnetic nanoparticles has also been demonstrated to be effective in thermal activation of ion channels and triggering action potentials in cultured neurons[211-212]. Magnetic nanoparticles were also used to target the motor cortex of moving mice and modulate its movement through magnetothermal stimulation[78]. Among various nanomaterials that could transform light energy to heat, polydopamine (PDA) nanoparticles are a particularly promising candidate for neuronal modulation due to their excellent photothermal properties, biocompatibility, biodegradability, and facile surface functionalization[54]. PDA-based nanomaterials have been widely investigated as photothermal agents for photothermal cancer therapy.[55-57] Furthermore, due to their biocompatibility and superior interaction with cells, PDA-based nanomaterials have been shown to be promising candidates for neuronal interfacing [58-60].

Here, we explore the use of biocompatible and biodegradable polydopamine nanoparticles and a novel highly porous biofoam as photothermal agents to stimulate excitable cells such as neurons and cardiomyocytes with NIR light in a non-disruptive manner. This novel nanomaterial

approach was utilized to localize the temperature around the excitable cells under 808 nm laser illumination. The change in the activity of neurons was monitored and quantified to understand the effect of different photothermal heating conditions. Electrical activity was measured for neurons and cardiomyocytes cultured on microelectrode array (MEA) to assess the ability of PDA nanoparticles and PDA-based foam to modulate the cell excitability. Series of quantitative analyses were performed to explain the effect of laser light intensity in the presence of PDA nanoparticles in modular and reversible control of the neuron and cardiomyocyte activity.

5.2 Results and Discussion

PDA nanoparticles are synthesized by oxidative self-polymerization of dopamine monomer in water–ethanol–ammonium mixture at room temperature, using a previously reported method [213]. Scanning electron microscopy (SEM) image and dynamic light scattering (DLS) measurement revealed the diameter of the PDA particles to be ~465 nm (Figure 5.1B and 5.1C). It has been recently reported that nanoparticle's interaction with neurons is solely dependent on its surface charge regardless of the shape, size and composition [214]. Negatively charged particles tend to adhere to the neuron cell membrane more efficiently than other particles. Polydopamine, due to the presence of hydroxyl and amine functional groups on its surface, exhibits different surface charge under different pH conditions, with an isoelectric point at 3.3 [130]. Under physiological conditions (pH=7.4), the zeta potential of PDA was measured to be -30.6 ± 0.3 mV (Figure S5.1). PDA particles exhibited broad optical absorption ranging from 400 nm to 800 nm with a peak around 500 nm (Figure 5.1D). Polydopamine nanoparticles exhibit excellent biocompatibility and biodegradability and provide high photothermal conversion efficiency and have been used as contrast agents for photothermal therapy [55]. Under 808 nm laser irradiation (power density of 14 mW mm^{-2}), PDA particle solution temperature increased with an increase

in the concentration of the nanoparticles. For a concentration of 400 µg ml^{-1}, the temperature increased by 30 ºC within 4 minutes, although the cell experiments are not conducted for this long period to prevent cell death (Figure 5.1E). It is worth noting that smaller changes in temperature (± 5 ºC) as would be desirable for controlling cell excitability can be achieved within a few seconds. The magnitude of temperature rise under NIR laser irradiation can be controlled by tuning the power density of the laser, which is critical to avoid photothermally-induced cell death (Figure 5.1F and 5.1G). Considering that the light absorption of cells and soft tissues in the NIR range is significantly lower compared to that in the visible part of the electromagnetic spectrum, 808 nm laser employed here confines the heat to the proximity of the photothermal nanoparticles, thus enabling locoregional neuromodulation [215-216].

To study the effect of nanoheating on the neuron viability, primary hippocampal neurons from prenatal rat were cultured on a substrate pre-coated with polyethylenimine (PEI) and laminin, sequentially. After 14 days *in vitro*, the neurons were immunolabeled for β-tubulin (III), which indicates good adhesion of neuron cells to the substrate and its long-term viability (Figure 5.2A) [76]. The effect of photothermal heating on the viability of cultured neurons was examined by incubating them with PDA NPs and applying NIR light (Figure 5.2B). When irradiated with 808 nm laser at a power density of 14 mW mm^{-2} in the presence of PDA NP for 1, 2 and 5 minutes, no noticable change in the viability of the neurons compared to the control groups was observed. The viability of neurons subjected to laser with and without PDA NP remained above 90%, indicating that the photothermal stimulation can be employed to modulate neuronal activity without inducing cell death.

To investigate the effect of photothermal heating on neurons activity, hippocampal neurons were cultured on microelectrode arrays (MEAs) and extracellular activity of neurons was recorded with and without PDA treatment and NIR stimulation (Figure 5.2C). Neurons cultured on MEA formed a dense network of neurites around TiN recording electrodes (Figure 5.2D). To ensure that the activity of the cultured neurons is stable and does not change over time, extracellular activity was recorded for 30 min without PDA treatment and NIR stimulation (Figure S5.2). The overlaid waveform of cultured neurons exhibited stable activity without any significant change in the spike shape or amplitude over the entire recording duration (Figure 5.2E). Before stimulating the neurons with NIR laser in presence of PDA, the effect of PDA treatment on neurons baseline activity was examined (Figure 5.2F). Upon adherence of PDA nanoparticles to the plasma membrane of neurons, the mean spike rate of the neurons increased. This is possibly because the negatively charged PDA NPs induce a depolarization of the membrane potential by providing negative charge extracellularly to cause increased firing [214].

Following the formation of a complete network and reaching a stable spontaneous activity (approximately 14 days *in vitro* (DIV)), the neurons cultured on the MEAs were treated with PDA NPs (100 µg ml^{-1} final concentration) and incubated overnight. The PDA NPs adhered to neurons and the substrate and the rest of them gradually settled down and created a bed of particles on the cells and neurites which resulted in a particle-free solution before the activity recording and photothermal stimulation. The PDA NP-treated neurons were subjected to repeated irradiation of 808 nm laser at different power densities for different stimulation duration (10, 20 and 30 seconds) in a back-to-back pulsatile fashion. The extracellular activity of the neurons was recorded before, during, and after the photothermal treatment (Figure 5.3A).

As can be noted, the neurons had spontaneous activity before any photo-stimulation. During the NIR irradiation, the number of action potentials fired reduced below spontaneous activity levels. Fewer spikes were detected for all power densities and for all durations tested (Figure 5.3A and 5.3B). The spike rate decreased monotonically with an increase in the NIR laser power density from 3 to 6 mW.mm^{-2} (Figure 5.3C). At laser power density of 3 mW mm^{-2}, there was only 39% reduction in the spike rate compared to before NIR stimulation. The spike rate reduction reached 98% when laser power density increased to 6 mW.mm^{-2}, suggesting an almost complete shutdown of neuron activity under these irradiation conditions. In comparison, neuron activity was recorded for cultures that were not treated with PDA NP but subjected to 808 nm laser irradiation (Figure S5.3). The neuron activity did not change even under a significantly higher laser power density of 14 mW mm^{-2} (Figure S5.3A). In the experiment without the presence of PDA particles, the mean spike rate measured before and during the laser irradiation did not change significantly. To investigate the effect of repeated laser stimulation, neuron activity was recorded for cultures treated with PDA NP and over 10 repeats of 30-second NIR pulses at 6 mW mm^{-2} where almost complete activity shutdown was observed (Figure 5.3D, S5.4). The similarity in neural spike activity observed, summarized as a correlation matrix, during different photothermal stimulation periods/cycles/pulses showed that the evoked photothermal responses were highly similar. Photothermal treatment had a culture wide and universal effect of in inhibiting neuron activity (Figure S5.4A). The mean spike rate for PDA NP-treated neurons was measured before the laser irradiation and after the finish of each cycle to reveal the possible permanent effect of photothermal treatment on neuron activity (Figure 5.3E). Although complete shutdown of extracellular activity was noted during the laser irradiation (with PDA NP and at 6 mW mm^{-2}), the mean spike rate after laser irradiation remained virtually identical to that

observed before irradiation, indicating the reversible nature of the photothermal neuromodulation. Moreover, the spike shape and amplitude before and after the photothermal treatment did not show significant change for the same experiment indicating that neurons recovered their activity after photothermal treatment with no sign of temporary or permanent damage (Figure S5.5).

Following the NIR irradiation period that resulted in complete inhibition of the neural activity, we noted that the neurons do not start firing immediately after stopping the irradiation but recovered their baseline activity after a short time lag. We investigated the dependence of the neural activity recovery time on the laser power density and laser irradiation duration (Figure 5.4). By fixing the irradiation duration and increasing the laser power density from 3 to 6 mW mm^{-2}, the activity recovery time (the period between the end of NIR irradiation and the first spike for each electrode) increased significantly for all of the laser durations tested (Figure 5.4A). There was a small increase in the recovery time with an increase in the laser power density from 3 to 4 mW mm^{-2}. An increase in the laser power density from 4 to 6 mW mm^{-2}, resulted in a much larger increase in the lag time (Figure 5.4C). This is possibly due to the long cooling period required at higher laser power densities, where the maximum temperature under laser irradiation is higher (Figure 5.1F). Alternately, stronger hyperpolarization during photo-stimulation period that at higher laser power densities could also result in longer recovery of resting membrane potential which could underlie similar monotonic increase in recovery time with response strength. In the case of fixed laser power density, an increase in the laser irradiation duration resulted in a monotonic increase in the activity lag time (Figure 5.4B). This increase in the activity lag time was more pronounced at the higher laser power density of 6 mW mm^{-2} (Figure 5.4D). The particles on the substrate immediately adjacent to the neurons also

contribute to the localized heating and delay the cooling process once the laser is turned off, thus causing a significant lag in the neuron activity recovery after each photothermal stimulation cycle. The tunable activity lag time with the laser power density and laser irradiation duration serves as an additional handle in light-based neuromodulation. On the other hand, specific targeting of the photothermal nanostructures to the neurons can minimize the non-specific adsorption of the nanostructures on the substrate and possibly minimize the activity lag time.

To test the generality of photothermal modulation on controlling cellular excitability, we have investigated the effect of PDA NPs and laser treatment on the electrical activity of cardiomyocytes. The iPSC-derived cardiomyocytes were differentiated and plated on the MEAs to assess the beating rates of cardiac tissues (Figure 5.5A). Without PDA NPs, upon laser stimulation, the beating rates of cardiac tissues increased only slightly (less than 10%) and recovered to baseline rate once the laser irradiation is stopped (Figure 5.5B and 5.5C). Following the incubation of cardiomyocytes with PDA nanoparticles for 24 hours, the beating rates under laser irradiation increased significantly compared to untreated cells subjected to laser irradiation (Figure 5.5D and 5.5E and supporting information Figure S5.6). These results indicate the successful modulation of the electrical activity of the cardiomyocytes with photothermal nanostructures. To further understand the effect of localized heating on the tissue, PDA NP-treated tissues were subjected to different laser power densities from 4 to 25 mW mm^{-2} (Figure 5.5F-H and supporting information Figure S5.7). With an increase in the laser power density from 4 to 14 mW mm^{-2}, the beating rate progressively increased and reached to about 1.8 times of the baseline activity (Figure 5.5F). For the highest laser power density (25 mW mm^{-2}), the cardiomyocytes exhibited irreversible changes in the beating rate, indicating possible thermal toxicity (Figure S5.7). The tissues not treated with PDA NPs exhibited only a small increase in

the beating rate with a maximum increase of less than 10% at 14 $mW.mm^{-2}$. These results demonstrate that the iPS-derived cardiac tissues showed a significant response to the localized nano-heating in the presence of PDA NPs with NIR laser irradiation. Also, the nature of the response changed from excitatory at lower laser power densities to inhibitory at laser power densities above 14 $mW\ mm^{-2}$ (Figure 5.5 and S5.7). The tunable modulation of the electrical activity of cardiomyocytes using PDA NPs could be harnessed for excitation and inhibition of cardiac activity is desired, simply by changing the laser power density.

The results discussed so far involve the incubation of the neurons (or cardiomyocytes) with colloidal PDA NP, which offers poor control over the distribution of the photothermally-active nanostructures. To achieve better spatial control over photothermal stimulation and better photothermal performance, we have designed a highly porous 3D collagen foam modified with PDA NPs as a conformal photothermal substrate (Figure 5.6A). Collagen foam is widely used in biomedical applications (e.g., wound dressing, tissue culture scaffolds) due to its highly porous structure and excellent biocompatibility.[217-218] Pristine collagen foam is white (due to light scattering) and does not possess photothermal activity (Figure S5.8A). When the collagen foam is exposed to a high concentration solution of PDA nanoparticles, within a few minutes, the collagen fibers are completely covered with PDA nanoparticles, as is indicated by its change of color from white to black (Figure S5.8B). SEM images of the PDA-modified collagen foam (PDA/Collagen) reveal the high porosity and the PDA nanoparticles adsorbed on individual collagen fibers (Figure 5.6B). The PDA/collagen foam was found to be highly stable with no noticeable desorption of the PDA NP even under mechanical agitation. The absorbance spectrum of the PDA/collagen foam is similar to that of PDA NP solution suggesting that photothermal efficiency for the foam should be similar to the PDA NPs (Figure 5.6C). In its dry state, the

surface temperature of PDA/collagen foam increased by more than 100 ºC in just less than 10 seconds when irradiated by laser at a power density of 6 mW mm^{-2} (Figure S5.9). Even at a much lower laser power density of 3 $mW.mm^{-2}$, we noted a 60 ºC increase in the local surface temperature within the first 10 seconds. In wet state, the foam surface temperature rose by up to 12 ºC after 10 seconds and by up to 20 ºC after 30 seconds of irradiation at a laser power density of 6 mW mm^{-2} (Figure 5.6D). The superior photothermal activity of the PDA/collagen foam compared to the high concentration of PDA NPs (100 µg ml^{-1}) stems from the highly dense adsorption of the PDA NPs on the collagen fibers and efficient light trapping within the foam due multiple reflections. In addition to the excellent photothermal properties, the highly porous PDA/collagen foam soaked in the cell culture medium can be applied as a conformal patch on cells and tissues.

To investigate the efficacy of PDA/collagen foam in photothermally modulating the neural activity, the foam was placed on the neurons cultured on the MEAs for 14 DIV, and after the neurons reached stable spontaneous activity. The neurons with PDA/collagen foam were subjected to repeated irradiation of 808 nm laser at different power densities for different stimulation durations (10, 20 and 30 seconds). The extracellular activity of the neurons was recorded during the photothermal treatment and it is evident that spiking activity during the photothermal stimulation is reduced drastically (Figure 5.6E and 5.6F). The quantitative measurement of the changes in the spike rate showed that at all the power densities tested, the neuron activity suppression was above 90% (Figure 5.6G). In comparison, at the same power density of 3 mW mm^{-2}, photothermal treatment of neurons treated with colloidal PDA NP resulted in only a 39% reduction in neuron activity. Moreover, when the power density was increased to 15 $mW.mm^{-2}$, PDA/collagen foam resulted in permanent damage to cells, and the

activity suppression was not reversible. This superior photothermal performance of the PDA/collagen compared to colloidal PDA NP allows the utilization of lower power light sources (e.g. near-infrared LEDs) instead of laser for modulating the neural activity. Furthermore, this PDA/collagen 3D foam could be easily applied as a patch on brain tissues and cardiac tissues for modulating the electrical activity in a facile manner.

5.3 Conclusion

In conclusion, we have demonstrated the reversible and graded control of the electrical activity of excitable cells using PDA nanoparticles as biocompatible and biodegradable photothermal transducers. In the presence of PDA nanoparticles, the spike rate of neurons was significantly suppressed under NIR laser irradiation with a power density as low as 3 mW mm^{-2}. With a progressive increase in the laser power density, we observed a monotonic decrease in the spike rate. The activity recovery time was found to be dependent on irradiation power density and irradiation duration. The neural activity suppression and recovery were repeatable over 10 consecutive pulses of laser irradiation in a single trial, demonstrating the robustness of this non-invasive neuromodulation approach. In the presence of PDA nanoparticles, the beating rate of cardiomyocyte tissues progressively increased as the irradiation laser power density increased from 4 to 14 mW mm^{-2}. To improve the ease of interfacing the photothermal agents with neural cultures and brain tissues, we have designed and realized a 3D collagen/polydopamine nanoparticle foam and applied it on the cultured neurons as an “add-on” patch. The 3D foam demonstrated superior photothermal and neuromodulation performance compared to colloidal polydopamine nanoparticles in that we observed more than 90 percent reduction in neuron

activity even at laser power densities as low as 3 mW mm^{-2}. Compared to inorganic photothermal nanostructures (e.g., noble metal nanoparticles), PDA nanostructures are better suited for *in vivo* neuromodulation owing to their high biocompatibility and biodegradability. We believe that this novel material platform for non-invasive neuromodulation can be easily extended to other excitable cells both *ex vivo* and *in vivo* and serve as a valuable tool in nano-neuroengineering.

5.4 Experimental Section

***Cell Culture**:* All procedures have been approved by the Institutional Animal Care and Use Committee (IACUC) at Washington University in St. Louis. Hippocampal tissues were dissected from embryonic day 18 Sprague_Dawley rat brain (Charles River, USA). The tissues were transferred into Hibernate EB medium (HEB, BrainBits, USA) for further use. Cell dissociation solution was prepared by dissolving 6 mg papain (P4762, Sigma, USA) in 3 ml of Hibernate E-Ca (HE-Ca, BrainBits, USA). Hippocampal tissues were transferred to the cell dissociation solution and incubated at 30 ºC for 10 minutes. Dissociation solution was removed and HEB medium was added to the tissues, followed by trituration with fire-polished Pasteur pipette. Cell dispersion was centrifuged (200×g, 1 minute) and supernatant was removed, and pellets were resuspended in NbActiv4 (BrainBits, USA). Substrates were pre-treated with poly(ethyleneimine) solution (0.1 % in water, P3143, Sigma, USA) for 30 minutes followed by air drying. Before the cell seeding, substrates were treated with laminin solution (20 µg ml^{-1} in NbActiv4 medium, L2020, Sigma, USA). After removing the extra laminin solution, cells were seeded at the density of 500-1000 cells.mm^{-2} and maintained in the NbActiv4 medium in a humidified incubator with 5% CO_2 and 37 ºC condition. After 2 days, half of the medium was changed with fresh NbActiv4 medium and was regularly changed every 4 days.

For iPS-derived cardiomyocytes (iPS-CMs), the WTC-11-GCaMP6 from Bruce Conklin Lab in Gladstone Institute were used as the induced pluripotent stem cells (iPSC). The iPSCs were maintained in E8 medium (Thermo Fisher Scientific) on Matrigel-coated (Corning) tissue culture plate and passaged every four days. The protocols used to differentiate and purify iPS-derived cardiomyocytes (iPS-CMs) was through Wnt modulation and lactate purification that was previously described [219-220].

Polydopamine Nanoparticle and Collagen/Polydopamine Foam Preparation*:* All chemicals were purchased from Millipore Sigma, St. Louis, USA and used without further modification. Polydopamine particles were synthesized by using a method described elsewhere.[213] In a typical synthesis procedure of polydopamine nanoparticles, 252 mL of deionized (DI) water (resistivity >18.2 MΩ·cm) was mixed with 112 mL of ethanol in a 1000 mL glass container. Subsequently, 1.96 mL of aqueous solution of ammonia (28−30% NH4OH) was introduced into the above water/ethanol mixture. After stirring for 30 min, the aqueous solution of dopamine hydrochloride (1.4 g in 28 mL) was added to the above solution. The reaction was left under gentle magnetic stirring for 24 h with no cap on the glass container. The PDA particles were collected by centrifugation (9000 rpm, 10 min) and washed with DI water three times and dispersed in water (320 mL).

To prepare the photothermally active 3D foam, a collagen film (HeliTAPE Collagen Wound Dressing, Miltex® Instruments, USA) was soaked in water to create a hydrogel. The collagen hydrogel wass then freeze-dried to achieve a highly porous 3D foam. The collagen foam, was soaked in the PDA NP solution (1 mg ml^{-1} in water) and left for 5 minutes with shaking followed by washing with water to remove the excess nanoparticles. The PDA NP-loaded collagen foam was freeze-dried again to be used in the photothermal stimulation experiments.

Material Characterization: Scanning electron microscopy (SEM) images were obtained by using a JEOL JSM-7001 LVF Field Emission scanning electron microscope. Dynamic light scattering (DLS) and zeta potential measurements were performed using Malvern Zetasizer (Nano ZS). Shimadzu UV-1800 spectrophotometer was employed for light absorption measurements.

Photothermal Stimulation*:* A fiber optic NIR laser (808 nm) was used for a light source and the laser beam spot size and power density was controlled by its distance from the microelectrode array (MEA, Multichannel Systems, Germany). Hippocampal neuronal networks were cultured on a MEA chip and incubated with PDA NPs overnight. The PDA NP-treated neurons were then repeatedly irradiated with a NIR laser (808 nm) at different power densities and durations. A typical photothermal experiment lasts for 330 seconds, and the cells were illuminated with laser at different power densities for 10, 20 and 30 seconds. The laser on and off was controlled by a mechanical shutter. For repeatability experiment, cells were illuminated for 30 seconds with a power density of 6 mW mm^{-2} followed by 90 seconds of no laser illumination for 10 cycles. The experiment for calculating the neuron activity recovery time after laser illumination was performed by recording the activity for 60 seconds followed by laser pulses with different durations and power densities followed by at least 90 seconds wait time, for a total of 210 seconds. Same experimental procedures were followed for cardiomyocytes.

Electrical Activity Recording*:* Neural recordings were obtained from neuronal cultures at the age of 14-18 DIV. Extracellular activity from cultured neurons were monitored using 60-channel TiN microelectrode arrays (MultiChannel Systems, diameter 30 μm, electrode spacing 200 μm, 500 nm thickness of Si3N4 insulator). Electrode signals were amplified and digitized with an *in vitro* MEA system (Multichannel systems, gain 1100, bandwidth 10-8 kHz, sampling frequency 25 kHz). The recorded signals were filtered with a 200 Hz digital high pass filter (Butterworth,

second order), and spikes were detected by setting the threshold level at five times the standard deviation of background noise using vendor provided software (MC Rack, MultiChannel Systems). Recording condition was maintained at 37 ºC and 5% CO_2. Collected data were processed using MATLAB (MathWorks). For bulk heating experiments, the head stage temperature was adjusted to desired value and after 15 minutes of stabilization, the neuron activity recording was performed. To test the effect of PDA NP on neuron activity without laser stimulation, the extracellular activity of cultured neurons was recorded for 30 minutes before addition of PDA NP after which the culture was incubated with PDA NP solution (100 µg ml^{-1} final concentration).

To record the field potential activities of iPS-CM, the iPS-CMs were suspended at 30×10^6 cells ml^{-1} and a 4 µl droplet was seeded on the recording area of MEA probe (60MEA200/10iR-Ti). The field potentials were recorded using MC_Rack software (Multichannel Systems) at 10000 Hz sampling rate with a 200 Hz digital high pass filter (Butterworth, second order). The data were converted to ABF format using MC_Data Tool (Multichannel Systems) and the field potentials were analyzed using Clampfit 10.7 (Molecular Devices) and MATLAB (MathWorks).

Cell Viability: Hippocampal neurons were cultured in pre-treated 96 well black plates at the density of 20000 cells per well for 14 DIV and treated with PDA NPs at 100 µg ml^{-1} final concentration. After 5 h incubation, they were subjected to 808 nm laser for 10 minutes at a power density of 14 mW mm^{-2}. After 24 hours, MTS assay was performed as per manufacturer protocol.

Data Analysis*:* Recording channels whose average firing rate was larger than 0.1 spikes per second were selected as active channels and used for neural activity analysis. For the analysis of spontaneous activity, peri-event time histogram and raster plots were used with the NIR

irradiation as an event. The spike rate reduction (ΔR/R) with or without the NIR irradiation was calculated by the following equation: ΔR/R (%) = [R(ON) - R(OFF)]/ R(OFF), where R(OFF) and R(ON) indicated the average spike rate before and after the onset of NIR irradiation, respectively. R(ON) covered the entire irradiation period (5-45 seconds), and R(OFF) covered the 30 second window just before the onset of the irradiation. All statistics were performed with 5% significance level.

Immunostaining*:* Hippocampal neurons were fixed in 4% neutral buffered formalin in 1x PBS for 30 minutes at room temperature and washed with PBS three times. To permeabilize the cells, neurons were incubated with 0.5% Triton X-100 in 1x PBS for 10 minutes at room temperature and washed with PBS three times. The nonspecific binding of antibodies was blocked by 6% bovine serum albumin (BSA, Sigma) in PBS for 30 minutes, and washed with PBS once. The biotinylated primary antibody (neuron-specific β-III tubulin antibody, 6 μg ml^{-1} in 1.5% BSA, R&D systems MAB 1195) was added to the cells and incubated for 3 h at RT. After washing with PBS for three times, streptavidin-tagged fluorescent dye (IRDye 800CW Streptavidin, 50 ng ml^{-1} in 1.5% BSA, LI-COR) were incubated with the cells for 30 minutes at RT. After washing with PBS for three times, DAPI solution (300 nM in PBS, Sigma) was used for nucleus staining. Fluorescence images were obtained using Lionheart FX Automated Microscope (BioTek, USA). The iPSC-derived cardiomyocytes were seeded on glass slide at Day 30. The cells were fixed with 4% (v/v) paraformaldehyde for one hour and stained with primary antibody TNNT2 (ab45923; Abcam) and secondary antibody Alexa Fluor 488 goat anti-rabbit IgG (A11008; Invitrogen) and nuclei counterstained by DAPI solution (1 μg mL^{-1}).

5.5 Supporting Information

Supporting Information for chapter 5 is provided in appendix 4.

5.6 Figures

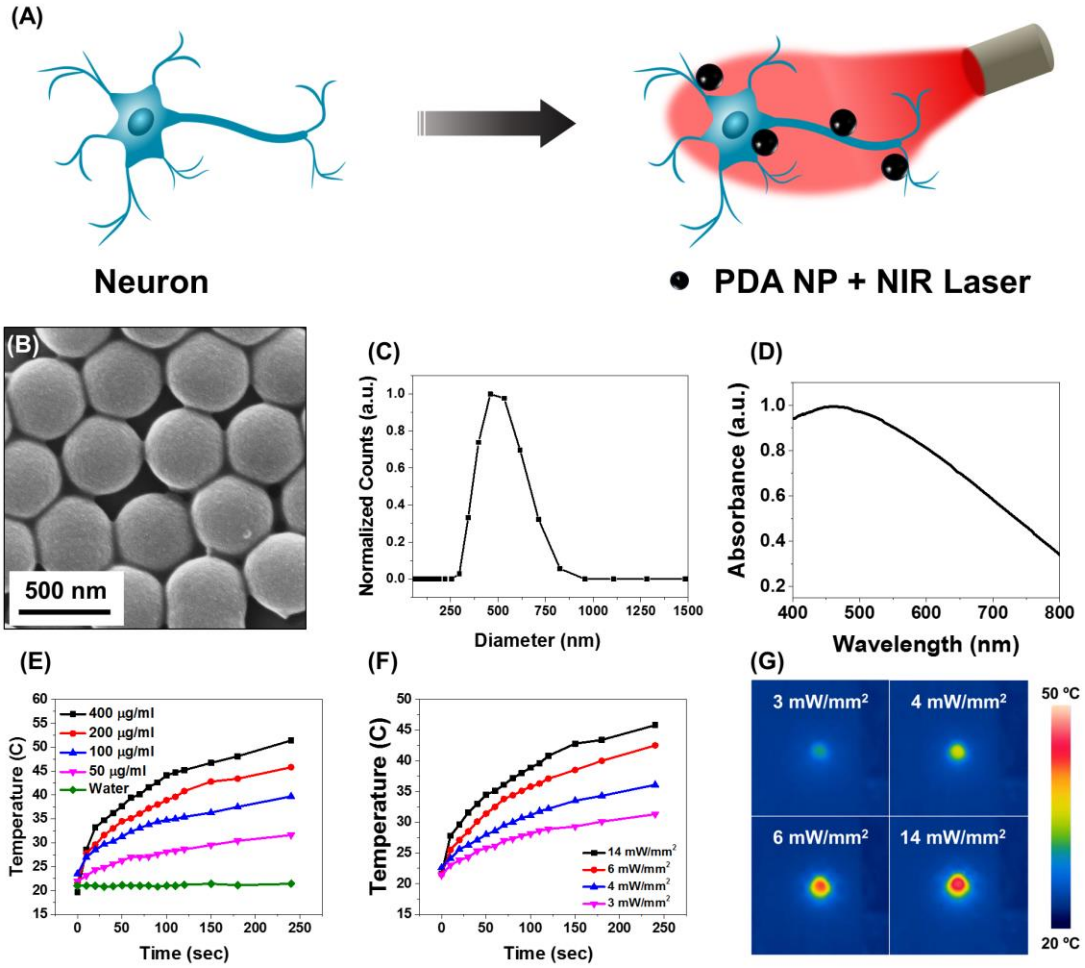

Figure 5. 1 (A) Schematic of Polydopamine nanoparticle (PDA NP)-mediated photothermal stimulation of neurons. PDA nanoparticles localized on the neuron membrane, modulates the neural activity through photothermal conversion of NIR light. (B) SEM image, (C) DLS measurement and (D) Absorption spectra of PDA NPs. (E) Temperature changes in PDA NP solution with different concentrations at 14 mW mm^{-2} laser power density. (F) Temperature changes in 200 µg ml^{-1} solution of PDA NP at different laser power density and (G) Corresponding IR Camera images of the PDA NP solution at the end of the laser illumination period.

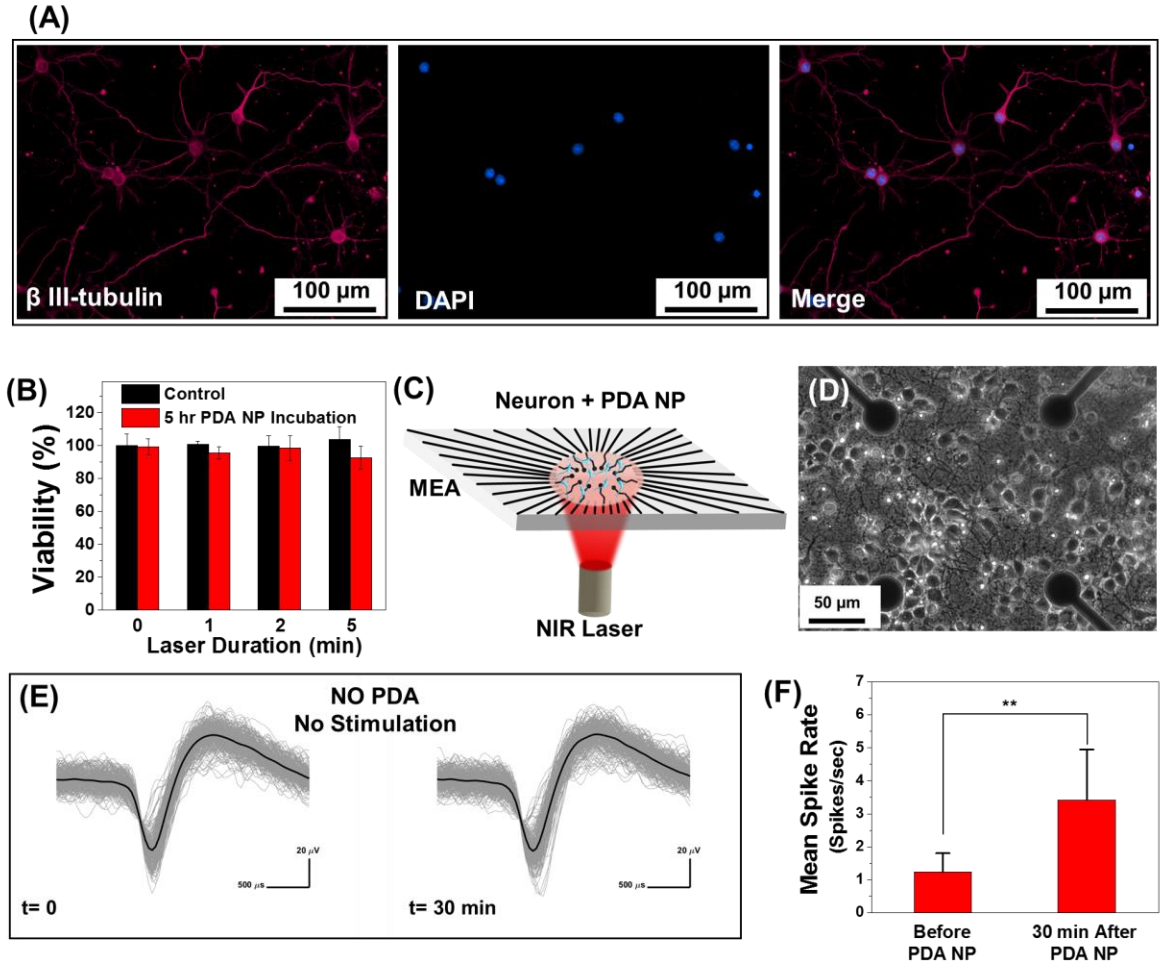

Figure 5. 2 (A) Fluorescence images of cultured hippocampal neurons after immunochemical staining with β-tubulin (III) (magenta) and nucleus (blue). (B) Cell viability of neurons subjected to 1, 2 and 5 minutes of NIR irradiation (14 mW mm^{-2}) without PDA NP (control) and with PDA NP (100 µg ml^{-1} final concentration). The heat generated by NIR laser in presence of PDA NP did not change the viability of the neurons compared to control sample (no PDA NP), meaning that it is safe to use PDA NP for photothermal treatment of neurons. (C) Schematic of the experimental setup with neurons cultured on a microelectrode array (MEA) and stimulated with NIR laser with and without PDA NP treatment. (D) Phase contrast image of the hippocampal neurons cultured on PEI-laminin coated MEA with cell density of 1000 cells mm^{-2}. (E) Overlaid waveform of hippocampal neurons at half an hour time interval. Neurons were not treated with PDA NP and are not subject to any external stimulation. Spikes from 3-minute recording with 256 spikes in each set (no change in mean spike rate). Black curve shows the mean value for each set. (F) Effect of localization of PDA NP on neuron membrane on the mean spike rate of cultured neurons without NIR stimulation. Unpaired Two-samples t-test; p= 0.0018, n=56, * $p<0.05$, ** $p<0.01$, *** $p<0.001$ and **** $p<0.0001$.

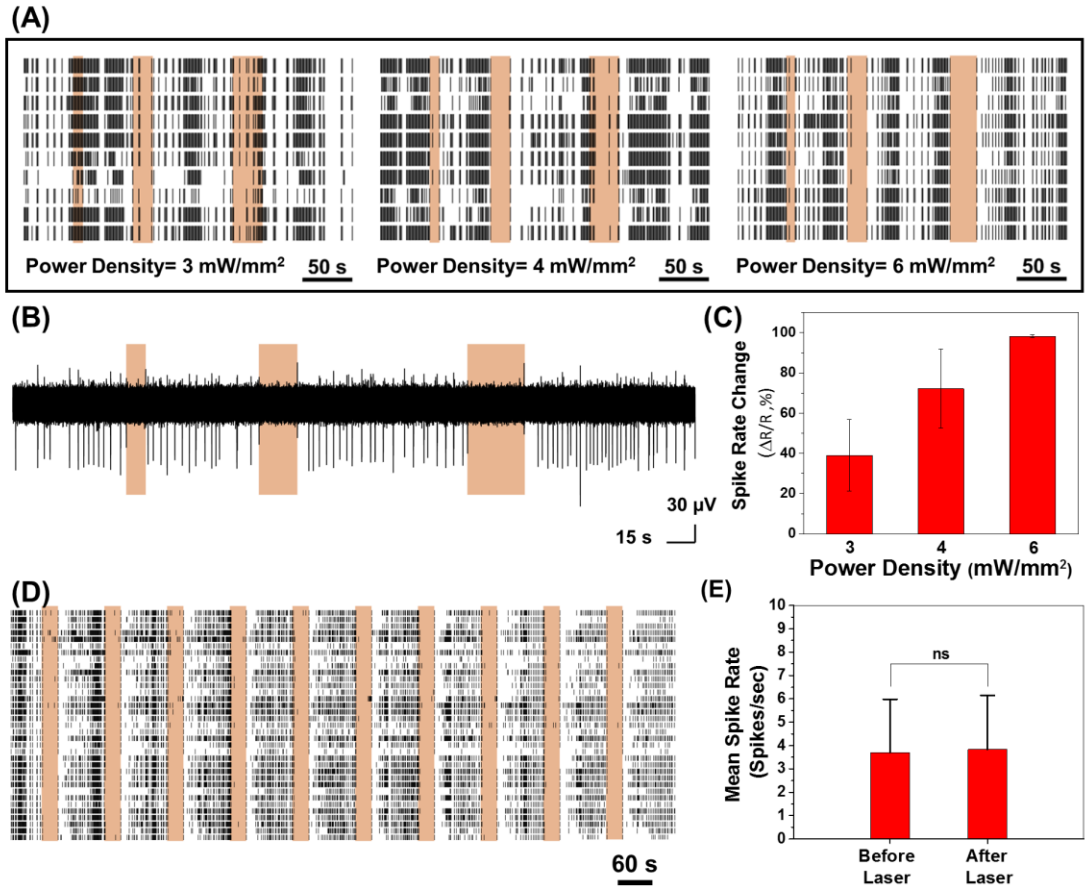

Figure 5. 3 (A) Spike rates of neurons treated with PDA NP (100 µg ml^{-1}) with NIR irradiation at different power densities. (B) A single trace of spike recording for different NIR irradiation periods (10 s, 20 s and 30 s laser irradiation at power density of 6 mW mm^{-2}). (C) Quantification of spike rate changes in panel A (effect of laser power density on spike rate change and inhibition of neuron activity). (D) Spike rates of neurons treated with PDA NP (100 µg ml^{-1}) with NIR irradiation (power density of 6 mW mm^{-2}) over 10 cycles of 30 s treatment. (E) Mean spike rates of PDA NP-treated neurons before and after NIR irradiation (Data were collected for laser power density of 6 mW mm^{-2} where neuron activities were completely suppressed during NIR irradiation, Unpaired Two-samples t-test; p= 0.8866, n=55).

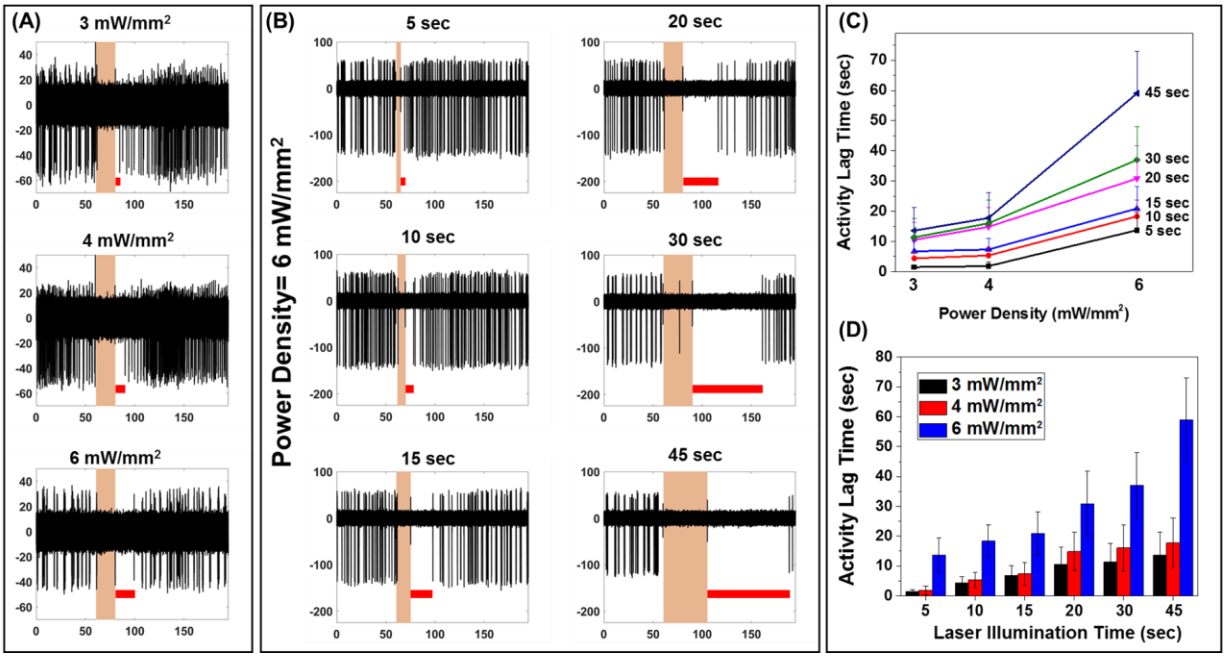

Figure 5. 4 (A) A single trace of spike recording for neuron treated with PDA NP at different laser power densities for 20 s. Red lines show the activity lag time which is the amount of time it took after the laser illumination for the first spike to appear. (B) Effect of laser duration on the activity lag time for PDA NP treated neurons (power density of 6 mW mm^{-2}). (C) Quantification of the effect of the laser duration on the activity lag time at different laser power densities. (D) Quantification of the effect of the laser power density on the activity lag time at different laser duration times.

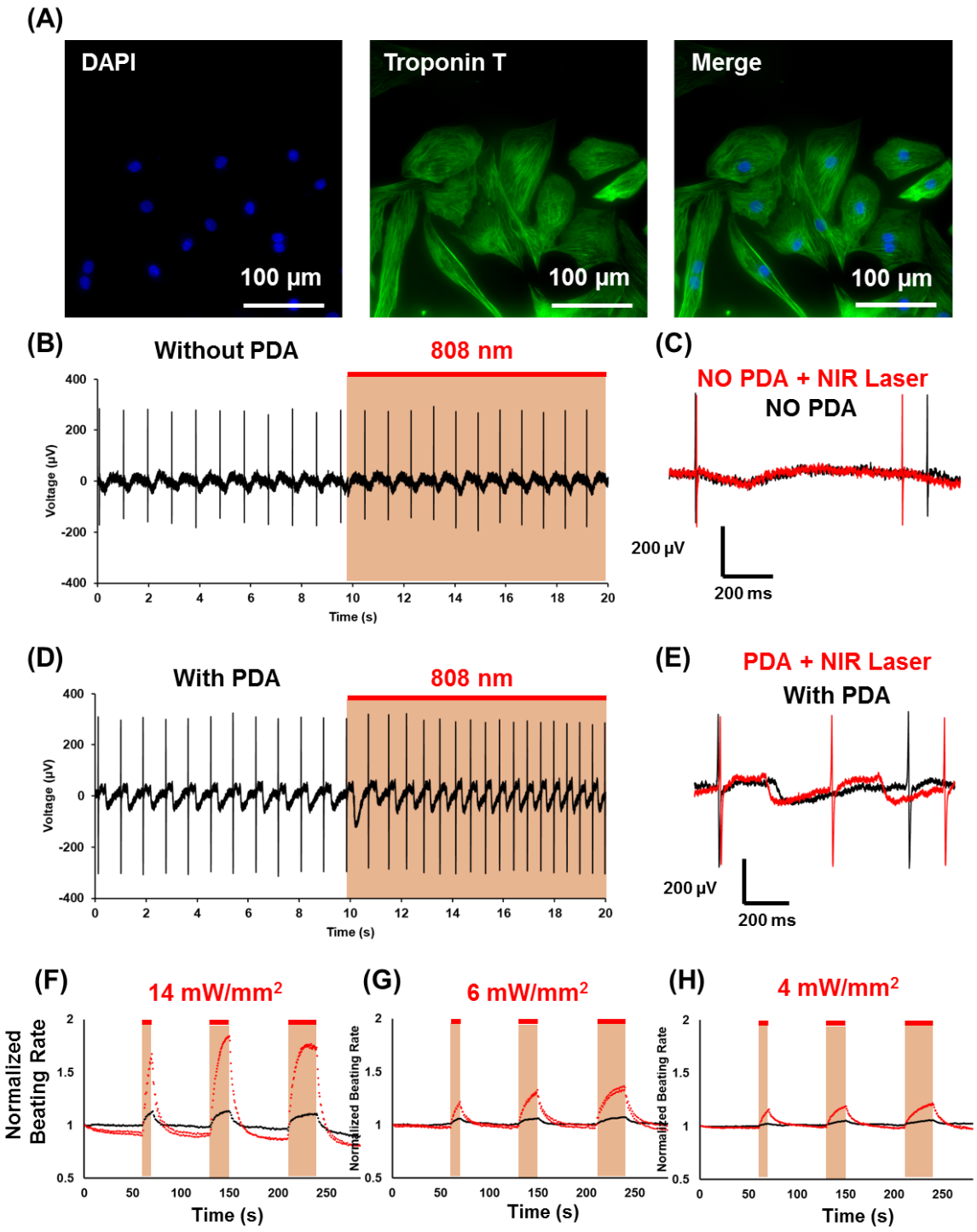

Figure 5. 5 (A) The immunofluorescence images of iPSC-derived cardiomyocyte counter stained with DAPI (blue) and cardiac troponin T (green). PDA nano-particles increased the beating rates of iPS-derived cardiomyocytes. (B) The original trace of filed potential recording of iPS-derived cardiomyocytes from MEA system without PDA treatment. The laser power density was 14 $mW.mm^{-2}$ and was turned on for 10 seconds as indicated. (C) The representative traces of field

potential recordings of iPS-CMs without treating with PDA nanoparticles before (black) and after (red) 808 nm laser excitation. (D) The original trace of filed potential recording of iPS-derived cardiomyocytes from MEA system. The iPS-CMs were treated with PDA nanoparticles for 24 hrs and washed out before recording. The laser power density was 14 mW mm^{-2} and was turned on for 10 seconds as indicated. (E) The representative traces of field potential recordings of iPS-CMs treated with PDA nanoparticles before (black) and after (red) 808 nm laser excitation. (F) – (H) The normalized beating rates of iPS-CMs before and after 808 nm laser excitation. At different laser power densities (14, 6 and 4 mW mm^{-2}), the laser was turned on for 10, 20 and 30 seconds at the indicated time. The beating rates were determined by calculating the peak intervals of field potential recordings and normalized the rates at baseline.

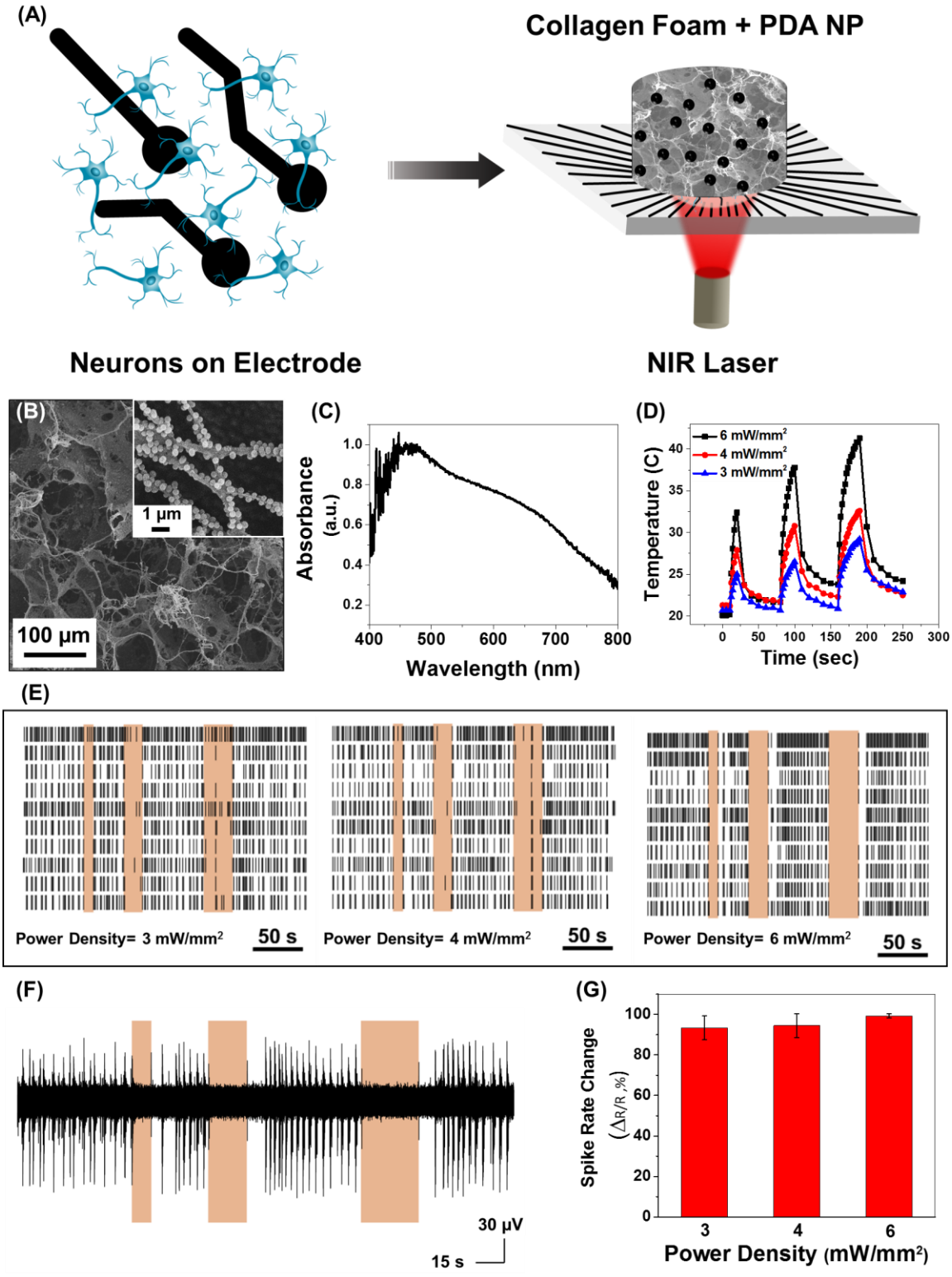

Figure 5. 6 (A) Schematic of experimental setup with neurons cultured on a microelectrode array (MEA), Collagen foam + PDA NP placed on the culture and stimulated with NIR laser. (B) SEM image (inset: higher magnification SEM) and (C) Absorption spectra of collagen foam + PDA

NP. (D) Temperature changes of collagen foam + PDA NP in wet state at different laser power densities. (E) Spike rates of neurons with collagen foam + PDA NP and NIR irradiation at different power densities. (F) A single trace of spike recording for different NIR irradiation periods (10 s, 20 s and 30 s laser irradiation at power density of 6 mW mm^{-2}). (G) Quantification of spike rate changes in panel E (effect of laser power density on spike rate change and inhibition of neuron activity).

Chapter 6: Conclusions

6.1 General Conclusions

Polydopamine-based organic nanomaterials possess excellent physical, chemical and optical properties which make them promising candidates for environmental and biomedical applications. They are rich with chemical groups on their surface that makes it easy to functionalize them with many desirable chemistries and tune them for specific applications. Polydopamine polymerization is a facile process which could be applied to almost any surface to create favorable chemistry on surfaces that are normally hard to functionalize. The synthesis of polydopamine nanoparticle is easy process and allows for creation of particles with different shapes and sizes to be used in different applications. Polydopamine surface chemistry demonstrates affinity to heavy metal ions and organic dyes, which make it excellent tool for fabrication of multifunctional membranes and substrates for environmental applications. Also, the excellent light-to-heat conversion efficiency of polydopamine nanomaterials enables it to serve as biocompatible photothermally active nanomaterial for various biomedical applications. This dissertation demonstrated several applications of polydopamine nanomaterials in environmental and biomedical applications.

We have demonstrated a novel PDA/BNC composite adsorption membrane which has potential to treat wastewater containing multiple inorganic and organic pollutants. The PDA/BNC membrane is fabricated by incorporating high density PDA particles inside BNC matrix during its growth. This fabrication technique is highly versatile and can be easily adapted to incorporate other adsorbents. All the materials used in the membrane fabrication process are biocompatible and biodegradable. The unique fabrication process resulted in a highly uniform distribution of PDA particles within the BNC matrix. The PDA/BNC membrane showed effective contaminant

removal from feed water containing heavy metal ions and positively charged organic dyes at high concentrations in a single pollutant or pollutant cocktail situations. The facile, inexpensive, and scalable synthesis, excellent mechanical robustness and highly efficient removal of heavy metals and organic dyes under complex conditions and the ability to modify the PDA surface for variety of water treatment systems, collectively make PDA/BNC membrane demonstrated here a promising and powerful candidate for wastewater treatment.

We have designed and demonstrated a highly efficient organic dye removal catalytic membrane based on BNC loaded with mPDA and Pd nanoparticles for wastewater treatment. Key factors which enable the Pd-mPDA-BNC membrane to be effective in dye removal are: synergistic effect of dye adsorption on mPDA and catalytic ability of Pd nanoparticles in presence of $NaBH_4$; highly porous structure due to the addition of mPDA nanoparticles, which increases the specific surface area for higher adsorption and degradation; and uniform and high loading of Pd nanoparticles within the entire membrane. The membrane fabrication process is simple and is easily scalable. The Pd-mPDA-BNC membrane exhibited excellent dye removal performance as well as the ability for the treatment of multiple contaminants with different chemical structures and charges simultaneously. The membrane exhibited significantly higher water flux compared to commercially available membranes even under low vacuum pressure. The facile and the scalable fabrication of the membrane along with excellent dye removal efficiency and higher water flux makes it a highly attractive candidate for wastewater treatment even at industrial scales.

We have also shown the design and synthesis technique of a core-shell nanostructure based on highly biocompatible and completely biodegradable components, where the photothermal property of the core was integrated with NIR-responsive drug release properties of the shell for

ultimately generating a robust and long-lasting anti-tumor immune response. PDA nanoparticles were employed as a photothermal core and mesoporous silica shell was used as the carrier for a mixture of phase-change material (1-tetradecanol) and immune-stimulating agent (gardiquimod). These nanoparticles were effectively uptaken by cancer cells and led to concurrent release of both antigens from the cancer cells (through immunogenic cell death) and adjuvant from the nanoparticles upon NIR irradiation. The external trigger NIR facilitated spatiotemporal control of the therapeutic events for ultimately mounting a potent anti-tumor immune response. The core-shell nanoparticle design is universal and is amenable for loading other types of immunomodulatory or chemotherapeutic drugs or their combinations for synergistic effects. The versatility and unique design of these multifunctional nanoparticles can be harnessed for improved photothermal-immunotherapeutic treatments acting as a powerful platform for cancer treatment.

Furthermore, we have demonstrated the reversible and graded control of the electrical activity of excitable cells using PDA nanoparticles as biocompatible and biodegradable photothermal transducers. In the presence of PDA nanoparticles, the spike rate of neurons is significantly suppressed under NIR laser irradiation with a power density as low as 3 mW mm^{-2}. With a progressive increase in the laser power density, we observed a monotonic decrease in the spike rate. The activity recovery time was found to be dependent on irradiation power density and irradiation duration. In the presence of PDA nanoparticles, the beating rate of cardiomyocyte tissues progressively increased as the irradiation laser power density increased from 4 to 14 mW mm^{-2}. To improve the ease of interfacing the photothermal agents with neural cultures and brain tissues, we have designed and realized a 3D collagen/polydopamine nanoparticle foam and applied it on the cultured neurons as an “add-on” patch. The 3D foam demonstrated superior

photothermal and neuromodulation performance compared to colloidal polydopamine nanoparticles. Compared to inorganic photothermal nanostructures (e.g., noble metal nanoparticles), PDA nanostructures are better suited for *in vivo* neuromodulation owing to their high biocompatibility and biodegradability. We believe that this novel nanomaterial platform for non-invasive neuromodulation can be easily extended to other excitable cells both *ex vivo* and *in vivo* and serve as a valuable tool in neuro-engineering.

6.2 Significance and Outlook

In addition to the representative nanomaterials and applications demonstrated in this dissertation, the fabrication strategies and design principles demonstrated in this work can have far reaching implications to realize various nanocomposites with applications in water purification, energy harvesting, cancer treatment and neuroscience. By harnessing polydopamine-based biocompatible and biodegradable organic materials, a wide variety of functional materials and nanocomposites can be achieved in a facile and controllable way.

References

1. Liu, Y.; Ai, K.; Lu, L., Polydopamine and Its Derivative Materials: Synthesis and Promising Applications in Energy, Environmental, and Biomedical Fields. *Chemical Reviews* **2014,** *114* (9), 5057-5115.
2. Szefer, P.; Frelek, K.; Szefer, K.; Lee, C. B.; Kim, B. S.; Warzocha, J.; Zdrojewska, I.; Ciesielski, T., Distribution and relationships of trace metals in soft tissue, byssus and shells of Mytilus edulis trossulus from the southern Baltic. *Environmental Pollution* **2002,** *120* (2), 423-444.
3. Lee, H.; Dellatore, S. M.; Miller, W. M.; Messersmith, P. B., Mussel-inspired surface chemistry for multifunctional coatings. *Science (New York, N.Y.)* **2007,** *318* (5849), 426-430.
4. Lee, H.; Lee, B. P.; Messersmith, P. B., A reversible wet/dry adhesive inspired by mussels and geckos. *Nature* **2007,** *448*, 338.
5. Xu, L. Q.; Yang, W. J.; Neoh, K.-G.; Kang, E.-T.; Fu, G. D., Dopamine-induced reduction and functionalization of graphene oxide nanosheets. *Macromolecules* **2010,** *43* (20), 8336-8339.
6. Postma, A.; Yan, Y.; Wang, Y.; Zelikin, A. N.; Tjipto, E.; Caruso, F., Self-polymerization of dopamine as a versatile and robust technique to prepare polymer capsules. *Chemistry of Materials* **2009,** *21* (14), 3042-3044.
7. Lee, H.; Rho, J.; Messersmith, P. B., Facile Conjugation of Biomolecules onto Surfaces via Mussel Adhesive Protein Inspired Coatings. *Advanced Materials* **2009,** *21* (4), 431-434.
8. Ryu, J.; Ku, S. H.; Lee, H.; Park, C. B., Mussel-Inspired Polydopamine Coating as a Universal Route to Hydroxyapatite Crystallization. *Advanced Functional Materials* **2010,** *20* (13), 2132-2139.
9. Liu, R.; Mahurin, S. M.; Li, C.; Unocic, R. R.; Idrobo, J. C.; Gao, H.; Pennycook, S. J.; Dai, S., Dopamine as a Carbon Source: The Controlled Synthesis of Hollow Carbon Spheres and Yolk-Structured Carbon Nanocomposites. *Angewandte Chemie International Edition* **2011,** *50* (30), 6799-6802.
10. Ai, K.; Liu, Y.; Ruan, C.; Lu, L.; Lu, G., Sp2 C-Dominant N-Doped Carbon Sub-micrometer Spheres with a Tunable Size: A Versatile Platform for Highly Efficient Oxygen-Reduction Catalysts. *Advanced Materials* **2013,** *25* (7), 998-1003.
11. Han, X.; Zhang, L.; Li, C., Preparation of polydopamine-functionalized graphene-Fe3O4 magnetic composites with high adsorption capacities. *RSC Advances* **2014,** *4* (58), 30536-30541.
12. Lee, M.; Rho, J.; Lee, D. E.; Hong, S.; Choi, S. J.; Messersmith, P. B.; Lee, H., Water Detoxification by a Substrate-Bound Catecholamine Adsorbent. *ChemPlusChem* **2012,** *77* (11), 987-990.
13. Dong, Z.; Zhang, F.; Wang, D.; Liu, X.; Jin, J., Polydopamine-mediated surface-functionalization of graphene oxide for heavy metal ions removal. *Journal of Solid State Chemistry* **2015,** *224*, 88-93.
14. Nematollahzadeh, A.; Seraj, S.; Mirzayi, B., Catecholamine coated maghemite nanoparticles for the environmental remediation: Hexavalent chromium ions removal. *Chemical Engineering Journal* **2015,** *277*, 21-29.

15. Sun, D. T.; Peng, L.; Reeder, W. S.; Moosavi, S. M.; Tiana, D.; Britt, D. K.; Oveisi, E.; Queen, W. L., Rapid, Selective Heavy Metal Removal from Water by a Metal–Organic Framework/Polydopamine Composite. *ACS Central Science* **2018**.
16. Gao, H.; Sun, Y.; Zhou, J.; Xu, R.; Duan, H., Mussel-Inspired Synthesis of Polydopamine-Functionalized Graphene Hydrogel as Reusable Adsorbents for Water Purification. *ACS Applied Materials & Interfaces* **2013,** *5* (2), 425-432.
17. Schwarzenbach, R. P.; Escher, B. I.; Fenner, K.; Hofstetter, T. B.; Johnson, C. A.; von Gunten, U.; Wehrli, B., The Challenge of Micropollutants in Aquatic Systems. *Science* **2006,** *313* (5790), 1072.
18. Ma, Q.; Yu, Y.; Sindoro, M.; Fane, A. G.; Wang, R.; Zhang, H., Carbon-Based Functional Materials Derived from Waste for Water Remediation and Energy Storage. *Advanced Materials* **2017,** *29* (13), 1605361.
19. Zou, Y.; Wang, X.; Khan, A.; Wang, P.; Liu, Y.; Alsaedi, A.; Hayat, T.; Wang, X., Environmental Remediation and Application of Nanoscale Zero-Valent Iron and Its Composites for the Removal of Heavy Metal Ions: A Review. *Environmental Science & Technology* **2016,** *50* (14), 7290-7304.
20. Zhang, Q.; Yang, Q.; Phanlavong, P.; Li, Y.; Wang, Z.; Jiao, T.; Peng, Q., Highly Efficient Lead(II) Sequestration Using Size-Controllable Polydopamine Microspheres with Superior Application Capability and Rapid Capture. *ACS Sustainable Chemistry & Engineering* **2017,** *5* (5), 4161-4170.
21. Ghosh, P.; Samanta, A. N.; Ray, S., Reduction of COD and removal of Zn2+ from rayon industry wastewater by combined electro-Fenton treatment and chemical precipitation. *Desalination* **2011,** *266* (1), 213-217.
22. Bolisetty, S.; Mezzenga, R., Amyloid–carbon hybrid membranes for universal water purification. *Nature Nanotechnology* **2016,** *11*, 365.
23. Khan, M. A.; Ahmad, A.; Umar, K.; Nabi, S. A., Synthesis, Characterization, and Biological Applications of Nanocomposites for the Removal of Heavy Metals and Dyes. *Industrial & Engineering Chemistry Research* **2015,** *54* (1), 76-82.
24. Chen, F.; Gong, A. S.; Zhu, M.; Chen, G.; Lacey, S. D.; Jiang, F.; Li, Y.; Wang, Y.; Dai, J.; Yao, Y.; Song, J.; Liu, B.; Fu, K.; Das, S.; Hu, L., Mesoporous, Three-Dimensional Wood Membrane Decorated with Nanoparticles for Highly Efficient Water Treatment. *ACS Nano* **2017,** *11* (4), 4275-4282.
25. Aguila, B.; Sun, Q.; Perman, J. A.; Earl, L. D.; Abney, C. W.; Elzein, R.; Schlaf, R.; Ma, S., Efficient Mercury Capture Using Functionalized Porous Organic Polymer. *Advanced Materials* **2017,** *29* (31), 1700665.
26. Smith, S. C.; Rodrigues, D. F., Carbon-based nanomaterials for removal of chemical and biological contaminants from water: A review of mechanisms and applications. *Carbon* **2015,** *91*, 122-143.
27. Bessbousse, H.; Rhlalou, T.; Verchère, J. F.; Lebrun, L., Removal of heavy metal ions from aqueous solutions by filtration with a novel complexing membrane containing poly(ethyleneimine) in a poly(vinyl alcohol) matrix. *Journal of Membrane Science* **2008,** *307* (2), 249-259.
28. Singh, R.; Hankins, N., *Emerging Membrane Technology for Sustainable Water Treatment*. Elsevier 2016.
29. Pendergast, M. M.; Hoek, E. M. V., A review of water treatment membrane nanotechnologies. *Energy & Environmental Science* **2011,** *4* (6), 1946-1971.

30. Venkateswararao, A.; Thomas, K. R. J.; Lee, C.-P.; Li, C.-T.; Ho, K.-C., Organic dyes containing carbazole as donor and π-linker: optical, electrochemical, and photovoltaic properties. *ACS applied materials & interfaces* **2014,** *6* (4), 2528-2539.
31. Tehrani-Bagha, A. R.; Mahmoodi, N. M.; Menger, F. M., Degradation of a persistent organic dye from colored textile wastewater by ozonation. *Desalination* **2010,** *260* (1-3), 34-38.
32. Ong, W.-J.; Tan, L.-L.; Ng, Y. H.; Yong, S.-T.; Chai, S.-P., Graphitic carbon nitride (g-C3N4)-based photocatalysts for artificial photosynthesis and environmental remediation: are we a step closer to achieving sustainability? *Chemical reviews* **2016,** *116* (12), 7159-7329.
33. Han, Q.; Wang, B.; Gao, J.; Cheng, Z.; Zhao, Y.; Zhang, Z.; Qu, L., Atomically thin mesoporous nanomesh of graphitic C3N4 for high-efficiency photocatalytic hydrogen evolution. *ACS nano* **2016,** *10* (2), 2745-2751.
34. Yu, K.; Yang, S.; Liu, C.; Chen, H.; Li, H.; Sun, C.; Boyd, S. A., Degradation of organic dyes via bismuth silver oxide initiated direct oxidation coupled with sodium bismuthate based visible light photocatalysis. *Environmental science & technology* **2012,** *46* (13), 7318-7326.
35. Tiwari, J. N.; Mahesh, K.; Le, N. H.; Kemp, K. C.; Timilsina, R.; Tiwari, R. N.; Kim, K. S., Reduced graphene oxide-based hydrogels for the efficient capture of dye pollutants from aqueous solutions. *Carbon* **2013,** *56*, 173-182.
36. Zhao, S.; Li, K.; Jiang, S.; Li, J., Pd–Co based spinel oxides derived from pd nanoparticles immobilized on layered double hydroxides for toluene combustion. *Applied Catalysis B: Environmental* **2016,** *181*, 236-248.
37. Liu, Y.; Zhang, Y. Y.; Kou, Q. W.; Chen, Y.; Han, D. L.; Wang, D. D.; Lu, Z. Y.; Chen, L.; Yang, J. H.; Xing, S., Eco-friendly seeded Fe 3 O 4-Ag nanocrystals: A new type of highly efficient and low cost catalyst for methylene blue reduction. *RSC advances* **2018,** *8* (4), 2209-2218.
38. Xie, S.; Huang, P.; Kruzic, J. J.; Zeng, X.; Qian, H., A highly efficient degradation mechanism of methyl orange using Fe-based metallic glass powders. *Scientific reports* **2016,** *6*, 21947.
39. Wang, J. Q.; Liu, Y. H.; Chen, M. W.; Xie, G. Q.; Louzguine-Luzgin, D. V.; Inoue, A.; Perepezko, J. H., Rapid Degradation of Azo Dye by Fe-Based Metallic Glass Powder. *Advanced Functional Materials* **2012,** *22* (12), 2567-2570.
40. Jiao, T.; Zhao, H.; Zhou, J.; Zhang, Q.; Luo, X.; Hu, J.; Peng, Q.; Yan, X., Self-assembly reduced graphene oxide nanosheet hydrogel fabrication by anchorage of chitosan/silver and its potential efficient application toward dye degradation for wastewater treatments. *ACS Sustainable Chemistry & Engineering* **2015,** *3* (12), 3130-3139.
41. Chandra, R.; Mukhopadhyay, S.; Nath, M., TiO2@ ZIF-8: A novel approach of modifying micro-environment for enhanced photo-catalytic dye degradation and high usability of TiO2 nanoparticles. *Materials Letters* **2016,** *164*, 571-574.
42. Xie, S.; Wu, S.; Bao, S.; Wang, Y.; Zheng, Y.; Deng, D.; Huang, L.; Zhang, L.; Lee, M.; Huang, Z., Intelligent mesoporous materials for selective adsorption and mechanical release of organic pollutants from water. *Advanced Materials* **2018,** *30* (27), 1800683.
43. Wang, F.; Li, C.; Sun, L. D.; Xu, C. H.; Wang, J.; Yu, J. C.; Yan, C. H., Porous single-crystalline palladium nanoparticles with high catalytic activities. *Angewandte Chemie International Edition* **2012,** *51* (20), 4872-4876.
44. Xu, T.; Jiang, Q.; Ghim, D.; Liu, K.-K.; Sun, H.; Derami, H. G.; Wang, Z.; Tadepalli, S.; Jun, Y.-S.; Zhang, Q.; Singamaneni, S., Catalytically Active Bacterial Nanocellulose-Based Ultrafiltration Membrane. *Small* **2018,** *14* (15), 1704006.

45. Freakley, S. J.; He, Q.; Harrhy, J. H.; Lu, L.; Crole, D. A.; Morgan, D. J.; Ntainjua, E. N.; Edwards, J. K.; Carley, A. F.; Borisevich, A. Y.; Kiely, C. J.; Hutchings, G. J., Palladium-tin catalysts for the direct synthesis of H₂O₂ with high selectivity. *Science* **2016,** *351* (6276), 965.
46. Zhu, W.; Wu, Z.; Foo, G. S.; Gao, X.; Zhou, M.; Liu, B.; Veith, G. M.; Wu, P.; Browning, K. L.; Lee, H. N.; Li, H.; Dai, S.; Zhu, H., Taming interfacial electronic properties of platinum nanoparticles on vacancy-abundant boron nitride nanosheets for enhanced catalysis. *Nature Communications* **2017,** *8* (1), 15291.
47. Bhaskar, R.; Joshi, H.; Sharma, A. K.; Singh, A. K., Reusable Catalyst for Transfer Hydrogenation of Aldehydes and Ketones Designed by Anchoring Palladium as Nanoparticles on Graphene Oxide Functionalized with Selenated Amine. *ACS Applied Materials & Interfaces* **2017,** *9* (3), 2223-2231.
48. Cai, J.; Huang, J.; Wang, S.; Iocozzia, J.; Sun, Z.; Sun, J.; Yang, Y.; Lai, Y.; Lin, Z., Crafting Mussel-Inspired Metal Nanoparticle-Decorated Ultrathin Graphitic Carbon Nitride for the Degradation of Chemical Pollutants and Production of Chemical Resources. *Advanced Materials* **2019,** *31* (15), 1806314.
49. Lu, J.; Fang, J.; Li, J.; Wang, C.; He, Z.; Zhu, L.-P.; Xu, Z.-K.; Zeng, H., Polydopamine Nanotubes Decorated with Ag Nanoparticles as Catalyst for the Reduction of Methylene Blue. *ACS Applied Nano Materials* **2019**.
50. Song, Y.; Jiang, H.; Wang, B.; Kong, Y.; Chen, J., Silver-Incorporated Mussel-Inspired Polydopamine Coatings on Mesoporous Silica as an Efficient Nanocatalyst and Antimicrobial Agent. *ACS Applied Materials & Interfaces* **2018,** *10* (2), 1792-1801.
51. Yao, T.; Cui, T.; Wang, H.; Xu, L.; Cui, F.; Wu, J., A simple way to prepare Au@polypyrrole/Fe3O4 hollow capsules with high stability and their application in catalytic reduction of methylene blue dye. *Nanoscale* **2014,** *6* (13), 7666-7674.
52. Wang, Z.; Yang, H.-C.; He, F.; Peng, S.; Li, Y.; Shao, L.; Darling, S. B., Mussel-inspired surface engineering for water-remediation materials. *Matter* **2019,** *1* (1), 115-155.
53. Cui, K.; Yan, B.; Xie, Y.; Qian, H.; Wang, X.; Huang, Q.; He, Y.; Jin, S.; Zeng, H., Regenerable urchin-like Fe3O4@PDA-Ag hollow microspheres as catalyst and adsorbent for enhanced removal of organic dyes. *Journal of Hazardous Materials* **2018,** *350*, 66-75.
54. Batul, R.; Tamanna, T.; Khaliq, A.; Yu, A., Recent progress in the biomedical applications of polydopamine nanostructures. *Biomaterials science* **2017,** *5* (7), 1204-1229.
55. Liu, Y.; Ai, K.; Liu, J.; Deng, M.; He, Y.; Lu, L., Dopamine-Melanin Colloidal Nanospheres: An Efficient Near-Infrared Photothermal Therapeutic Agent for In Vivo Cancer Therapy. *Advanced Materials* **2013,** *25* (9), 1353-1359.
56. Zhang, D.-Y.; Zheng, Y.; Zhang, H.; Sun, J.-H.; Tan, C.-P.; He, L.; Zhang, W.; Ji, L.-N.; Mao, Z.-W., Delivery of Phosphorescent Anticancer Iridium(III) Complexes by Polydopamine Nanoparticles for Targeted Combined Photothermal-Chemotherapy and Thermal/Photoacoustic/Lifetime Imaging. *Advanced Science* **2018,** *5* (10), 1800581.
57. Seth, A.; Gholami Derami, H.; Gupta, P.; Wang, Z.; Rathi, P.; Gupta, R.; Cao, T.; Morrissey, J. J.; Singamaneni, S., Polydopamine–Mesoporous Silica Core–Shell Nanoparticles for Combined Photothermal Immunotherapy. *ACS applied materials & interfaces* **2020,** *12* (38), 42499-42510.
58. Kang, K.; Lee, S.; Kim, R.; Choi, I. S.; Nam, Y., Electrochemically Driven, Electrode-Addressable Formation of Functionalized Polydopamine Films for Neural Interfaces. *Angewandte Chemie* **2012,** *124* (52), 13278-13281.

59. Battaglini, M.; Marino, A.; Carmignani, A.; Tapeinos, C.; Cauda, V.; Ancona, A.; Garino, N.; Vighetto, V.; La Rosa, G.; Sinibaldi, E., Polydopamine nanoparticles as an organic and biodegradable multitasking tool for neuroprotection and remote neuronal stimulation. *ACS Applied Materials & Interfaces* **2020,** *12* (32), 35782-35798.
60. Golabchi, A.; Wu, B.; Cao, B.; Bettinger, C. J.; Cui, X. T., Zwitterionic polymer/polydopamine coating reduce acute inflammatory tissue responses to neural implants. *Biomaterials* **2019,** *225*, 119519.
61. Liu, X.; Cao, J.; Li, H.; Li, J.; Jin, Q.; Ren, K.; Ji, J., Mussel-Inspired Polydopamine: A Biocompatible and Ultrastable Coating for Nanoparticles in Vivo. *ACS Nano* **2013,** *7* (10), 9384-9395.
62. Zhang, P.; Xu, Q.; Du, J.; Wang, Y., Polydopamine-based nanoparticles with excellent biocompatibility for photothermally enhanced gene delivery. *RSC Advances* **2018,** *8* (60), 34596-34602.
63. Poinard, B.; Lam, S. A. E.; Neoh, K. G.; Kah, J. C. Y., Mucopenetration and biocompatibility of polydopamine surfaces for delivery in an Ex Vivo porcine bladder. *Journal of Controlled Release* **2019,** *300*, 161-173.
64. Gu, G. E.; Park, C. S.; Cho, H.-J.; Ha, T. H.; Bae, J.; Kwon, O. S.; Lee, J.-S.; Lee, C.-S., Fluorescent polydopamine nanoparticles as a probe for zebrafish sensory hair cells targeted in vivo imaging. *Scientific Reports* **2018,** *8* (1), 4393.
65. Ball, V., Polydopamine Nanomaterials: Recent Advances in Synthesis Methods and Applications. *Frontiers in Bioengineering and Biotechnology* **2018,** *6* (109).
66. Li, W.; Liu, Z.; Fontana, F.; Ding, Y.; Liu, D.; Hirvonen, J. T.; Santos, H. A., Tailoring Porous Silicon for Biomedical Applications: From Drug Delivery to Cancer Immunotherapy. *Advanced Materials* **2018,** *30* (24), 1703740.
67. Li, J.; Pu, K., Development of organic semiconducting materials for deep-tissue optical imaging, phototherapy and photoactivation. *Chemical Society Reviews* **2019,** *48* (1), 38-71.
68. Boyden, E. S.; Zhang, F.; Bamberg, E.; Nagel, G.; Deisseroth, K., Millisecond-timescale, genetically targeted optical control of neural activity. *Nature Neuroscience* **2005,** *8*, 1263-1268.
69. Zemelman, B. V.; Lee, G. A.; Ng, M.; Miesenböck, G., Selective Photostimulation of Genetically ChARGed Neurons. *Neuron* **2002,** *33* (1), 15-22.
70. Bernstein, J. G.; Boyden, E. S., Optogenetic tools for analyzing the neural circuits of behavior. *Trends in Cognitive Sciences* **2011,** *15* (12), 592-600.
71. Deisseroth, K.; Feng, G.; Majewska, A. K.; Miesenböck, G.; Ting, A.; Schnitzer, M. J., Next-generation optical technologies for illuminating genetically targeted brain circuits. *Journal of Neuroscience* **2006,** *26* (41), 10380-10386.
72. Callaway, E. M.; Yuste, R., Stimulating neurons with light. *Current opinion in neurobiology* **2002,** *12*, 587-592.
73. Wang, Y.; Guo, L., Nanomaterial-enabled neural stimulation. *Frontiers in Neuroscience* **2016,** *10*, 69.
74. Yoo, S.; Park, J.-H.; Nam, Y., Single-cell photothermal neuromodulation for functional mapping of neural networks. *ACS nano* **2018,** *13* (1), 544-551.
75. Rastogi, S. K.; Garg, R.; Scopelliti, M. G.; Pinto, B. I.; Hartung, J. E.; Kim, S.; Murphey, C. G. E.; Johnson, N.; San Roman, D.; Bezanilla, F.; Cahoon, J. F.; Gold, M. S.; Chamanzar, M.; Cohen-Karni, T., Remote nongenetic optical modulation of neuronal activity using fuzzy graphene. *Proceedings of the National Academy of Sciences* **2020,** *117* (24), 13339.

76. Yoo, S.; Hong, S.; Choi, Y.; Park, J.-H.; Nam, Y., Photothermal Inhibition of Neural Activity with Near-Infrared-Sensitive Nanotransducers. *ACS Nano* **2014,** *8* (8), 8040-8049.
77. Carvalho-de-Souza, João L.; Treger, Jeremy S.; Dang, B.; Kent, Stephen B. H.; Pepperberg, David R.; Bezanilla, F., Photosensitivity of Neurons Enabled by Cell-Targeted Gold Nanoparticles. *Neuron* **2015,** *86* (1), 207-217.
78. Munshi, R.; Qadri, S. M.; Zhang, Q.; Rubio, I. C.; Del Pino, P.; Pralle, A., Magnetothermal genetic deep brain stimulation of motor behaviors in awake, freely moving mice. *Elife* **2017,** *6*, e27069.
79. Kang, H.; Lee, G.-H.; Jung, H.; Lee, J. W.; Nam, Y., Inkjet-Printed Biofunctional Thermo-Plasmonic Interfaces for Patterned Neuromodulation. *ACS Nano* **2018,** *12* (2), 1128-1138.
80. Lee, J. W.; Jung, H.; Cho, H. H.; Lee, J. H.; Nam, Y., Gold nanostar-mediated neural activity control using plasmonic photothermal effects. *Biomaterials* **2018,** *153*, 59-69.
81. Eom, K.; Kim, J.; Choi, J. M.; Kang, T.; Chang, J. W.; Byun, K. M.; Jun, S. B.; Kim, S. J., Enhanced Infrared Neural Stimulation using Localized Surface Plasmon Resonance of Gold Nanorods. *Small* **2014,** *10* (19), 3853-3857.
82. Yoo, S.; Kim, R.; Park, J.-H.; Nam, Y., Electro-optical Neural Platform Integrated with Nanoplasmonic Inhibition Interface. *ACS Nano* **2016,** *10* (4), 4274-4281.
83. Yang, X.; Wang, Z.; Shao, L., Construction of oil-unidirectional membrane for integrated oil collection with lossless transportation and oil-in-water emulsion purification. *Journal of Membrane Science* **2018,** *549*, 67-74.
84. Sun, H.; Yang, X.; Zhang, Y.; Cheng, X.; Xu, Y.; Bai, Y.; Shao, L., Segregation-induced in situ hydrophilic modification of poly (vinylidene fluoride) ultrafiltration membranes via sticky poly (ethylene glycol) blending. *Journal of Membrane Science* **2018**.
85. Wu, X.; Jiang, Q.; Ghim, D.; Singamaneni, S.; Jun, Y.-S., Localized heating with a photothermal polydopamine coating facilitates a novel membrane distillation process. *Journal of Materials Chemistry A* **2018**.
86. Contreras Rodriguez, A. R.; Saiz-Poseu, J.; Garcia-Pardo, J.; Garcia, B.; Lorenzo, J.; Ojea-Jimenez, I.; Komilis, D.; Sedo, J.; Busque, F.; Sanchez, A.; Ruiz-Molina, D.; Font, X., Biocompatible polydopamine-like particles for the removal of heavy metals at extremely low concentrations. *RSC Advances* **2016,** *6* (46), 40058-40066.
87. Carpenter, A. W.; de Lannoy, C.-F.; Wiesner, M. R., Cellulose Nanomaterials in Water Treatment Technologies. *Environmental Science & Technology* **2015,** *49* (9), 5277-5287.
88. Wu, Z.-Y.; Liang, H.-W.; Chen, L.-F.; Hu, B.-C.; Yu, S.-H., Bacterial Cellulose: A Robust Platform for Design of Three Dimensional Carbon-Based Functional Nanomaterials. *Accounts of Chemical Research* **2016,** *49* (1), 96-105.
89. Tian, L.; Jiang, Q.; Liu, K.-K.; Luan, J.; Naik, R. R.; Singamaneni, S., Bacterial Nanocellulose-Based Flexible Surface Enhanced Raman Scattering Substrate. *Advanced Materials Interfaces* **2016,** *3* (15), n/a-n/a.
90. Tian, L.; Luan, J.; Liu, K.-K.; Jiang, Q.; Tadepalli, S.; Gupta, M. K.; Naik, R. R.; Singamaneni, S., Plasmonic Biofoam: A Versatile Optically Active Material. *Nano Letters* **2016,** *16* (1), 609-616.
91. Chen, L.-F.; Huang, Z.-H.; Liang, H.-W.; Gao, H.-L.; Yu, S.-H., Three-Dimensional Heteroatom-Doped Carbon Nanofiber Networks Derived from Bacterial Cellulose for Supercapacitors. *Advanced Functional Materials* **2014,** *24* (32), 5104-5111.

92. Chen, L.-F.; Zhang, X.-D.; Liang, H.-W.; Kong, M.; Guan, Q.-F.; Chen, P.; Wu, Z.-Y.; Yu, S.-H., Synthesis of nitrogen-doped porous carbon nanofibers as an efficient electrode material for supercapacitors. *ACS nano* **2012,** *6* (8), 7092-7102.
93. Tong, S.; Zheng, M.; Lu, Y.; Lin, Z.; Zhang, X.; He, P.; Zhou, H., Binder-free carbonized bacterial cellulose-supported ruthenium nanoparticles for Li-O2 batteries. *Chemical Communications* **2015,** *51* (34), 7302-7304.
94. Wang, B.; Li, X.; Luo, B.; Yang, J.; Wang, X.; Song, Q.; Chen, S.; Zhi, L., Pyrolyzed bacterial cellulose: a versatile support for lithium ion battery anode materials. *Small* **2013,** *9* (14), 2399-2404.
95. Liang, H.-W.; Guan, Q.-F.; Zhu, Z.; Song, L.-T.; Yao, H.-B.; Lei, X.; Yu, S.-H., Highly conductive and stretchable conductors fabricated from bacterial cellulose. *NPG Asia Mater* **2012,** *4*, e19.
96. Olsson, R. T.; Azizi Samir, M. A. S.; Salazar Alvarez, G.; BelovaL; StromV; Berglund, L. A.; IkkalaO; NoguesJ; Gedde, U. W., Making flexible magnetic aerogels and stiff magnetic nanopaper using cellulose nanofibrils as templates. *Nat Nano* **2010,** *5* (8), 584-588.
97. Jiang, Q.; Tian, L.; Liu, K. K.; Tadepalli, S.; Raliya, R.; Biswas, P.; Naik, R. R.; Singamaneni, S., Bilayered Biofoam for Highly Efficient Solar Steam Generation. *Advanced Materials* **2016,** *28* (42), 9400-9407.
98. Jiang, Q.; Kacica, C.; Soundappan, T.; Liu, K.-k.; Tadepalli, S.; Biswas, P.; Singamaneni, S., An in situ grown bacterial nanocellulose/graphene oxide composite for flexible supercapacitors. *Journal of Materials Chemistry A* **2017,** *5* (27), 13976-13982.
99. Xu, T.; Jiang, Q.; Ghim, D.; Liu, K. K.; Sun, H.; Derami, H. G.; Wang, Z.; Tadepalli, S.; Jun, Y. S.; Zhang, Q., Catalytically Active Bacterial Nanocellulose-Based Ultrafiltration Membrane. *Small* **2018**, 1704006.
100. Liu, Y.; Ai, K.; Liu, J.; Deng, M.; He, Y.; Lu, L., Dopamine-Melanin Colloidal Nanospheres: An Efficient Near-Infrared Photothermal Therapeutic Agent for In Vivo Cancer Therapy. *Advanced Materials* **2013,** *25* (9), 1353-1359.
101. Luo, H.; Gu, C.; Zheng, W.; Dai, F.; Wang, X.; Zheng, Z., Facile synthesis of novel size-controlled antibacterial hybrid spheres using silver nanoparticles loaded with poly-dopamine spheres. *RSC Advances* **2015,** *5* (18), 13470-13477.
102. Fu, J.; Chen, Z.; Wang, M.; Liu, S.; Zhang, J.; Zhang, J.; Han, R.; Xu, Q., Adsorption of methylene blue by a high-efficiency adsorbent (polydopamine microspheres): kinetics, isotherm, thermodynamics and mechanism analysis. *Chemical Engineering Journal* **2015,** *259*, 53-61.
103. Fu, J.; Xin, Q.; Wu, X.; Chen, Z.; Yan, Y.; Liu, S.; Wang, M.; Xu, Q., Selective adsorption and separation of organic dyes from aqueous solution on polydopamine microspheres. *Journal of colloid and interface science* **2016,** *461*, 292-304.
104. Poletto, M.; Pistor, V.; Santana, R. M. C.; Zattera, A. J., Materials produced from plant biomass: part II: evaluation of crystallinity and degradation kinetics of cellulose. *Materials Research* **2012,** *15* (3), 421-427.
105. Weng, C.-H., Modeling Pb(II) adsorption onto sandy loam soil. *Journal of Colloid and Interface Science* **2004,** *272* (2), 262-270.
106. Huang, S.; Yang, L.; Liu, M.; Phua, S. L.; Yee, W. A.; Liu, W.; Zhou, R.; Lu, X., Complexes of polydopamine-modified clay and ferric ions as the framework for pollutant-absorbing supramolecular hydrogels. *Langmuir* **2013,** *29* (4), 1238-1244.

107. Kinniburgh, D. G.; Milne, C. J.; Benedetti, M. F.; Pinheiro, J. P.; Filius, J.; Koopal, L. K.; Van Riemsdijk, W. H., Metal ion binding by humic acid: application of the NICA-Donnan model. *Environmental Science & Technology* **1996,** *30* (5), 1687-1698.
108. Jiang, Q.; Derami, H. G.; Ghim, D.; Cao, S.; Jun, Y.-S.; Singamaneni, S., Polydopamine-filled bacterial nanocellulose as a biodegradable interfacial photothermal evaporator for highly efficient solar steam generation. *Journal of Materials Chemistry A* **2017,** *5* (35), 18397-18402.
109. Bolisetty, S.; Mezzenga, R., Amyloid–carbon hybrid membranes for universal water purification. *Nature nanotechnology* **2016,** *11* (4), 365.
110. Lv, Y.; Zhang, C.; He, A.; Yang, S. J.; Wu, G. P.; Darling, S. B.; Xu, Z. K., Photocatalytic nanofiltration membranes with self-cleaning property for wastewater treatment. *Advanced Functional Materials* **2017,** *27* (27), 1700251.
111. Avlonitis, S. A.; Poulios, I.; Sotiriou, D.; Pappas, M.; Moutesidis, K., Simulated cotton dye effluents treatment and reuse by nanofiltration. *Desalination* **2008,** *221* (1-3), 259-267.
112. Gil, A.; Assis, F. C. C.; Albeniz, S.; Korili, S. A., Removal of dyes from wastewaters by adsorption on pillared clays. *Chemical Engineering Journal* **2011,** *168* (3), 1032-1040.
113. Jiang, D.; Chen, M.; Wang, H.; Zeng, G.; Huang, D.; Cheng, M.; Liu, Y.; Xue, W.; Wang, Z., The application of different typological and structural MOFs-based materials for the dyes adsorption. *Coordination Chemistry Reviews* **2019,** *380*, 471-483.
114. Hu, H.; Xin, J. H.; Hu, H.; Wang, X.; Miao, D.; Liu, Y., Synthesis and stabilization of metal nanocatalysts for reduction reactions–a review. *Journal of materials chemistry A* **2015,** *3* (21), 11157-11182.
115. Massaro, M.; Colletti, C. G.; Lazzara, G.; Guernelli, S.; Noto, R.; Riela, S., Synthesis and characterization of halloysite–cyclodextrin nanosponges for enhanced dyes adsorption. *ACS Sustainable Chemistry & Engineering* **2017,** *5* (4), 3346-3352.
116. Naushad, M.; Ali Khan, M.; Abdullah Alothman, Z.; Rizwan Khan, M.; Kumar, M., Adsorption of methylene blue on chemically modified pine nut shells in single and binary systems: isotherms, kinetics, and thermodynamic studies. *Desalination and Water Treatment* **2016,** *57* (34), 15848-15861.
117. Xiao, M.; Wang, Z.; Lyu, M.; Luo, B.; Wang, S.; Liu, G.; Cheng, H. M.; Wang, L., Hollow nanostructures for photocatalysis: advantages and challenges. *Advanced Materials* **2019,** *31* (38), 1801369.
118. Jiao, L.; Wang, Y.; Jiang, H. L.; Xu, Q., Metal–organic frameworks as platforms for catalytic applications. *Advanced Materials* **2018,** *30* (37), 1703663.
119. Wang, Z.; Ji, S.; Zhang, J.; He, F.; Xu, Z.; Peng, S.; Li, Y., Dual functional membrane with multiple hierarchical structures (MHS) for simultaneous and high-efficiency removal of dye and nano-sized oil droplets in water under high flux. *Journal of Membrane Science* **2018,** *564*, 317-327.
120. Khan, N. A.; Hasan, Z.; Jhung, S. H., Adsorptive removal of hazardous materials using metal-organic frameworks (MOFs): a review. *Journal of hazardous materials* **2013,** *244*, 444-456.
121. Islam, M. A.; Ahmed, M. J.; Khanday, W. A.; Asif, M.; Hameed, B. H., Mesoporous activated coconut shell-derived hydrochar prepared via hydrothermal carbonization-NaOH activation for methylene blue adsorption. *Journal of environmental management* **2017,** *203*, 237-244.

122. Shahabuddin, S.; Sarih, N. M.; Mohamad, S.; Baharin, S. N. A., Synthesis and characterization of Co 3 O 4 nanocube-doped polyaniline nanocomposites with enhanced methyl orange adsorption from aqueous solution. *RSC Advances* **2016,** *6* (49), 43388-43400.
123. Kurt, B. Z.; Durmus, Z.; Durmus, A., Preparation and characterization of platinum (Pt) and palladium (Pd) nanoparticle decorated graphene sheets and their utilization for the elimination of basic fuchsin and indigo carmine dyes. *Solid State Sciences* **2016,** *51*, 51-58.
124. Leyva-Pérez, A.; Oliver-Meseguer, J.; Rubio-Marqués, P.; Corma, A., Water-Stabilized Three- and Four-Atom Palladium Clusters as Highly Active Catalytic Species in Ligand-Free C□C Cross-Coupling Reactions. *Angewandte Chemie International Edition* **2013,** *52* (44), 11554-11559.
125. Kuvarega, A. T.; Krause, R. W. M.; Mamba, B. B., Nitrogen/Palladium-Codoped TiO2 for Efficient Visible Light Photocatalytic Dye Degradation. *The Journal of Physical Chemistry C* **2011,** *115* (45), 22110-22120.
126. Xiong, Z.; Zhang, L. L.; Ma, J.; Zhao, X. S., Photocatalytic degradation of dyes over graphene–gold nanocomposites under visible light irradiation. *Chemical Communications* **2010,** *46* (33), 6099-6101.
127. Zhang, Y.; Liu, S.; Lu, W.; Wang, L.; Tian, J.; Sun, X., In situ green synthesis of Au nanostructures on graphene oxide and their application for catalytic reduction of 4-nitrophenol. *Catalysis Science & Technology* **2011,** *1* (7), 1142-1144.
128. Zhang, Z.; Shao, C.; Zou, P.; Zhang, P.; Zhang, M.; Mu, J.; Guo, Z.; Li, X.; Wang, C.; Liu, Y., In situ assembly of well-dispersed gold nanoparticles on electrospun silica nanotubes for catalytic reduction of 4-nitrophenol. *Chemical Communications* **2011,** *47* (13), 3906-3908.
129. Ghasemzadeh, G.; Momenpour, M.; Omidi, F.; Hosseini, M. R.; Ahani, M.; Barzegari, A., Applications of nanomaterials in water treatment and environmental remediation. *Frontiers of Environmental Science & Engineering* **2014,** *8* (4), 471-482.
130. Gholami Derami, H.; Jiang, Q.; Ghim, D.; Cao, S.; Chandar, Y. J.; Morrissey, J. J.; Jun, Y.-S.; Singamaneni, S., A robust and scalable polydopamine/bacterial nanocellulose hybrid membrane for efficient wastewater treatment. *ACS Applied Nano Materials* **2019,** *2* (2), 1092-1101.
131. Sikhwivhilu, K.; Moutloali, R. M., Functionalized PVDF Membrane-immobilized Fe/Ni Bimetallic Nanoparticles for Catalytic Degradation of Methyl Orange Dye: A Comparative Study. *Materials Today: Proceedings* **2015,** *2* (7), 4070-4080.
132. Subair, R.; Tripathi, B. P.; Formanek, P.; Simon, F.; Uhlmann, P.; Stamm, M., Polydopamine modified membranes with in situ synthesized gold nanoparticles for catalytic and environmental applications. *Chemical Engineering Journal* **2016,** *295*, 358-369.
133. Kamal, T.; Ahmad, I.; Khan, S. B.; Asiri, A. M., Synthesis and catalytic properties of silver nanoparticles supported on porous cellulose acetate sheets and wet-spun fibers. *Carbohydrate Polymers* **2017,** *157*, 294-302.
134. Wang, Z.; Han, M.; Zhang, J.; He, F.; Xu, Z.; Ji, S.; Peng, S.; Li, Y., Designing preferable functional materials based on the secondary reactions of the hierarchical tannic acid (TA)-aminopropyltriethoxysilane (APTES) coating. *Chemical Engineering Journal* **2019,** *360*, 299-312.
135. Lin, J.; Ye, W.; Baltaru, M.-C.; Tang, Y. P.; Bernstein, N. J.; Gao, P.; Balta, S.; Vlad, M.; Volodin, A.; Sotto, A., Tight ultrafiltration membranes for enhanced separation of dyes and Na2SO4 during textile wastewater treatment. *Journal of Membrane Science* **2016,** *514*, 217-228.

136. Guan, B. Y.; Yu, L.; Lou, X. W., Formation of asymmetric bowl-like mesoporous particles via emulsion-induced interface anisotropic assembly. *Journal of the American Chemical Society* **2016,** *138* (35), 11306-11311.
137. Hong, G.; Shen, L.; Wang, M.; Yang, Y.; Wang, X.; Zhu, M.; Hsiao, B. S., Nanofibrous polydopamine complex membranes for adsorption of Lanthanum (III) ions. *Chemical engineering journal* **2014,** *244*, 307-316.
138. Dong, Z.; Wang, D.; Liu, X.; Pei, X.; Chen, L.; Jin, J., Bio-inspired surface-functionalization of graphene oxide for the adsorption of organic dyes and heavy metal ions with a superhigh capacity. *Journal of Materials Chemistry A* **2014,** *2* (14), 5034-5040.
139. Jiang, Q.; Tian, L.; Liu, K.-K.; Tadepalli, S.; Raliya, R.; Biswas, P.; Naik, R. R.; Singamaneni, S., Bilayered Biofoam for Highly Efficient Solar Steam Generation. *Advanced Materials* **2016,** *28* (42), 9400-9407.
140. Ghim, D.; Jiang, Q.; Cao, S.; Singamaneni, S.; Jun, Y.-S., Mechanically interlocked 1T/2H phases of MoS2 nanosheets for solar thermal water purification. *Nano Energy* **2018,** *53*, 949-957.
141. Liu, K.-K.; Jiang, Q.; Kacica, C.; Derami, H. G.; Biswas, P.; Singamaneni, S., Flexible solid-state supercapacitor based on tin oxide/reduced graphene oxide/bacterial nanocellulose. *RSC Advances* **2018,** *8* (55), 31296-31302.
142. Shaheen, F.; Badshah, A.; Gielen, M.; Dusek, M.; Fejfarova, K.; de Vos, D.; Mirza, B., Synthesis, characterization, antibacterial and cytotoxic activity of new palladium (II) complexes with dithiocarbamate ligands: X-ray structure of bis (dibenzyl-1-S: S′-dithiocarbamato) Pd (II). *Journal of organometallic chemistry* **2007,** *692* (14), 3019-3026.
143. Ul-Islam, M.; Khattak, W. A.; Kang, M.; Kim, S. M.; Khan, T.; Park, J. K., Effect of post-synthetic processing conditions on structural variations and applications of bacterial cellulose. *Cellulose* **2013,** *20* (1), 253-263.
144. Rahul, R.; Singh, R. K.; Bera, B.; Devivaraprasad, R.; Neergat, M., The role of surface oxygenated-species and adsorbed hydrogen in the oxygen reduction reaction (ORR) mechanism and product selectivity on Pd-based catalysts in acid media. *Physical Chemistry Chemical Physics* **2015,** *17* (23), 15146-15155.
145. Wang, B.; Yan, T.; Chang, T.; Wei, J.; Zhou, Q.; Yang, S.; Fang, T., Palladium supported on reduced graphene oxide as a high-performance catalyst for the dehydrogenation of dodecahydro-N-ethylcarbazole. *Carbon* **2017,** *122*, 9-18.
146. Dubey, A. V.; Kumar, A. V., A biomimetic magnetically recoverable palladium nanocatalyst for the Suzuki cross-coupling reaction. *RSC Advances* **2016,** *6* (52), 46864-46870.
147. Xu, L.; Wu, X.-C.; Zhu, J.-J., Green preparation and catalytic application of Pd nanoparticles. *Nanotechnology* **2008,** *19* (30), 305603.
148. Wei, H.; Ren, J.; Han, B.; Xu, L.; Han, L.; Jia, L., Stability of polydopamine and poly (DOPA) melanin-like films on the surface of polymer membranes under strongly acidic and alkaline conditions. *Colloids and Surfaces B: Biointerfaces* **2013,** *110*, 22-28.
149. Shah, L. A.; Sayed, M.; Fayaz, M.; Bibi, I.; Nawaz, M.; Siddiq, M., Ag-Loaded Thermo-Sensitive Composite Microgels for Enhanced Catalytic Reduction of Methylene Blue. *Nanotechnology for Environmental Engineering* **2017,** *2* (1), 14.
150. Ma, X.; Guo, Y.; Jin, J.; Zhao, B.; Song, W., Bi-Functional Reduced Graphene Oxide/AgCo Composite Nanosheets: An Efficient Catalyst and SERS Substrate for Monitoring the Catalytic Reactions. *RSC Advances* **2017,** *7* (67), 41962-41969.

151. Kojima, Y.; Suzuki, K.-i.; Fukumoto, K.; Sasaki, M.; Yamamoto, T.; Kawai, Y.; Hayashi, H., Hydrogen generation using sodium borohydride solution and metal catalyst coated on metal oxide. *International Journal of Hydrogen Energy* **2002,** *27* (10), 1029-1034.
152. Ali, F.; Khan, S. B.; Kamal, T.; Alamry, K. A.; Asiri, A. M.; Sobahi, T. R. A., Chitosan Coated Cotton Cloth Supported Zero-Valent Nanoparticles: Simple but Economically Viable, Efficient and Easily Retrievable Catalysts. *Scientific Reports* **2017,** *7* (1), 16957.
153. Ucar, A.; Findik, M.; Gubbuk, I. H.; Kocak, N.; Bingol, H., Catalytic Degradation of Organic Dye Using Reduced Graphene Oxide–Polyoxometalate Nanocomposite. *Materials Chemistry and Physics* **2017,** *196*, 21-28.
154. Robina, B.; Jawayria, N.; Ayesha, S.; Khalida, N.; Ahmad, I.; Abdullah, G. A.-S.; Zahoor, H. F., Chemical Reduction of Methylene Blue in the Presence of Nanocatalysts: A Critical Review. *Reviews in Chemical Engineering* **2019,** (0), 20180047.
155. Naseem, K.; Farooqi, Z. H.; Begum, R.; Irfan, A., Removal of Congo red dye from aqueous medium by its catalytic reduction using sodium borohydride in the presence of various inorganic nano-catalysts: a review. *Journal of cleaner production* **2018,** *187*, 296-307.
156. Ravikumar, K. V. G.; Dubey, S.; pulimi, M.; Chandrasekaran, N.; Mukherjee, A., Scale-Up Synthesis of Zero-Valent Iron Nanoparticles and Their Applications for Synergistic Degradation of Pollutants With Sodium Borohydride. *Journal of Molecular Liquids* **2016,** *224*, 589-598.
157. Chen, Z.-x.; Jin, X.-y.; Chen, Z.; Megharaj, M.; Naidu, R., Removal of Methyl Orange from Aqueous Solution Using Bentonite-Supported Nanoscale Zero-Valent Iron. *Journal of Colloid and Interface Science* **2011,** *363* (2), 601-607.
158. Ilunga, A. K.; Khoza, T.; Tjabadi, E.; Meijboom, R., Effective Catalytic Reduction of Methyl Orange Catalyzed by the Encapsulated Random Alloy Palladium-Gold Nanoparticles Dendrimer. *ChemistrySelect* **2017,** *2* (30), 9803-9809.
159. Mondal, A.; Adhikary, B.; Mukherjee, D., Room-temperature synthesis of air stable cobalt nanoparticles and their use as catalyst for methyl orange dye degradation. *Colloids and Surfaces A: Physicochemical and Engineering Aspects* **2015,** *482*, 248-257.
160. Lin, F.-h.; Doong, R.-a., Highly Efficient Reduction of 4-nitrophenol by Heterostructured Gold-Magnetite Nanocatalysts. *Applied Catalysis A: General* **2014,** *486*, 32-41.
161. Li, J.; Liu, C.-y.; Liu, Y., Au/Graphene Hydrogel: Synthesis, Characterization and its Use for Catalytic Reduction of 4-Nitrophenol. *Journal of Materials Chemistry* **2012,** *22* (17), 8426-8430.
162. Bae, S.; Gim, S.; Kim, H.; Hanna, K., Effect of NaBH4 on Properties of Nanoscale Zero-Valent Iron and its Catalytic Activity for Reduction of p-Nitrophenol. *Applied Catalysis B: Environmental* **2016,** *182*, 541-549.
163. Davis, R. E.; Bromels, E.; Kibby, C. L., Boron hydrides. III. Hydrolysis of sodium borohydride in aqueous solution. *Journal of the American Chemical Society* **1962,** *84* (6), 885-892.
164. Chen, W.; Mo, J.; Du, X.; Zhang, Z.; Zhang, W., Biomimetic dynamic membrane for aquatic dye removal. *Water research* **2019,** *151*, 243-251.
165. Zhang, Y.; Cheng, X.; Jiang, X.; Urban, J. J.; Lau, C. H.; Liu, S.; Shao, L., Robust natural nanocomposites realizing unprecedented ultrafast precise molecular separations. *Materials Today* **2020**.
166. Zhang, Y.; Ma, J.; Shao, L., Ultra-thin Trinity Coating Enabled by Competitive Reactions for Unparalleled Molecular Separations. *Journal of Materials Chemistry A* **2020**.

167. Vinodgopal, K.; Kamat, P. V., Enhanced Rates of Photocatalytic Degradation of an Azo Dye Using SnO2/TiO2 Coupled Semiconductor Thin Films. *Environmental Science & Technology* **1995,** *29* (3), 841-845.
168. Zheng, Y.; Zhong, X.; Li, Z.; Xia, Y., Successive, Seed-Mediated Growth for the Synthesis of Single-Crystal Gold Nanospheres with Uniform Diameters Controlled in the Range of 5–150 nm. *Particle & Particle Systems Characterization* **2014,** *31* (2), 266-273.
169. Vesely, M. D.; Kershaw, M. H.; Schreiber, R. D.; Smyth, M. J., Natural Innate and Adaptive Immunity to Cancer. *Annual Review of Immunology* **2011,** *29* (1), 235-271.
170. Dunn, G. P.; Bruce, A. T.; Ikeda, H.; Old, L. J.; Schreiber, R. D., Cancer immunoediting: from immunosurveillance to tumor escape. *Nature Immunology* **2002,** *3* (11), 991-998.
171. O'Donnell, J. S.; Teng, M. W. L.; Smyth, M. J., Cancer immunoediting and resistance to T cell-based immunotherapy. *Nature Reviews Clinical Oncology* **2018**.
172. Beatty, G. L.; Gladney, W. L., Immune Escape Mechanisms as a Guide for Cancer Immunotherapy. *Clinical Cancer Research* **2015,** *21* (4), 687.
173. Mellman, I.; Coukos, G.; Dranoff, G., Cancer immunotherapy comes of age. *Nature* **2011,** *480* (7378), 480-489.
174. Disis, M. L., Mechanism of Action of Immunotherapy. *Seminars in Oncology* **2014,** *41*, S3-S13.
175. Huang, L.; Xu, H.; Peng, G., TLR-mediated metabolic reprogramming in the tumor microenvironment: potential novel strategies for cancer immunotherapy. *Cell Mol Immunol* **2018,** *15* (5), 428-437.
176. Bocanegra Gondan, A. I.; Ruiz-de-Angulo, A.; Zabaleta, A.; Gómez Blanco, N.; Cobaleda-Siles, B. M.; García-Granda, M. J.; Padro, D.; Llop, J.; Arnaiz, B.; Gato, M.; Escors, D.; Mareque-Rivas, J. C., Effective cancer immunotherapy in mice by polyIC-imiquimod complexes and engineered magnetic nanoparticles. *Biomaterials* **2018,** *170*, 95-115.
177. Xu, C.; Nam, J.; Hong, H.; Xu, Y.; Moon, J. J., Positron Emission Tomography-Guided Photodynamic Therapy with Biodegradable Mesoporous Silica Nanoparticles for Personalized Cancer Immunotherapy. *ACS Nano* **2019,** *13* (10), 12148-12161.
178. Seth, A.; Heo, M. B.; Lim, Y. T., Poly (γ-glutamic acid) based combination of water-insoluble paclitaxel and TLR7 agonist for chemo-immunotherapy. *Biomaterials* **2014,** *35* (27), 7992-8001.
179. Phuengkham, H.; Ren, L.; Shin, I. W.; Lim, Y. T., Nanoengineered Immune Niches for Reprogramming the Immunosuppressive Tumor Microenvironment and Enhancing Cancer Immunotherapy. *Advanced Materials* **2019,** *31* (34), 1803322.
180. Rodell, C. B.; Arlauckas, S. P.; Cuccarese, M. F.; Garris, C. S.; Li, R.; Ahmed, M. S.; Kohler, R. H.; Pittet, M. J.; Weissleder, R., TLR7/8-agonist-loaded nanoparticles promote the polarization of tumour-associated macrophages to enhance cancer immunotherapy. *Nature Biomedical Engineering* **2018,** *2* (8), 578-588.
181. Im, S.; Lee, J.; Park, D.; Park, A.; Kim, Y.-M.; Kim, W. J., Hypoxia-Triggered Transforming Immunomodulator for Cancer Immunotherapy via Photodynamically Enhanced Antigen Presentation of Dendritic Cell. *ACS Nano* **2019,** *13* (1), 476-488.
182. Chen, Q.; Xu, L.; Liang, C.; Wang, C.; Peng, R.; Liu, Z., Photothermal therapy with immune-adjuvant nanoparticles together with checkpoint blockade for effective cancer immunotherapy. *Nature Communications* **2016,** *7* (1), 13193.
183. Yang, W.; Zhu, G.; Wang, S.; Yu, G.; Yang, Z.; Lin, L.; Zhou, Z.; Liu, Y.; Dai, Y.; Zhang, F.; Shen, Z.; Liu, Y.; He, Z.; Lau, J.; Niu, G.; Kiesewetter, D. O.; Hu, S.; Chen, X., In

Situ Dendritic Cell Vaccine for Effective Cancer Immunotherapy. *ACS Nano* **2019,** *13* (3), 3083-3094.
184. Ye, X.; Liang, X.; Chen, Q.; Miao, Q.; Chen, X.; Zhang, X.; Mei, L., Surgical Tumor-Derived Personalized Photothermal Vaccine Formulation for Cancer Immunotherapy. *ACS Nano* **2019,** *13* (3), 2956-2968.
185. Ni, K.; Luo, T.; Lan, G.; Culbert, A.; Song, Y.; Wu, T.; Jiang, X.; Lin, W., Nanoscale Metal-organic Frameworks Mediate Photodynamic Therapy and Deliver CpG Oligodeoxynucleotides to Enhance Antigen Presentation and Cancer Immunotherapy. *Angewandte Chemie International Edition* **2019,** *0* (ja).
186. Embgenbroich, M.; Burgdorf, S., Current Concepts of Antigen Cross-Presentation. *Frontiers in immunology* **2018,** *9*, 1643-1643.
187. Sánchez-Paulete, A. R.; Teijeira, A.; Cueto, F. J.; Garasa, S.; Pérez-Gracia, J. L.; Sánchez-Arráez, A.; Sancho, D.; Melero, I., Antigen cross-presentation and T-cell cross-priming in cancer immunology and immunotherapy. *Annals of Oncology* **2017,** *28* (suppl_12), xii44-xii55.
188. Alloatti, A.; Kotsias, F.; Magalhaes, J. G.; Amigorena, S., Dendritic cell maturation and cross-presentation: timing matters! *Immunological reviews* **2016,** *272* (1), 97-108.
189. Gil-Torregrosa, B. C.; Lennon-Duménil, A. M.; Kessler, B.; Guermonprez, P.; Ploegh, H. L.; Fruci, D.; Endert, P. V.; Amigorena, S., Control of cross-presentation during dendritic cell maturation. *European Journal of Immunology* **2004,** *34* (2), 398-407.
190. Reis e Sousa, C., Dendritic cells in a mature age. *Nature Reviews Immunology* **2006,** *6* (6), 476-483.
191. Dhodapkar, M. V.; Dhodapkar, K. M.; Palucka, A. K., Interactions of tumor cells with dendritic cells: balancing immunity and tolerance. *Cell Death Differ* **2008,** *15* (1), 39-50.
192. Makkouk, A.; Weiner, G. J., Cancer Immunotherapy and Breaking Immune Tolerance: New Approaches to an Old Challenge. *Cancer Research* **2015,** *75* (1), 5.
193. Mende, I.; Engleman, E. G., Breaking Self-Tolerance to Tumor-Associated Antigens by In Vivo Manipulation of Dendritic Cells. In *Immunological Tolerance: Methods and Protocols*, Fairchild, P. J., Ed. Humana Press: Totowa, NJ, 2007; pp 457-468.
194. Ma, F.; Zhang, J.; Zhang, J.; Zhang, C., The TLR7 agonists imiquimod and gardiquimod improve DC-based immunotherapy for melanoma in mice. *Cell Mol Immunol* **2010,** *7* (5), 381-388.
195. Seth, A.; Lee, H.; Cho, M. Y.; Park, C.; Korm, S.; Lee, J.-Y.; Choi, I.; Lim, Y. T.; Hong, K. S., Combining vasculature disrupting agent and Toll-like receptor 7/8 agonist for cancer therapy. *Oncotarget* **2017,** *8* (3), 5371-5381.
196. Weber, A.; Zimmermann, C.; Mausberg, A. K.; Kieseier, B. C.; Hartung, H. P.; Hofstetter, H. H., Induction of pro-inflammatory cytokine production in thymocytes by the immune response modifiers Imiquimod and Gardiquimod™. *International Immunopharmacology* **2013,** *17* (2), 427-431.
197. Zou, B. B.; Wang, F.; Li, L.; Cheng, F. W.; Jin, R.; Luo, X.; Zhu, L. X.; Geng, X.; Zhang, S. Q., Activation of Toll-like receptor 7 inhibits the proliferation and migration, and induces the apoptosis of pancreatic cancer cells. *Molecular Medicine Reports* **2015,** *12* (4), 6079-6085.
198. Wang, C.; Ma, Z.; Wang, T.; Su, Z., Synthesis, Assembly, and Biofunctionalization of Silica-Coated Gold Nanorods for Colorimetric Biosensing. *Advanced Functional Materials* **2006,** *16* (13), 1673-1678.

199. Shen, S.; Tang, H.; Zhang, X.; Ren, J.; Pang, Z.; Wang, D.; Gao, H.; Qian, Y.; Jiang, X.; Yang, W., Targeting mesoporous silica-encapsulated gold nanorods for chemo-photothermal therapy with near-infrared radiation. *Biomaterials* **2013,** *34* (12), 3150-3158.
200. Tian, L.; Gandra, N.; Singamaneni, S., Monitoring controlled release of payload from gold nanocages using surface enhanced Raman scattering. *ACS nano* **2013,** *7* (5), 4252-4260.
201. Tran, T. H.; Tran, T. T. P.; Truong, D. H.; Nguyen, H. T.; Pham, T. T.; Yong, C. S.; Kim, J. O., Toll-like receptor-targeted particles: A paradigm to manipulate the tumor microenvironment for cancer immunotherapy. *Acta Biomaterialia* **2019,** *94*, 82-96.
202. Stary, G.; Bangert, C.; Tauber, M.; Strohal, R.; Kopp, T.; Stingl, G., Tumoricidal activity of TLR7/8-activated inflammatory dendritic cells. *The Journal of experimental medicine* **2007,** *204* (6), 1441-1451.
203. Moon, G. D.; Choi, S.-W.; Cai, X.; Li, W.; Cho, E. C.; Jeong, U.; Wang, L. V.; Xia, Y., A new theranostic system based on gold nanocages and phase-change materials with unique features for photoacoustic imaging and controlled release. *Journal of the American Chemical Society* **2011,** *133* (13), 4762-4765.
204. Won, S. M.; Song, E.; Zhao, J.; Li, J.; Rivnay, J.; Rogers, J. A., Recent advances in materials, devices, and systems for neural interfaces. *Advanced Materials* **2018,** *30* (30), 1800534.
205. Li, J.; Duan, H.; Pu, K., Nanotransducers for near-infrared Photoregulation in biomedicine. *Advanced Materials* **2019,** *31* (33), 1901607.
206. Fattahi, P.; Yang, G.; Kim, G.; Abidian, M. R., A review of organic and inorganic biomaterials for neural interfaces. *Advanced materials* **2014,** *26* (12), 1846-1885.
207. Jeong, Y. C.; Lee, H. E.; Shin, A.; Kim, D. G.; Lee, K. J.; Kim, D., Progress in Brain-Compatible Interfaces with Soft Nanomaterials. *Advanced Materials* **2020**, 1907522.
208. Obidin, N.; Tasnim, F.; Dagdeviren, C., The Future of Neuroimplantable Devices: A Materials Science and Regulatory Perspective. *Advanced Materials* **2020,** *32* (15), 1901482.
209. Mikhail G. Shapiro; Kazuaki Homma; Sebastian Villarreal; Richter, C.-P.; Bezanilla, F., Infrared light excites cells by changing their electrical capacitance. *Nature Communications* **2012,** *3*, 736.
210. Yong, J.; Needham, K.; Brown, W. G. A.; Nayagam, B. A.; McArthur, S. L.; Yu, A.; Stoddart, P. R., Gold-Nanorod-Assisted Near-Infrared Stimulation of Primary Auditory Neurons. *Advanced Healthcare Materials* **2014**, n/a-n/a.
211. Dobson, J., Remote control of cellular behaviour with magnetic nanoparticles. *Nat Nanotechnol* **2008,** *3* (3), 139-143.
212. Huang, H.; Delikanli, S.; Zeng, H.; Ferkey, D. M.; Pralle, A., Remote control of ion channels and neurons through magnetic-field heating of nanoparticles. *Nat Nanotechnol* **2010,** *5* (8), 602-606.
213. Ai, K.; Liu, Y.; Ruan, C.; Lu, L.; Lu, G., Sp2 C-Dominant N-Doped Carbon Sub-micrometer Spheres with a Tunable Size: A Versatile Platform for Highly Efficient Oxygen-Reduction Catalysts. *Advanced Materials* **2013,** *25* (7), 998-1003.
214. Dante, S.; Petrelli, A.; Petrini, E. M.; Marotta, R.; Maccione, A.; Alabastri, A.; Quarta, A.; De Donato, F.; Ravasenga, T.; Sathya, A.; Cingolani, R.; Proietti Zaccaria, R.; Berdondini, L.; Barberis, A.; Pellegrino, T., Selective Targeting of Neurons with Inorganic Nanoparticles: Revealing the Crucial Role of Nanoparticle Surface Charge. *ACS Nano* **2017,** *11* (7), 6630-6640.
215. Smith, A. M.; Mancini, M. C.; Nie, S., Second window for in vivo imaging. *Nature Nanotechnology* **2009,** *4* (11), 710-711.

216. Weissleder, R., A clearer vision for in vivo imaging. *Nature Biotechnology* **2001,** *19* (4), 316-317.
217. Aslan, B.; Guler, S.; Tevlek, A.; Aydin, H. M., Evaluation of collagen foam, poly(l-lactic acid) nanofiber mesh, and decellularized matrices for corneal regeneration. *Journal of Biomedical Materials Research Part B: Applied Biomaterials* **2018,** *106* (6), 2157-2168.
218. Mackenzie, S. J.; Yi, J. L.; Singla, A.; Russell, T. M.; Osterhout, D. J.; Calancie, B., Cauda equina repair in the rat: Part 3. Axonal regeneration across Schwann cell—Seeded collagen foam. *Muscle & Nerve* **2018,** *57* (1), E78-E84.
219. Lian, X.; Hsiao, C.; Wilson, G.; Zhu, K.; Hazeltine, L. B.; Azarin, S. M.; Raval, K. K.; Zhang, J.; Kamp, T. J.; Palecek, S. P., Cozzarelli Prize Winner: Robust cardiomyocyte differentiation from human pluripotent stem cells via temporal modulation of canonical Wnt signaling. *Proc. Natl. Acad. Sci. USA* **2012,** *109*, E1848-E1857.
220. Tohyama, S.; Hattori, F.; Sano, M.; Hishiki, T.; Nagahata, Y.; Matsuura, T.; Hashimoto, H.; Suzuki, T.; Yamashita, H.; Satoh, Y., Distinct metabolic flow enables large-scale purification of mouse and human pluripotent stem cell-derived cardiomyocytes. *Cell stem cell* **2013,** *12* (1), 127-137.
221. Zheng, Y.; Zhong, X.; Li, Z.; Xia, Y., Successive, Seed-Mediated Growth for the Synthesis of Single-Crystal Gold Nanospheres with Uniform Diameters Controlled in the Range of 5–150 nm. *Particle & Particle Systems Characterization* **2014,** *31* (2), 266-273.
222. Poletto, M.; Pistor, V.; Santana, R. M. C.; Zattera, A. J., Materials produced from plant biomass: part II: evaluation of crystallinity and degradation kinetics of cellulose. *Materials Research* **2012,** *15*, 421-427.
223. EPA, Report of the Food Quality Protection Act (FQPA) Tolerance Reassessment Eligibility Decision (TRED) for Boric Acid/Sodium Borate Salts. *https://www3.epa.gov/pesticides/chem_search/reg_actions/reregistration/tred_PC-011001_1-Jul-06.pdf*.
224. Ghosh, S.; Avellini, T.; Petrelli, A.; Kriegel, I.; Gaspari, R.; Almeida, G.; Bertoni, G.; Cavalli, A.; Scotognella, F.; Pellegrino, T.; Manna, L., Colloidal CuFeS2 Nanocrystals: Intermediate Fe d-Band Leads to High Photothermal Conversion Efficiency. *Chemistry of Materials* **2016,** *28* (13), 4848-4858.

Appendix

Appendix 1

Gold nanoparticle (AuNP) synthesis: AuNPs were synthesized using a seed-mediated method.[221] Au seeds with a diameter of 3 nm were synthesized by addition of ice-cold sodium borohydride (0.6 ml, 10 mM) into a mixture of hexadecyltrimethylammonium bromide CTAB (9.75 ml, 0.1 M) and gold chloride trihydrate (0.25 ml, 10 mM) under vigorous stirring. AuNPs with a dimeter of 5 nm were synthesized by mixing CTAC (2 ml, 0.2 M), ascorbic acid (1.5 ml, 0.1 M) and 3 nm as-prepared seed (1 ml) and addition of gold chloride solution (2 ml, 0.5 mM) under vigorous stirring for 15 minutes. For 10 nm AuNPs, CTAC (7 ml, 0.2 M), ascorbic acid (5.25 ml, 0.1 M) and 3 nm as-prepared seed (0.175 ml) were mixed and added with gold chloride solution (7 ml, 0.5 mM) under vigorous stirring for 15 minutes.

Table S2. 1 Parameters of Langmuir Isotherm models for adsorption of Pb (II) and R6G onto PDA/BNC foams.

Pollutant	Membrane	Langmuir model parameters		
		Q_{max} (mg/g)	$1/K_L$ (mg/L)	R^2
Pb (II)	PDA/BNC	16.85	20.25	0.992
	BNC	4.95	16.08	0.984
R6G	PDA/BNC	8.83	15.63	0.992
	BNC	1.82	13.57	0.970

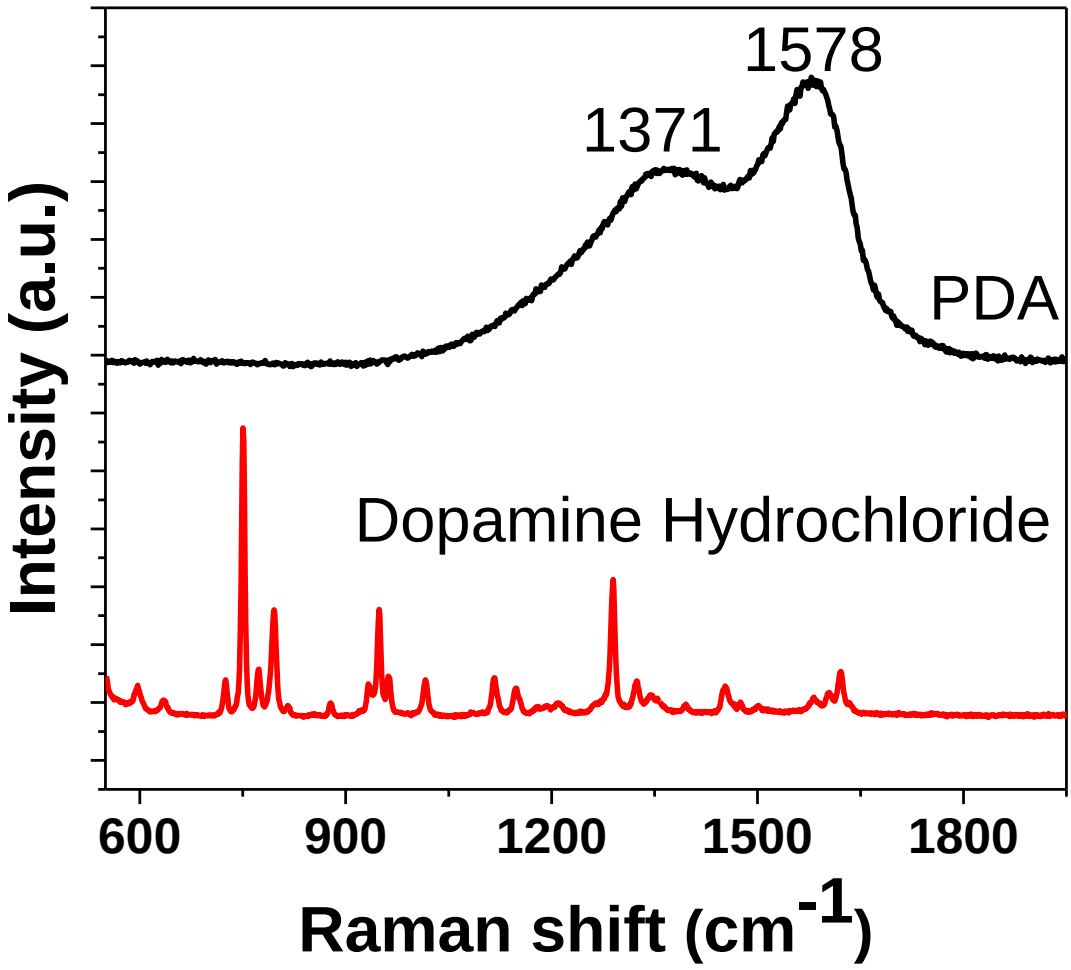

Figure S2. 1 Raman spectra of the dopamine monomer and polydopamine particles.

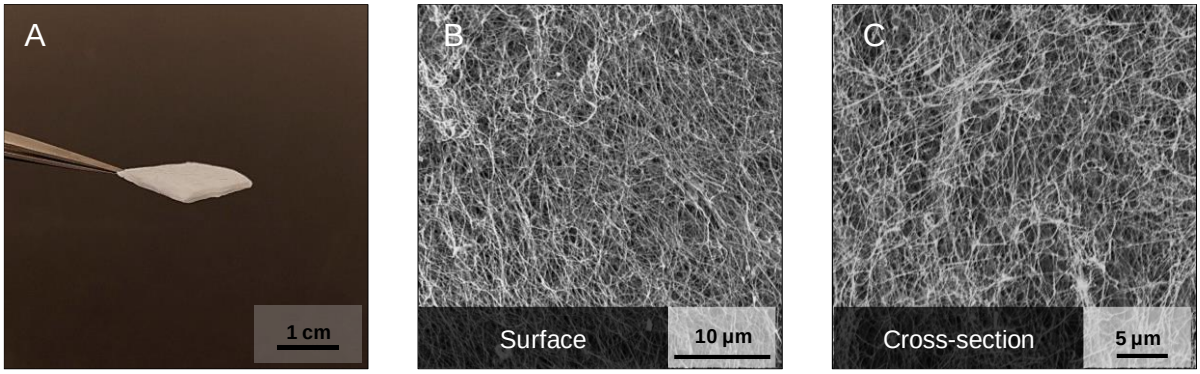

Figure S2. 2 (A) Photograph and SEM images of (B) surface and (C) cross-section of the freeze-dried pristine BNC (BNC foam).

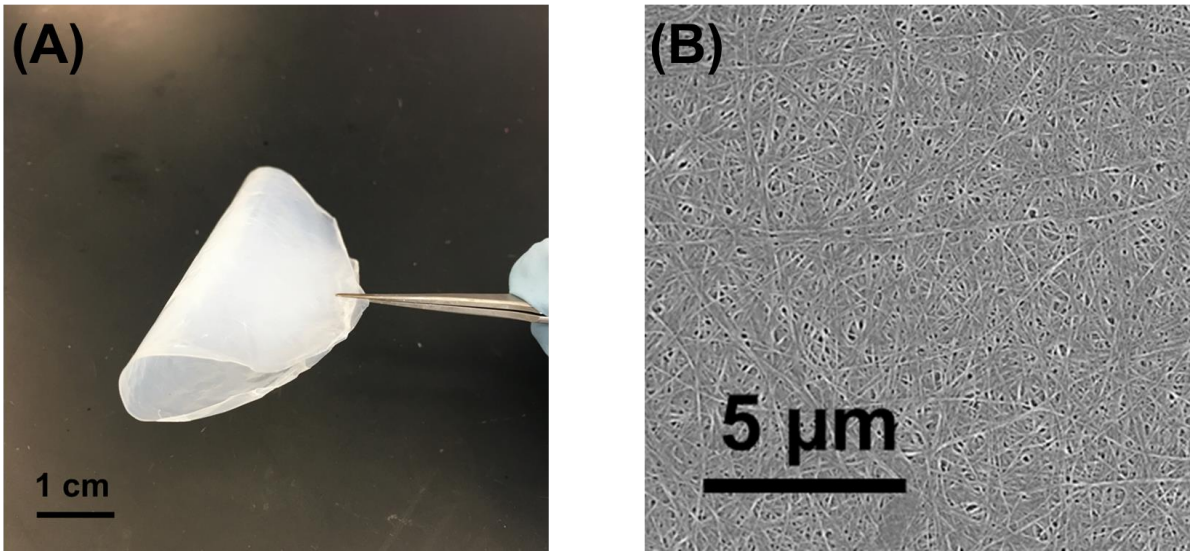

Figure S2. 3 Optical image (A) and SEM of the surface (B) of the BNC membrane (air-dried BNC).

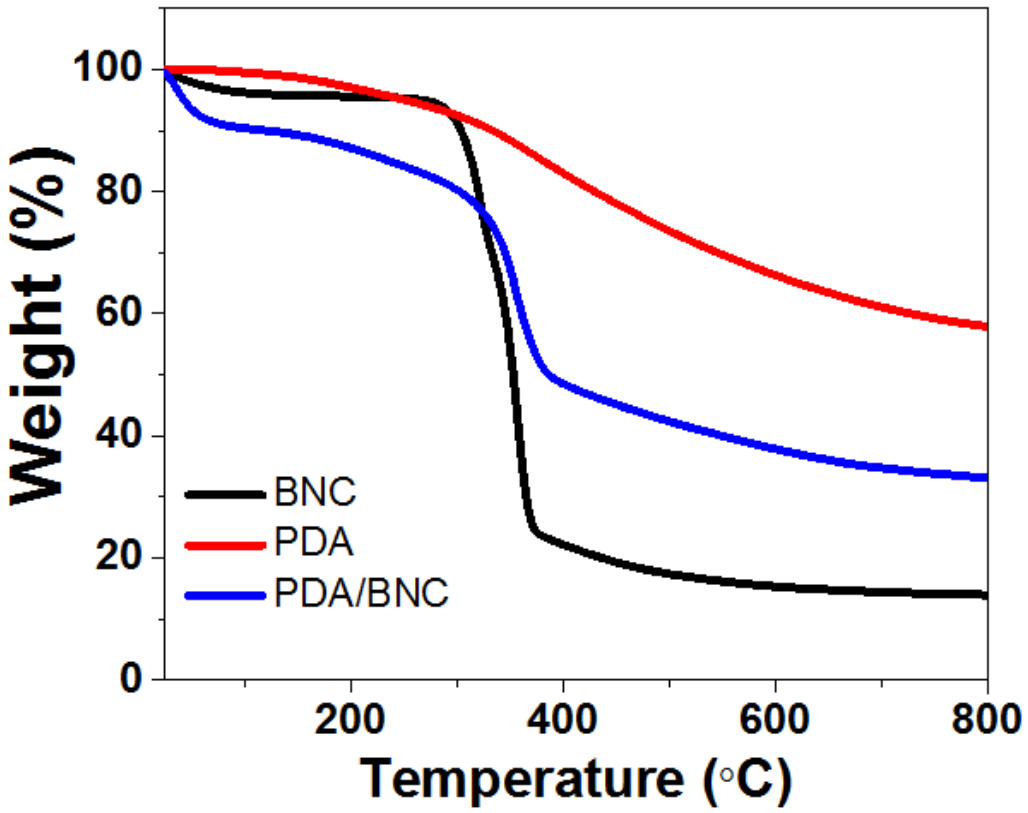

Figure S2. 4 Weight loss profiles of BNC, PDA particles and PDA/BNC composite as measured by thermogravimetric analysis (TGA).

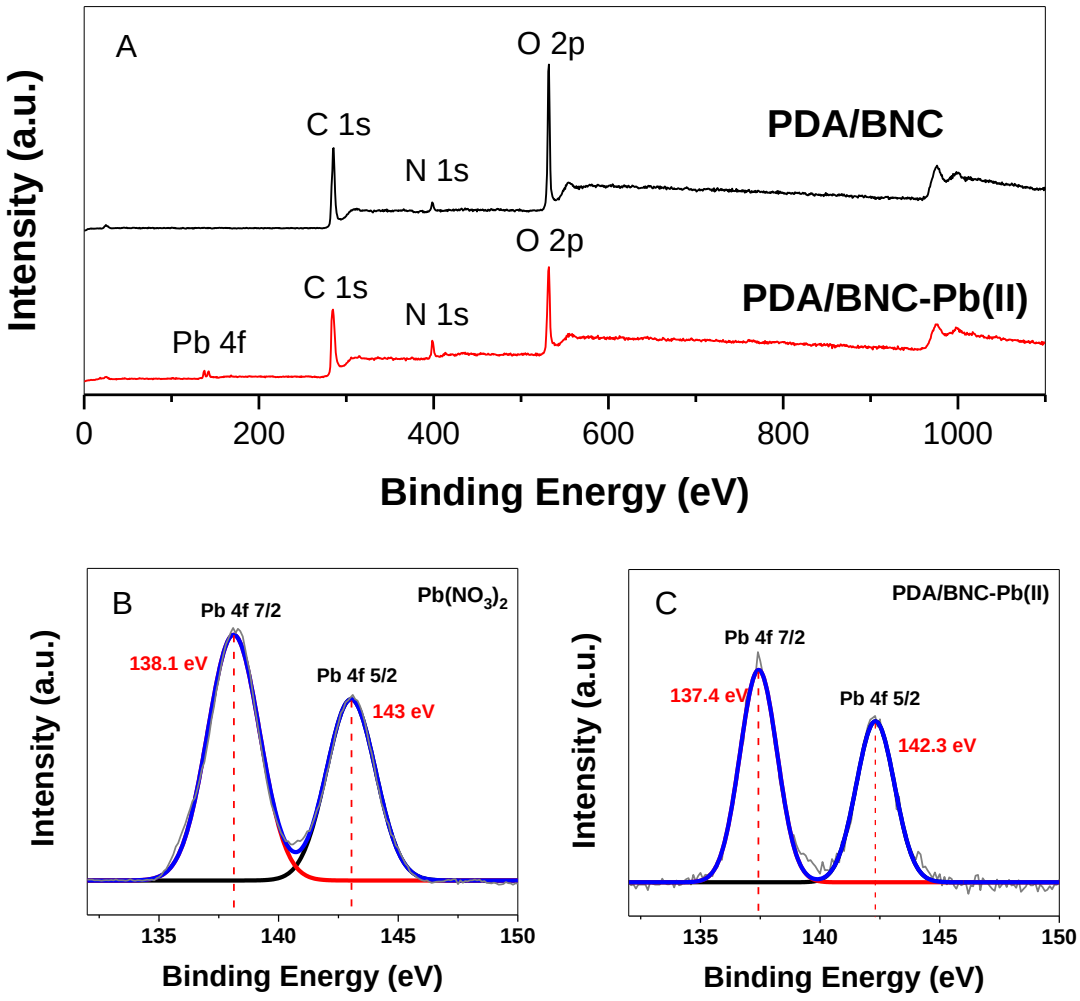

Figure S2. 5 (A) XPS spectra of PDA/BNC before and after the Pb (II) adsorption test. Pb 4f spectra of Pb (II) in (B) $Pb(NO_3)_2$ powder and (C) after adsorption on PDA/BNC.

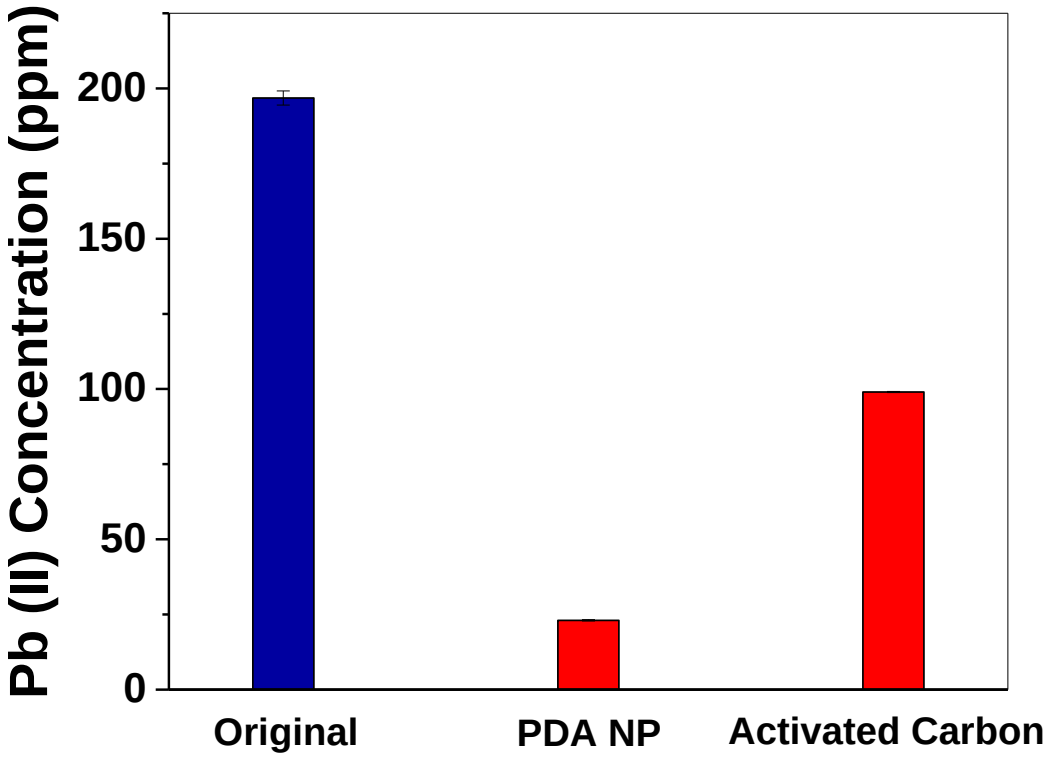

Figure S2. 6 Comparison between PDA nanoparticle and activated carbon in Pb (II) adsorption (the weight of the both adsorbents was 80 mg, NOTE: error bars are small compared to scale of the graph).

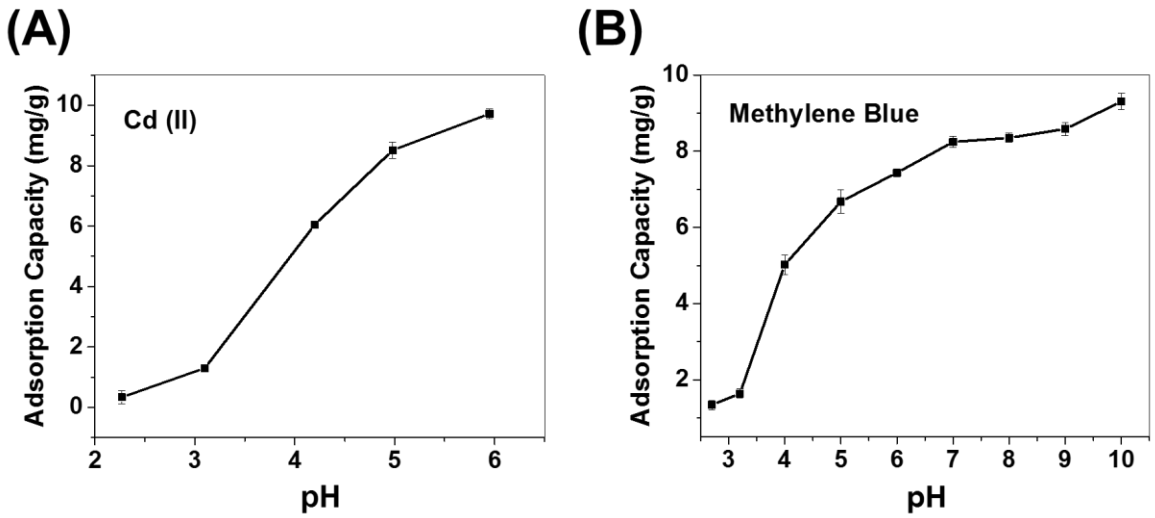

Figure S2. 7 Adsorption capacities of PDA/BNC foam for Cd (II) (A), and MB (B) at different pH values (Experiments carried out at room temperature and the initial concentration of the contaminants was 200 ppm).

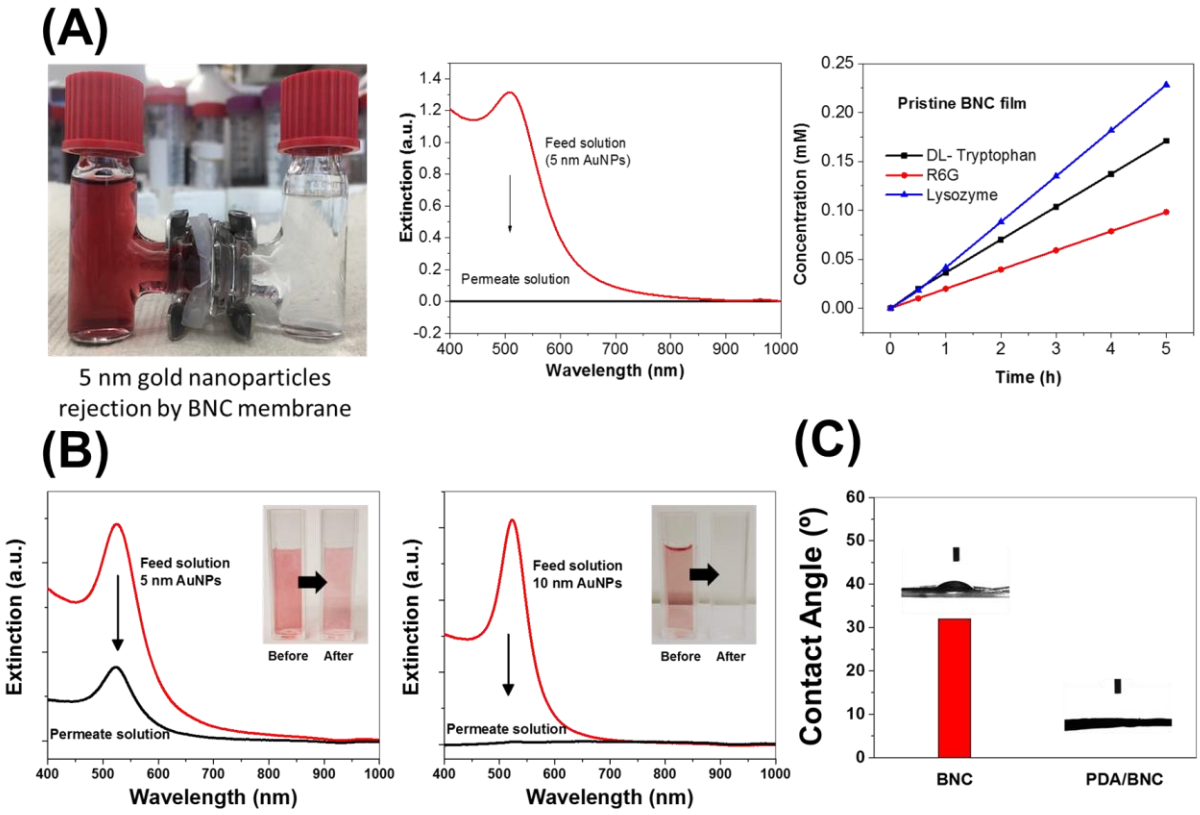

Figure S2. 8 (A) Pore size investigation for BNC membrane. 5 nm AuNP solution diffusion test (left and center) that shows no particle diffuses through the membrane and a upper limit for the pore size. The diffusion test repeated for DL-Tryptophan, R6G, and Lysozyme (right), and all these molecules are diffusing through the BNC membrane giving a lower limit of roughly 1 nm pore size for the membrane. (B) Pore size study for PDA/BNC membrane using 5 nm (left) and 10 nm (right) AuNPs using vacuum filtration at 0.7 bar pressure. The 5 nm AuNPs penetrate through the membrane suggesting that pore size of the membrane is larger than 5 nm, while 10 nm AuNPs dont penetrate through the membrane even after 4 hours of solution filtration. This

gives a lower limit of 5 nm and upper limit of 10 nm for the pore size of the PDA/BNC membrane. (C) Contact angle measurements for pristine BNC and PDA/BNC membranes.

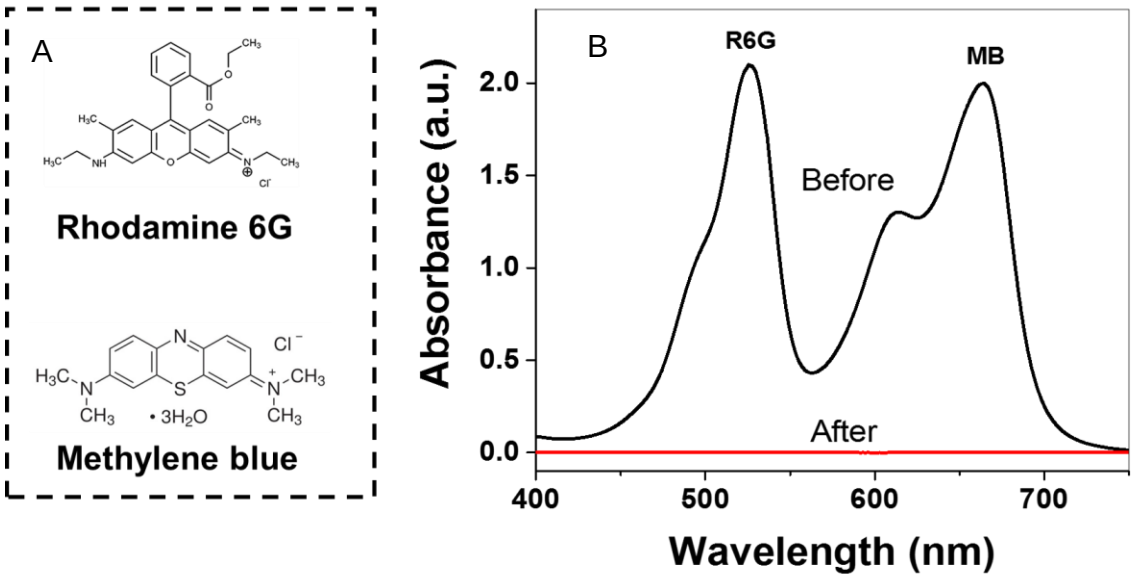

Figure S2. 9 (A) Chemical structures of model positively charged dyes used in cocktail filtration test. (B) UV-Vis spectra of the cocktail solution before and after the filtration.

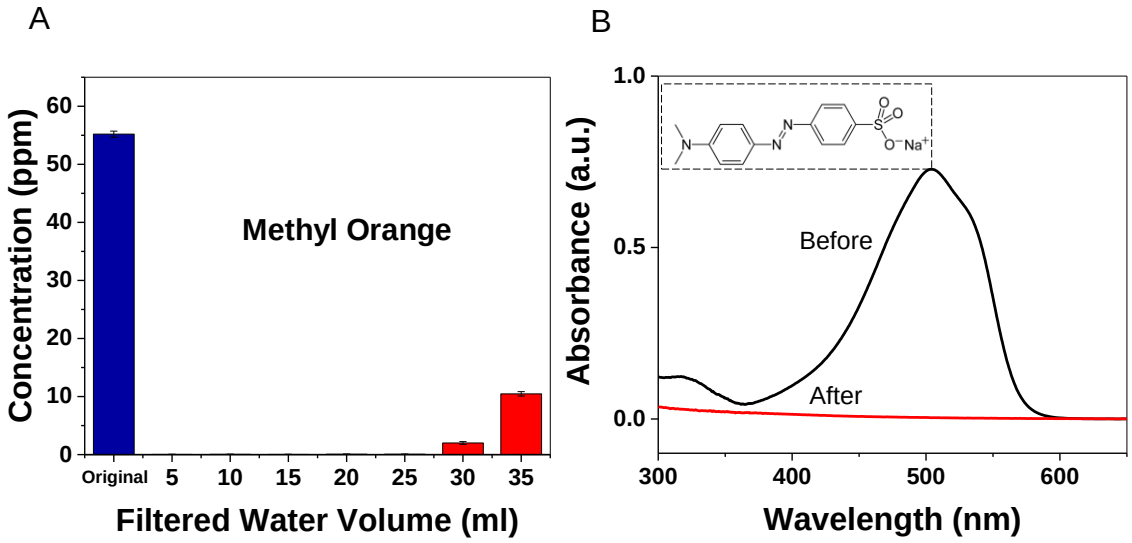

Figure S2. 10 (A) Concentrations of negatively charged MO in feed and permeate water solutions during filtration test (initial pH value was ~2.4). (B) UV-Vis spectra of the MO before and after the filtration test (inset shows the chemical structure of MO).

Appendix 2

Gold nanoparticle (AuNP) synthesis: AuNPs were synthesized using a seed-mediated method.[221] Au seeds with a diameter of 3 nm were synthesized by addition of ice-cold sodium borohydride (0.6 ml, 10 mM) into a mixture of hexadecyltrimethylammonium bromide CTAB (9.75 ml, 0.1 M) and gold chloride trihydrate (0.25 ml, 10 mM) under vigorous stirring. AuNPs with a dimeter of 5 nm were synthesized by mixing CTAC (2 ml, 0.2 M), ascorbic acid (1.5 ml, 0.1 M) and 3 nm as-prepared seed (1 ml) and addition of gold chloride solution (2 ml, 0.5 mM) under vigorous stirring for 15 minutes. For 10 nm AuNPs, CTAC (7 ml, 0.2 M), ascorbic acid (5.25 ml, 0.1 M) and 3 nm as-prepared seed (0.175 ml) were mixed and added with gold chloride solution (7 ml, 0.5 mM) under vigorous stirring for 15 minutes.

Thermogravimetric Analysis (TGA): Thermogravimetric analysis (TGA) was employed to analyze the mass loading of Pd in Pd-BNC and Pd-mPDA-BNC membranes (Figure S3.3). For Pd-mPDA-BNC, the first mass loss of ~6% can be attributed to residual/absorbed water at 100 ^{o}C, second mass loss of ~6% at 280 ^{o}C can be attributed to the degradation of cellulose and mPDA particles and a mass loss of ~30% at 350 ^{o}C can be attributed to the decomposition of cellulose residue, which generates CO_2 and H_2O, and further degradation of mPDA particles.[222] After heating to 600 ^{o}C, the remaining mass (~46%) is composed of Pd nanoparticles and carbon residues. The mass of carbon residues for mPDA-BNC at 600 ^{o}C is ~25.7%. Based on the above discussion, the mass loading of Pd in Pd-mPDA-BNC membrane was calculated to be ~20.3 wt%. However, in the case of Pd-BNC, the mass loading of Pd was calculated to be ~13.6 wt%.

Environmental Impact of Sodium Borate: Environmental Protection Agency's (EPA) guidelines states that Lowest Observed Adverse Effect Level (LOAEL) for oral exposure (e.g. drinking) of boric acid and sodium borate is between 32 mg/kg/day and 46 mg/kg/day.[223] LOAEL shows the lowest dose at which there was an observed toxic or adverse effect. By assuming that a toddler has an average weight of 15 kg and drinks 2 liters of water every day, the LOAEL limit would be between 480 mg and 690 mg. In our experiments, maximum final concentration of $NaBH_4$ is 2.5 mM and by assuming that 100% of it has reacted and turned into sodium borate, 2 liters of filtered water contain 329 mg of sodium borate, which is below the lower limit of LOAEL.

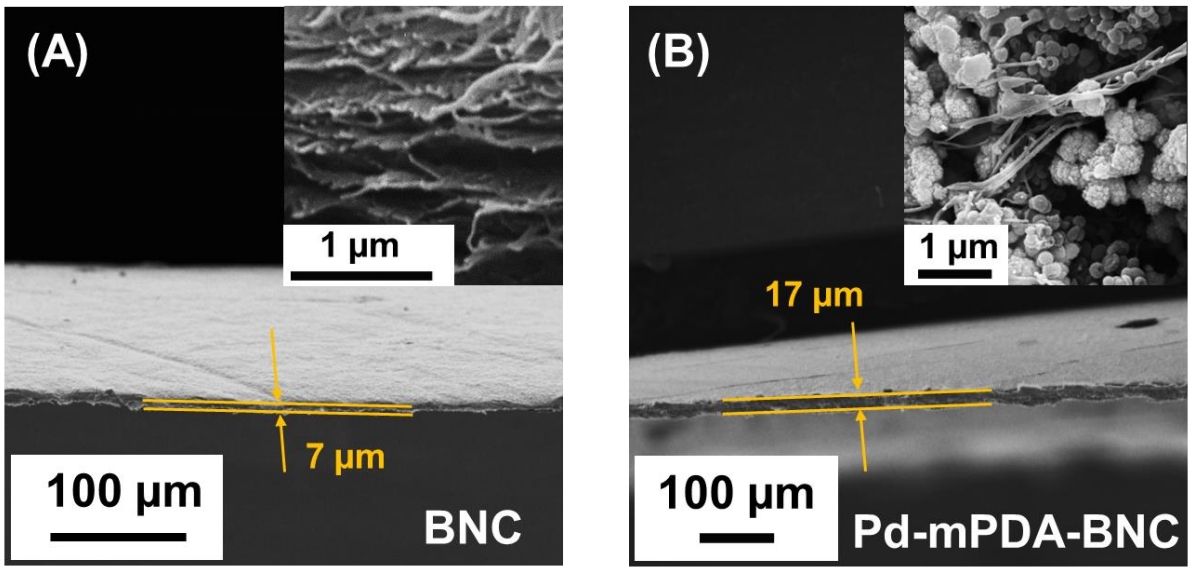

Figure S3. 1 Cross section SEM images of the (A) BNC membrane and (B) Pd-mPDA-BNC membrane. (Insets show corresponding higher magnification SEM images.)

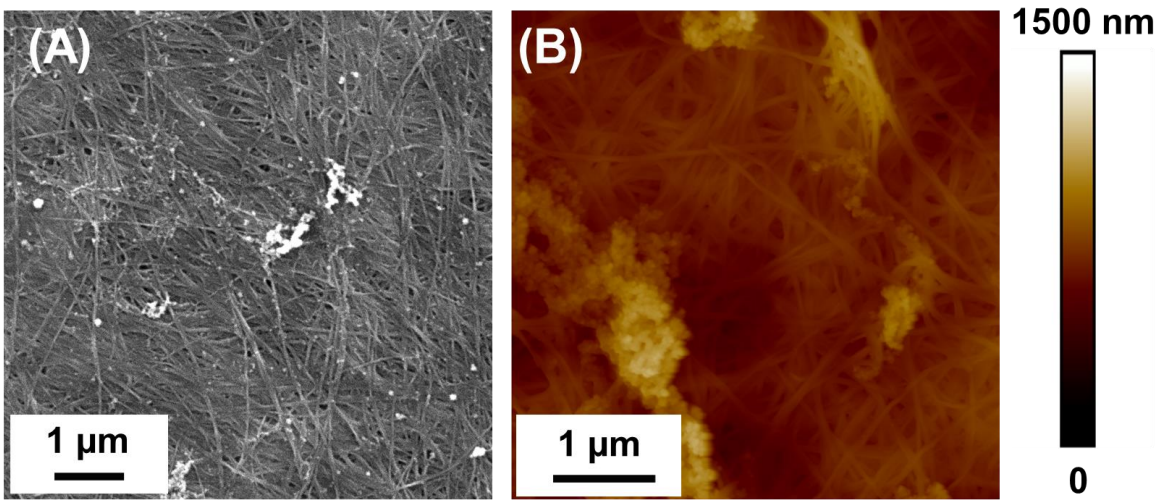

Figure S3. 2 (A) SEM and (B) AFM images of the surface of the Pd-BNC membrane.

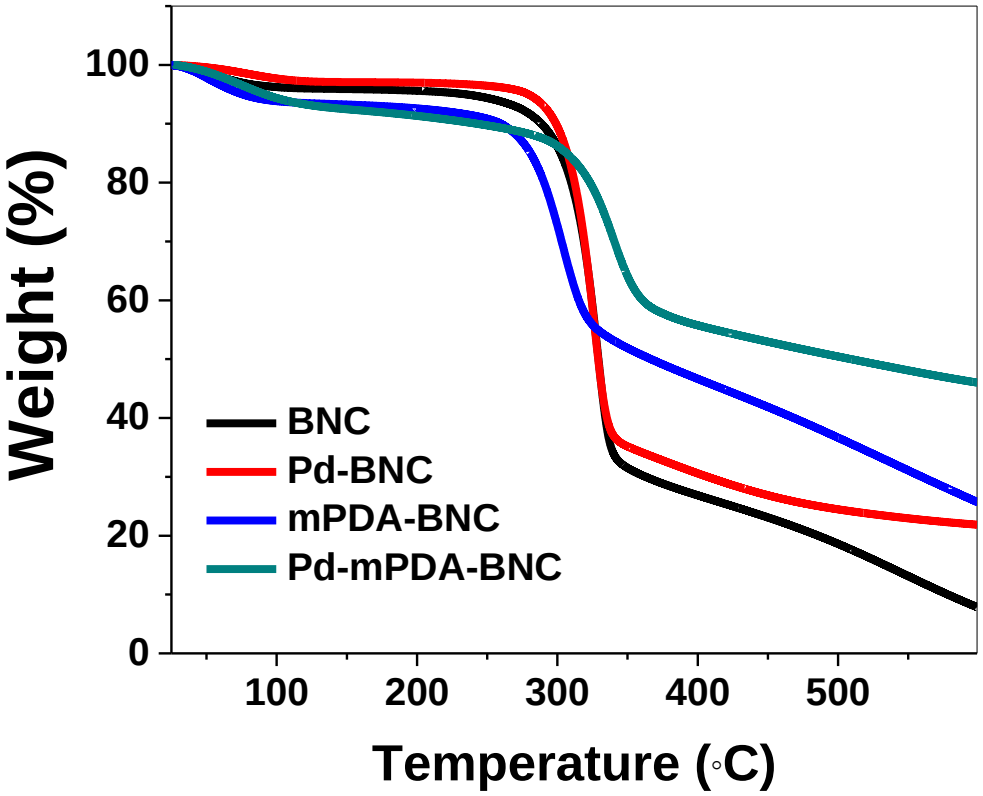

Figure S3. 3 Weight loss profiles of BNC, Pd-BNC, mPDA-BNC and Pd-mPDA-BNC composites obtained by TGA.

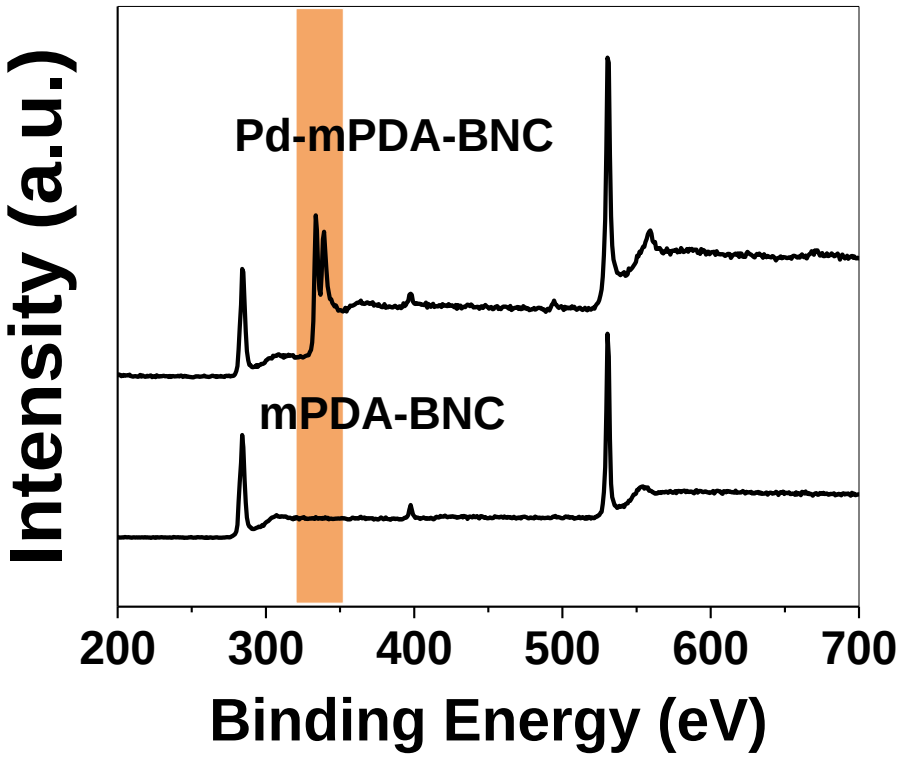

Figure S3. 4 XPS spectra of mPDA-BNC and Pd-mPDA-BNC membranes confirming the presence of metallic Pd.

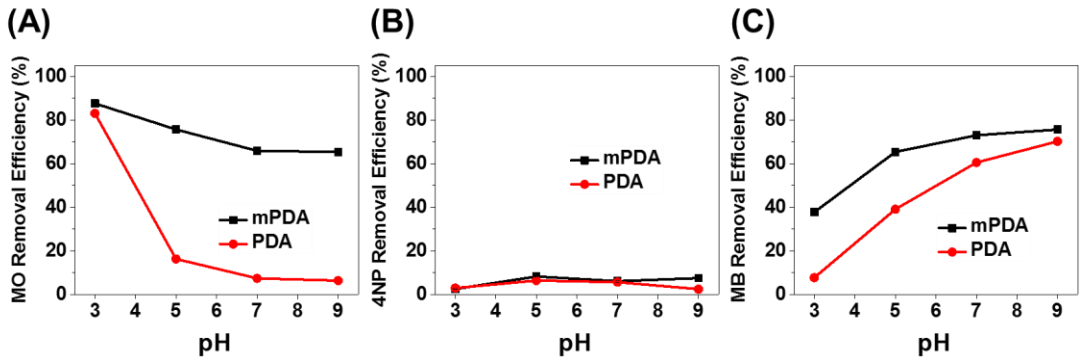

Figure S3. 5 mPDA vs PDA nanoparticle efficiency in removing (A) MO, (B) 4NP and (C) MB at different pH values.

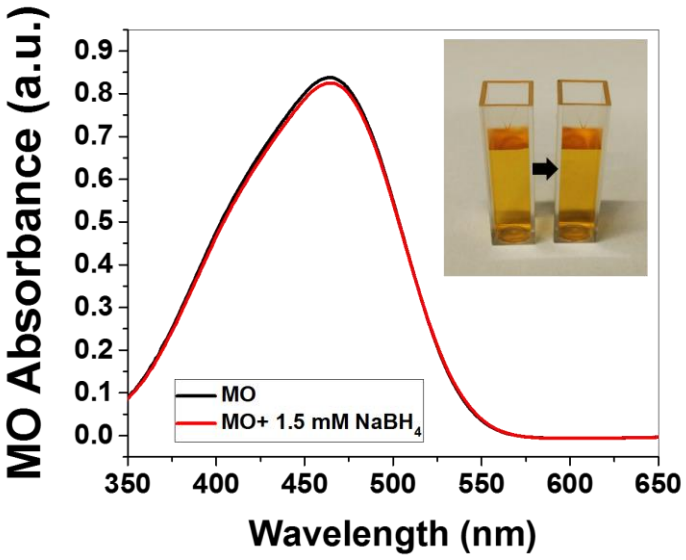

Figure S3. 6 Effect of 1.5 mM $NaBH_4$ on the absorbance of the MO after 20 minutes.

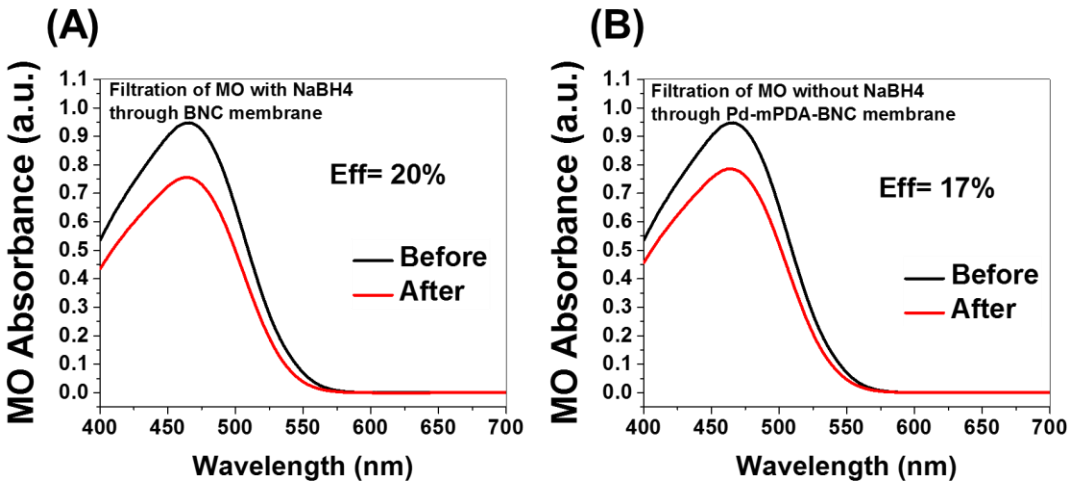

Figure S3. 7 (A) Absorbance of MO solution before and after filtration through BNC membrane in presence of $NaBH_4$. (B) Absorbance of MO solution before and after filtration through Pd-mPDA-BNC membrane in the absence of $NaBH_4$.

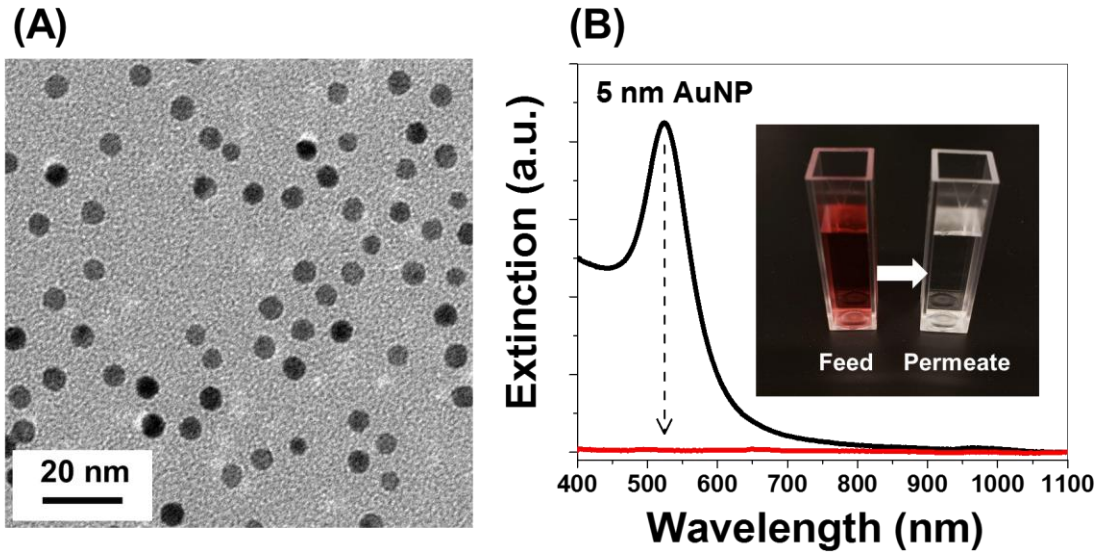

Figure S3. 8 Particle rejection test. (A) TEM image of the 5 nm AuNPs used for praticles rejection test on Pd-mPDA-BNC membrane. (B) Extinction spectra of the AuNP feed solution and the permeate after filtration through Pd-mPDA-BNC membrane (Inset shows corresponding optical image of the solution).

Appendix 3

Analysis of TGA data: 31% of the weight of PDA was retained after heating to 600 °C under nitrogen. Mesoporous silica-coated PDA showed an initial mass loss of about 20% at 100 °C, due to water evaporation. It lost its weight less dramatically mainly because of the presence of the silica coating and retained 56% of the total weight after heating to 600 °C. This indicates that silica coating accounts for about 53% of the weight of core-shell PDA@$mSiO_2$ nanoparticles (Figure 4.1H).

Loading and release of LT680: Successful loading and controlled release of payload from the PDA@$mSiO_2$ nanoparticles was further investigated using a fluorescent dye, LT680. Following the loading procedure, the PDA@$mSiO_2$ nanoparticles exhibited significantly higher fluorescence intensity compared to the supernatant (corresponding to the unloaded dye in solution), confirming the successful loading of dye in solution (Figure S4.5A). Under laser irradiation (power of 14 mW/mm^2) the fluorescence intensity of solution monotonically increased with time. This experiment demonstrates the successful loading and release of the LT680 dye, that can be used for studying nanoparticle uptake and subsequent release of drug from within the cells *in vitro*.

Photothermal efficiency calculation: The photothermal conversion efficiency for $mSiO_2$-PDA was measured using a method reported previously.[224] To obtain the temperature data, 300 µl of $mSiO_2$-PDA solution (1 mg/ml) was irradiated with 808 nm laser (power 0.4 W, power density 14 mW/mm^2) for six minutes so that the solution temperature reaches steady-state. Laser was

turned off at six minutes and solution temperature was monitored for another six minutes to follow the cooling kinetics. Same test was carried out with deionized water.

The energy input by nanoparticles is given by:[224]

$$Q_{NP} = I(1 - 10^{-A_{808}})\eta \quad \text{(S4.1)}$$

Where I is laser power (W), A_{808} is the nanoparticle absorbance at 808 nm and η is the photothermal conversion efficiency.

The heat dissipated to the environment is given by:

$$Q_{loss} = hS(T - T_a) \quad \text{(S4.2)}$$

Where h is the heat transfer coefficient (W/cm.K), S is the surface area (cm^2) and T_a is the ambient temperature (K).

When the steady-state condition is reached, the energy input is equal to energy output:

$$Q_{NP} + Q_w = Q_{loss-max} = hS(T_{max} - T_a) \quad \text{(S4.3)}$$

Where Q_w is the heat generated by water from laser irradiation. By combining equation 1 and 2, the photothermal conversion efficiency can be deduced to be:

$$\eta = \frac{hS(T_{max} - T_a) - Q_w}{I(1 - 10^{-A_{808}})} \quad \text{(S4.4)}$$

In order to calculate the hS, a non-dimensional temperature θ is defined as:

$$\theta = \frac{T - T_a}{T_{max} - T_a} \quad \text{(S4.5)}$$

A typical time constant could be written as follows:

$$\tau_s = \frac{\sum_i m_i c_i}{hS} \tag{S4.6}$$

Where m is the weight and c is the specific heat capacity. Using conservation of energy during the cooling stage and equations (5) and (6):

$$dt = -\tau_s \frac{d\theta}{\theta} \tag{S4.7}$$

By integrating the above equation:

$$t = -\tau_s \ln(\theta) \tag{S4.8}$$

This means, the system's time constant is the slope of the linear fit between time and $-\ln(\theta)$ during the cooling stage.

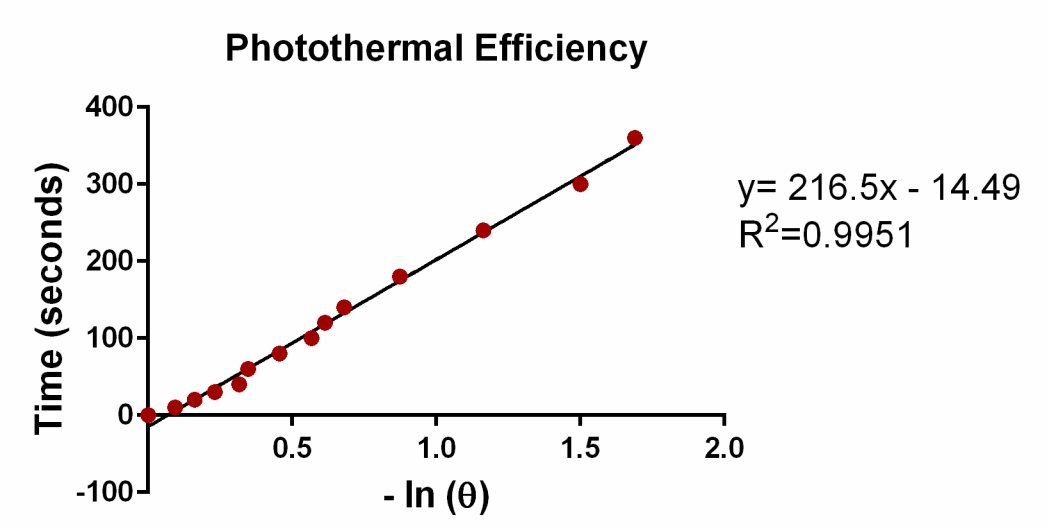

From the slope of the above graph, we obtain $\tau_s = 216.52$ sec. The hS is calculated using equation (6), giving $hS = 0.00582$ (W/K). Then, Q_w is calculated using equation below:

$$Q_w = hS\,(T_{maxW} - T_a) \tag{S4.9}$$

Considering that the temperature rise for deionized water is 0.5 K, Q_w is calculated to be 0.0029 W.

Then, the photothermal conversion efficiency of the nanoparticles is calculated by using equation (4). Laser power is 0.4 W, $A_{808} = 0.678$ and with $T_{max} - T_a = 31.4\,K$, we calculate the photothermal conversion efficiency $\eta = 56.8\ \%$.

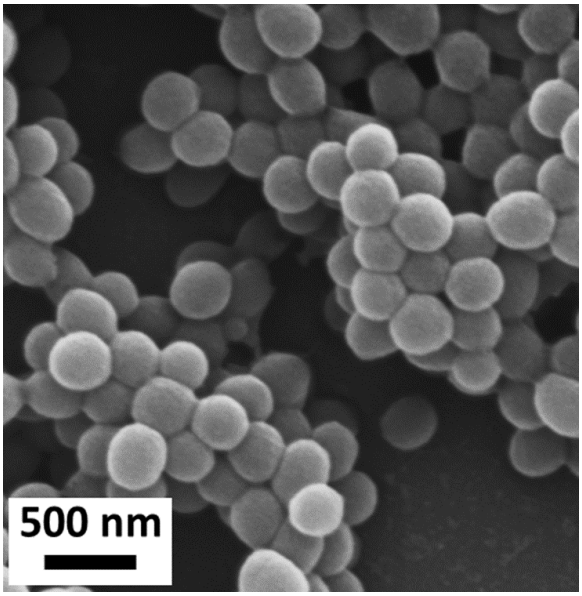

Figure S4. 1 SEM image of as-prepared silica-coated PDA nanoparticles before removing the pore-template (CTAB).

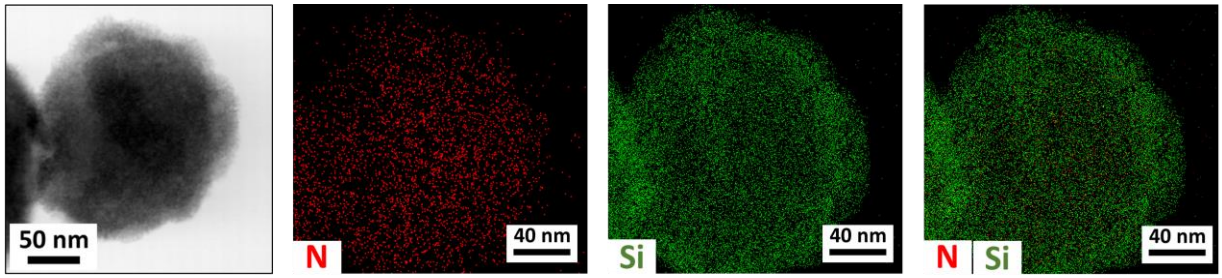

Figure S4. 2 HRTEM image of PDA@mSiO$_2$ nanoparticles and corresponding EDS elemental mapping for N and Si, showing the presence of PDA core and silica shell.

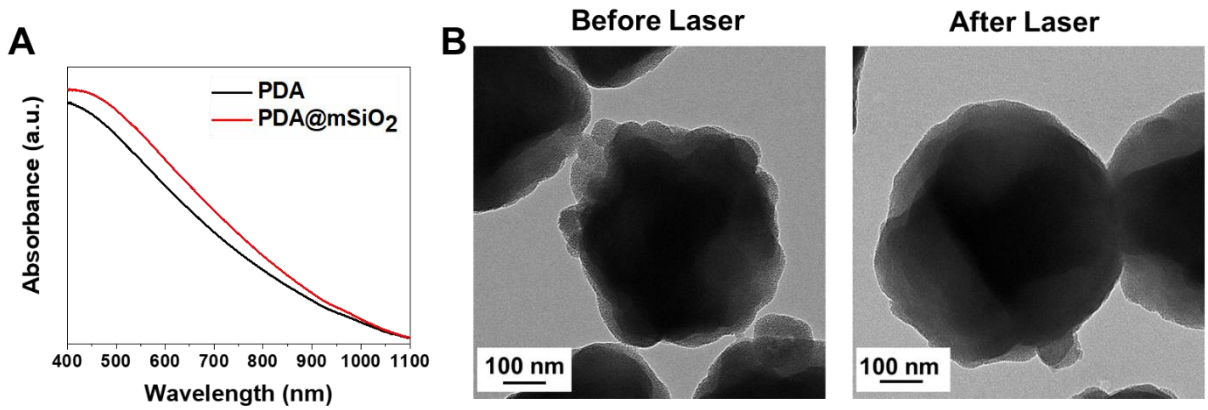

Figure S4. 3 (A) Absorbance spectra of PDA and PDA@mSiO$_2$ nanoparticles. (B) TEM images of the PDA@mSiO$_2$ nanoparticles before and after 10 minutes laser treatment.

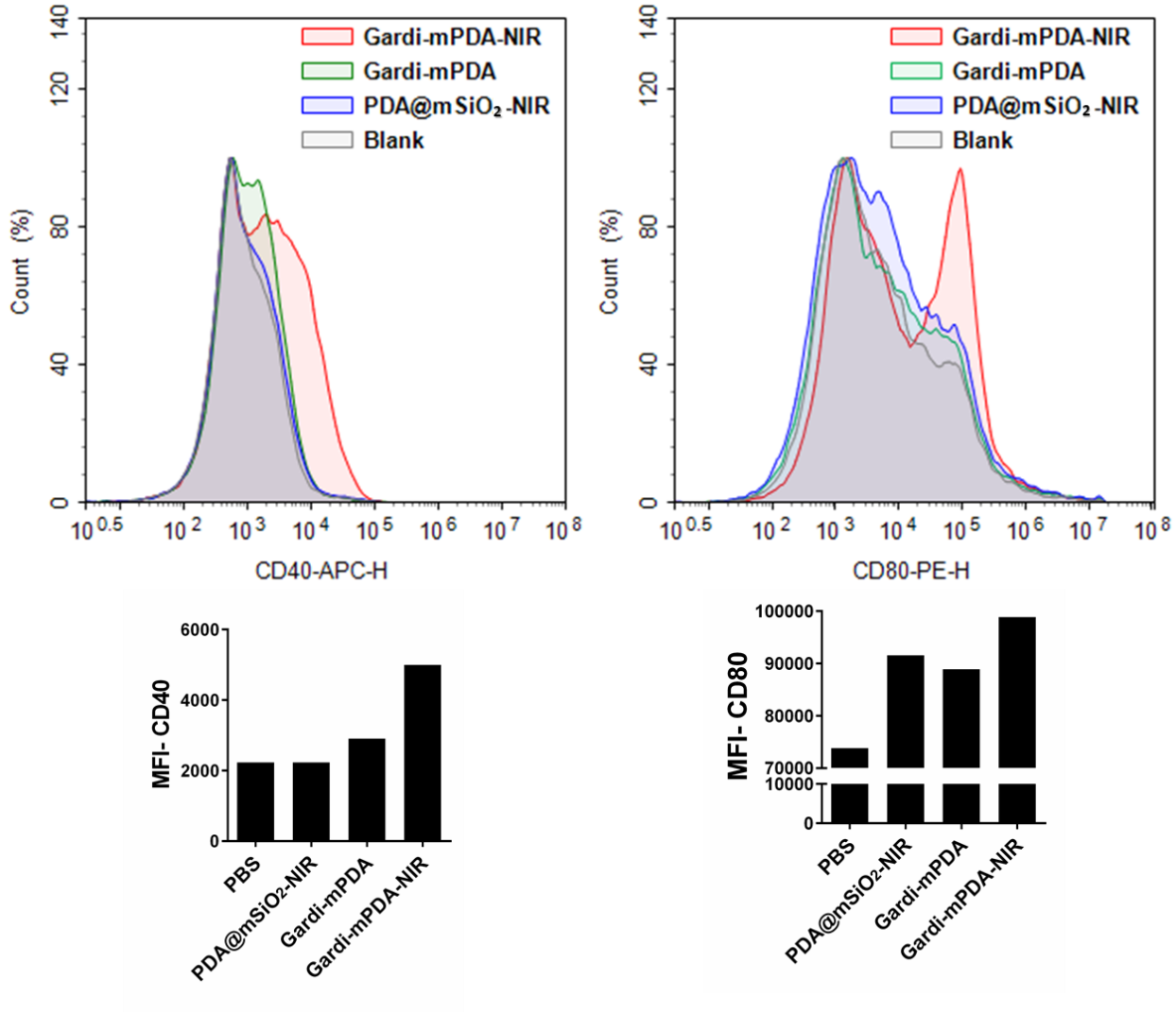

Figure S4. 4 *In vitro* maturation of BMDCs indicated by upregulation of maturation markers: CD40, and CD80.

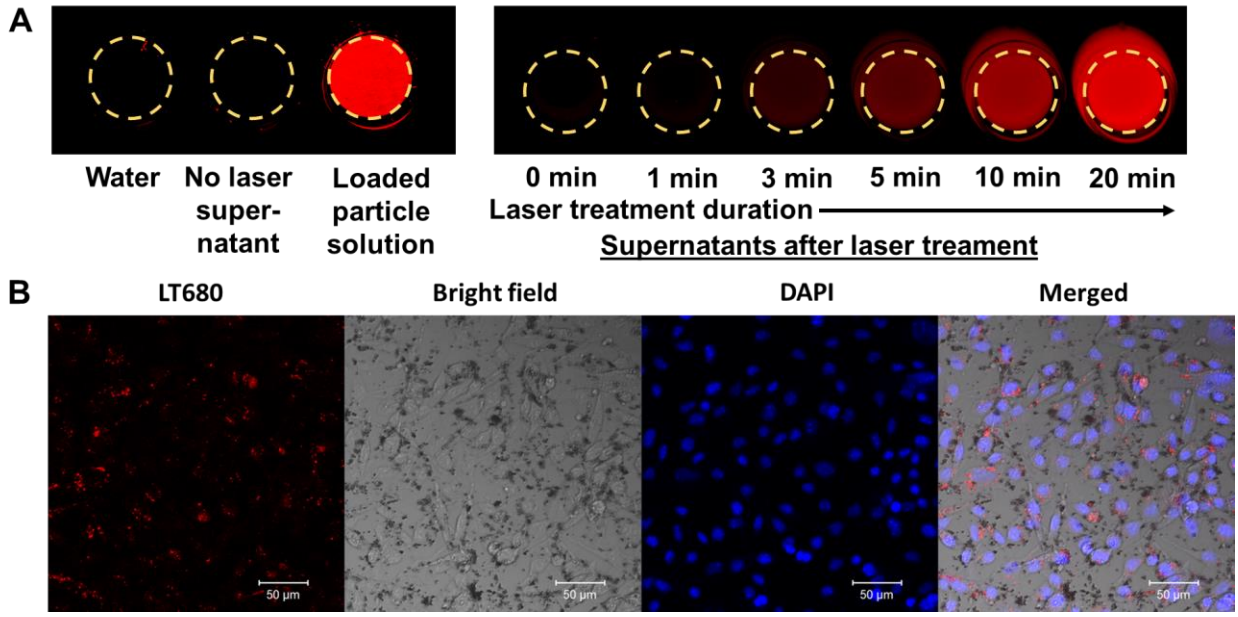

Figure S4. 5 (A) (Left) FL images of the water (control), supernatant of loaded particles and LT680 loaded PDA@mSiO$_2$ particles showing efficient dye loading without free dye in solution. (right) NIR-triggered release of LT680 dye from PDA@mSiO$_2$ versus laser irradiation time (808 nm, 14 mW/mm^2). (B) Nanoparticle uptake by cancer cells. Confocal fluorescence images of B16-F10 cells incubated with LT680-mPDA nanoparticles. Scale bar: 50 µm.

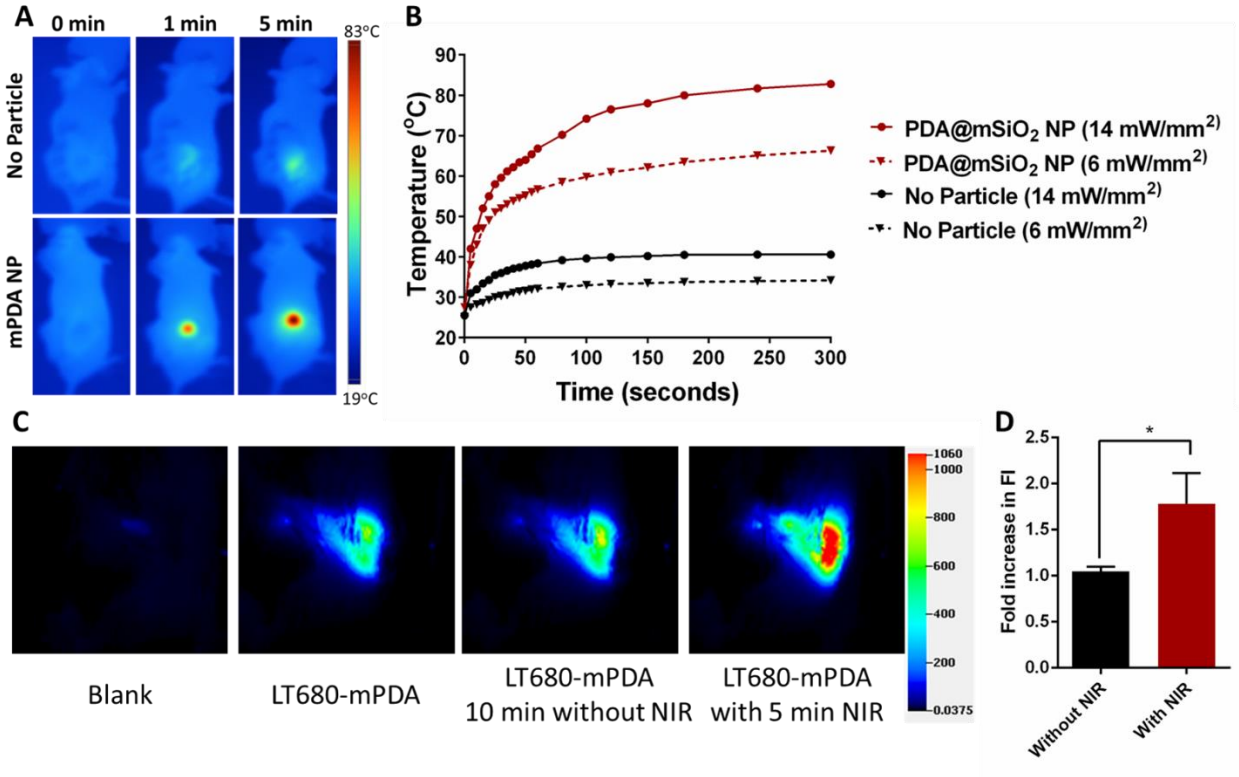

Figure S4. 6 (A) IR images of the mouse melanoma model when tumor was ablated with laser (808 nm, 14 mW/mm^2) with and without PDA@mSiO$_2$ nanoparticle injection. (B) Changes in local tumor temperature when ablated with different laser power densities with and without PDA@mSiO$_2$ nanoparticle injection. (C) Fluorescence images of mouse tumor acquired before injection (blank) and after LT680-loaded mPDA injection (LT680-mPDA and LT680-mPDA 10 minute without NIR) and after 5 minutes of NIR treatment (LT680-mPDA with 5 min NIR). (D) Fold increase in fluorescence intensity (FI) with and without NIR treatment (n=3). Data represented as mean ± SD. * $p<0.05$ by Unpaired t test with Welch's correction.

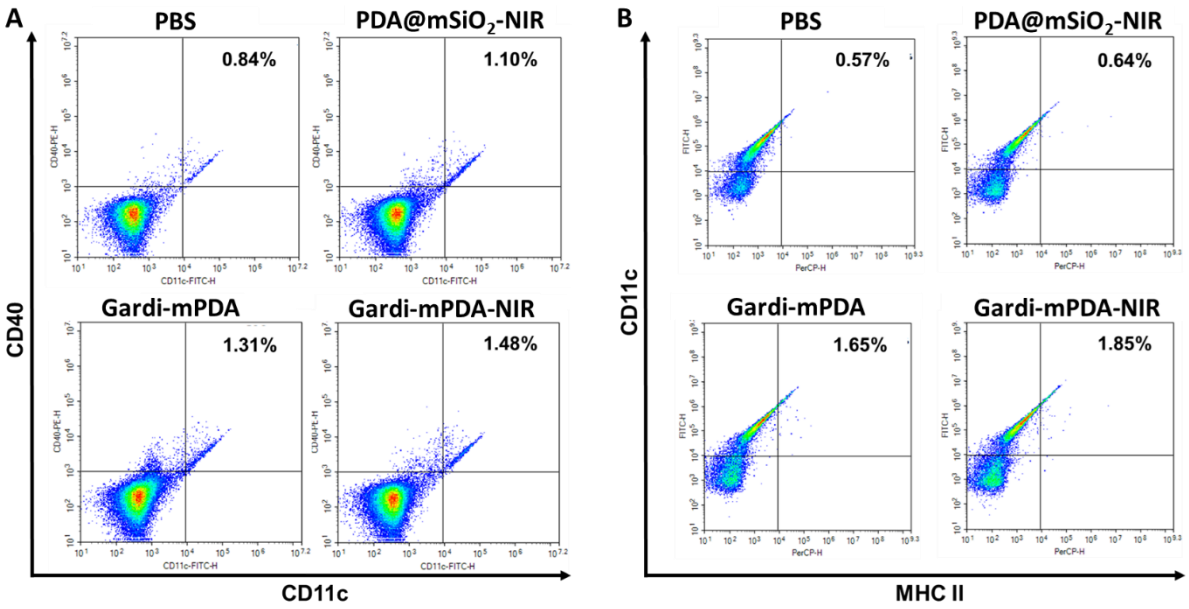

Figure S4. 7 Relative populations and activation status of immune cells in tumor draining lymph node at day 16. Representative flow cytometry plots of (A) $CD11c^+$ $CD40^+$ dendritic cells, (B) $CD11c^+$ $MHCII^+$ dendritic cells. Percentage positive cells are displayed on top right corner.

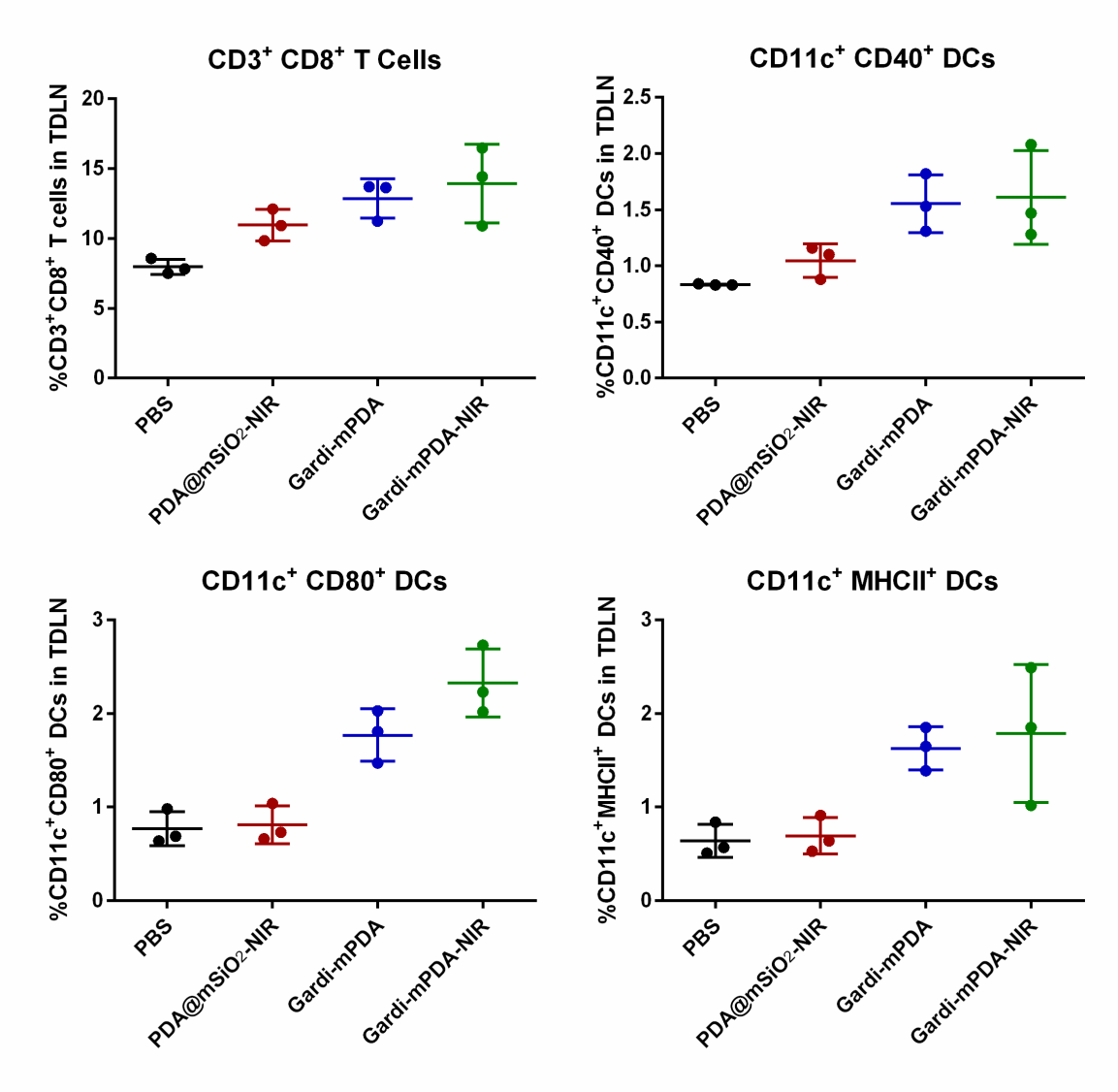

Figure S4. 8 Percentage of different immune cells present in tumor draining lymph node (n=3). Data represented as mean ± SD.

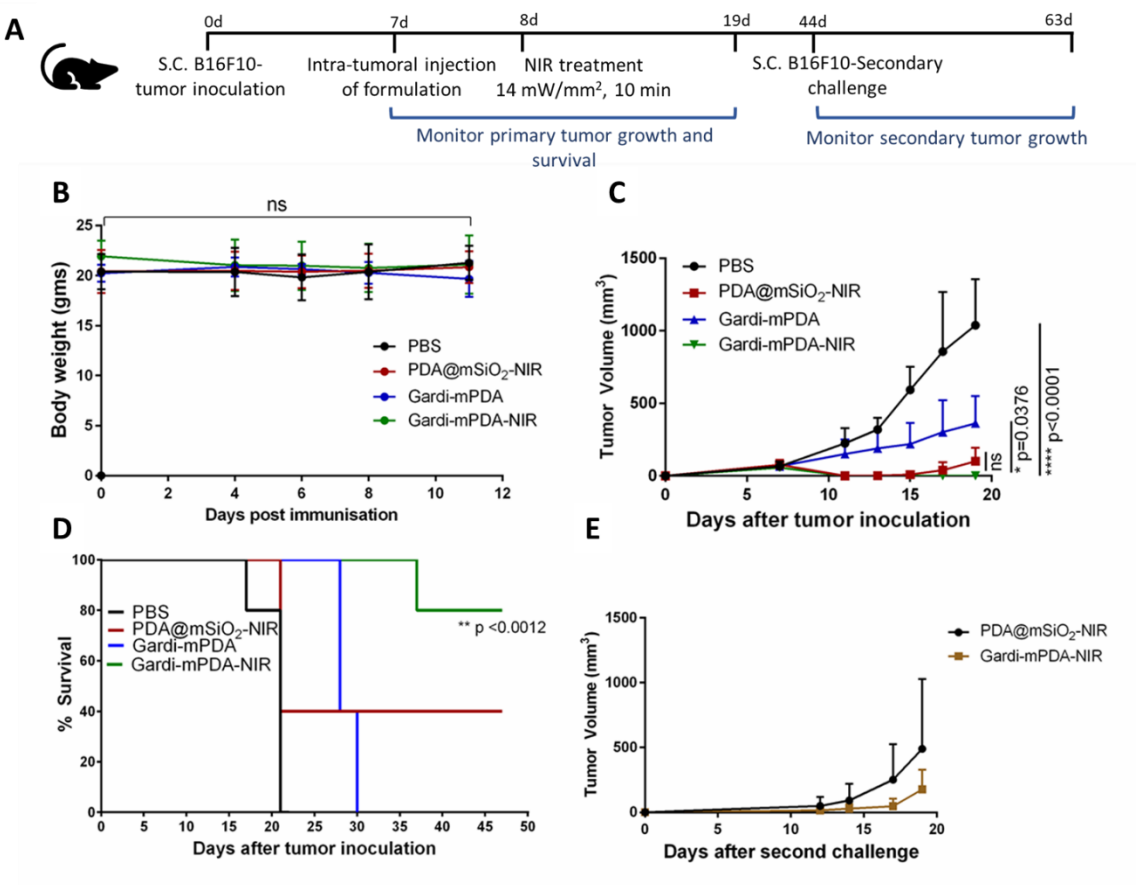

Figure S4. 9 Therapeutic effect of increasing NIR treatment duration to 10 minutes. (A) Timeline of experiment. (B) *In vivo* toxicity of gardi-mPDA and 10 minute NIR assessed by change in body weight of the mice, (C) tumor growth curves, (D) survival curve of mice given different treatments (n=5). (E) Tumor volume after secondary challenge in mice surviving after gardi-mPDA-NIR treatment and PDA@$mSiO_2$-NIR (n=2). Data represented as mean ± SD. * $p<0.05$, ** $p<0.01$ and **** $p<0.0001$ by one-way ANOVA with Tukey's posttest and Log-rank (Mantel-Cox) test for survival curve.

Appendix 4

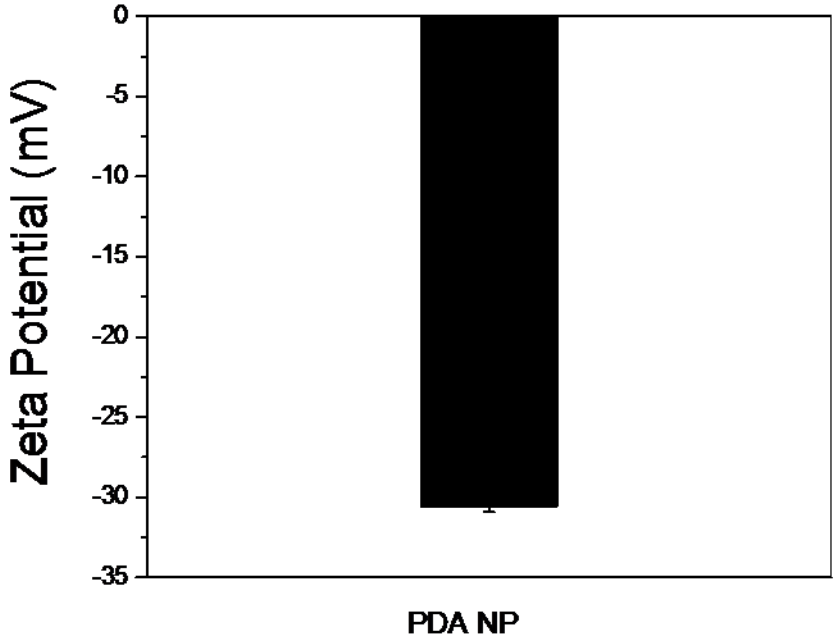

Figure S5. 1 Zeta potential measurements of Polydopamine nanoparticles in PBS, pH=7.4.

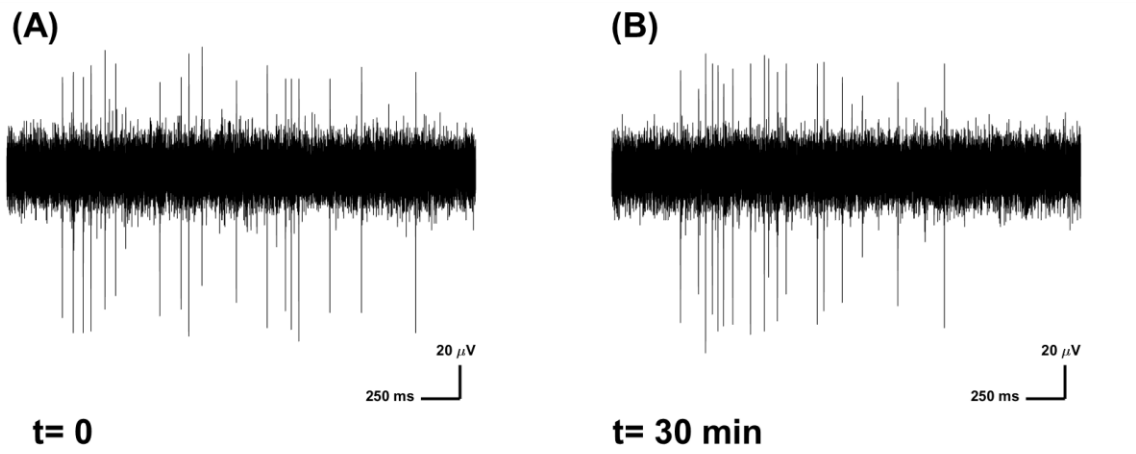

Figure S5. 2 A single trace of spike recording at half an hour interval. Neurons were not treated with PDA NP and are not subject to any external stimulation

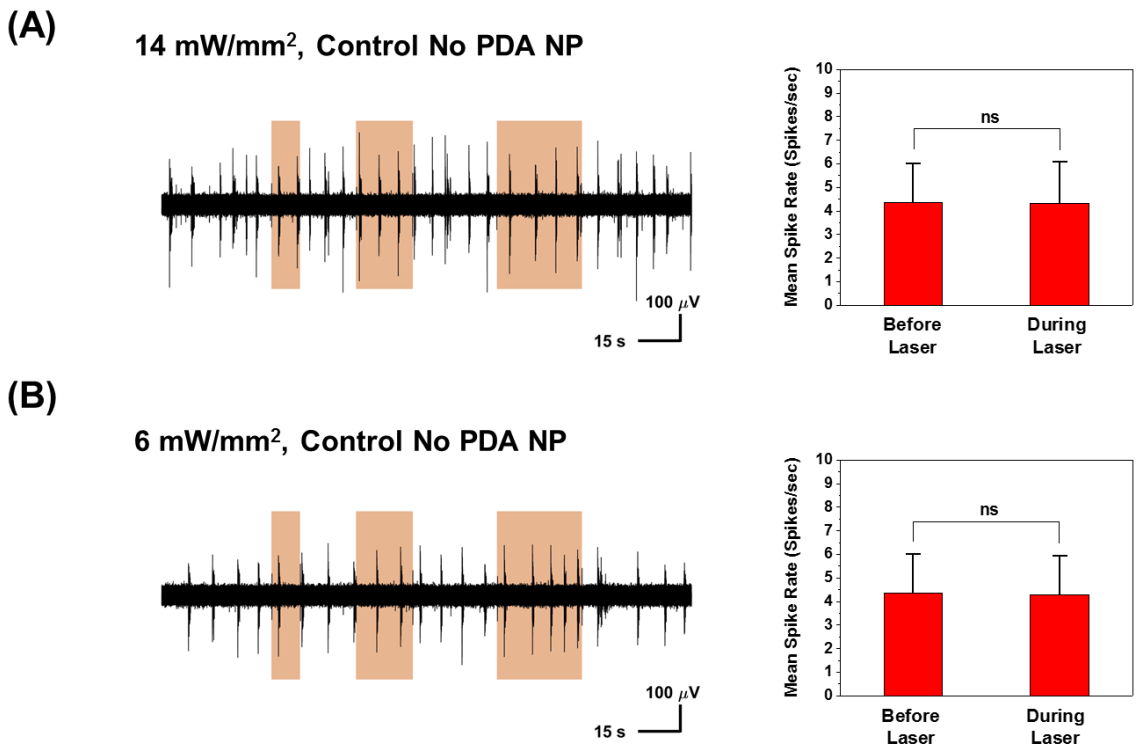

Figure S5. 3 Control experiments: Effect of laser irradiation on neuron activity without PDA NP treatment. A single trace of spike recording (left) and mean spike rate (right). Unpaired Two-samples t-test; panel (A): p= 0.7928, n=32, panel (B): p= 0.661927, n=38.

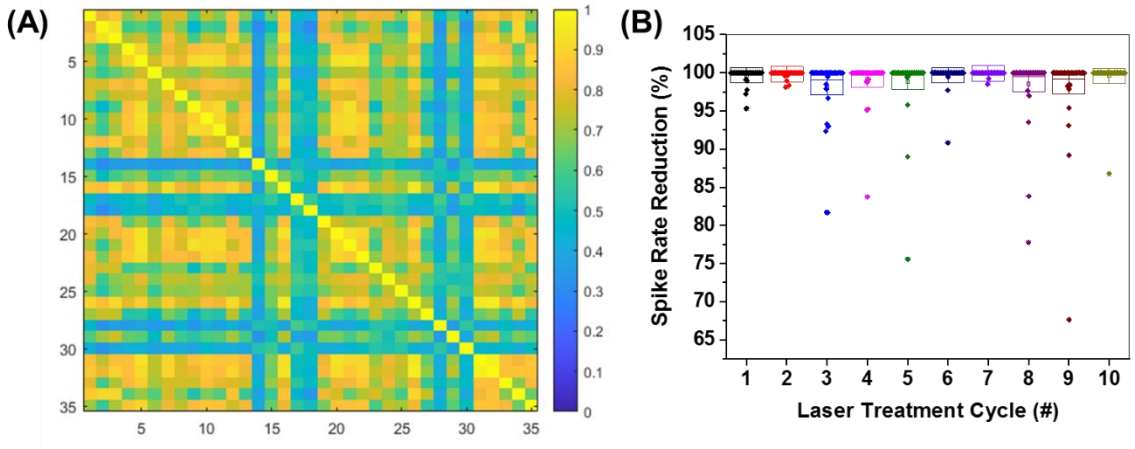

Figure S5. 4 (A) Correlation coefficient matrix for repeated laser photothermal stimulation in presence of PDA NP. Highly correlated spike activity across the culture during the laser application indicates the culture wide and universal effect of the treatment. (B) Box plot displays the spike reduction percentage during the photothermal stimulation for each cycle and the its distribution across diffeent electrodes. Close to 1oo percent average activity reduction and low scattering across electrodes demonstrates the culture-wide effectiveness of the photothermal stimulation.

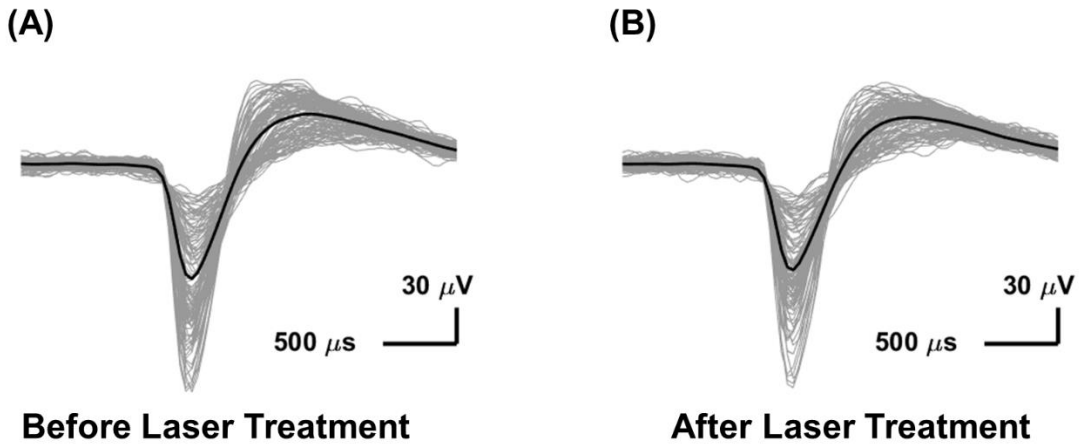

Figure S5. 5 Overlaid waveform of hippocampal neurons treated with PDA NP, before and after NIR laser irradiation. Data were collected for laser power density of 6 $mW.mm^{-2}$ where neuron activities were completely suppressed during NIR irradiation. Panel (A) shows the spike cutouts before the application of laser and panel (B) shows the spike cutouts after the laser irradiation was finished.

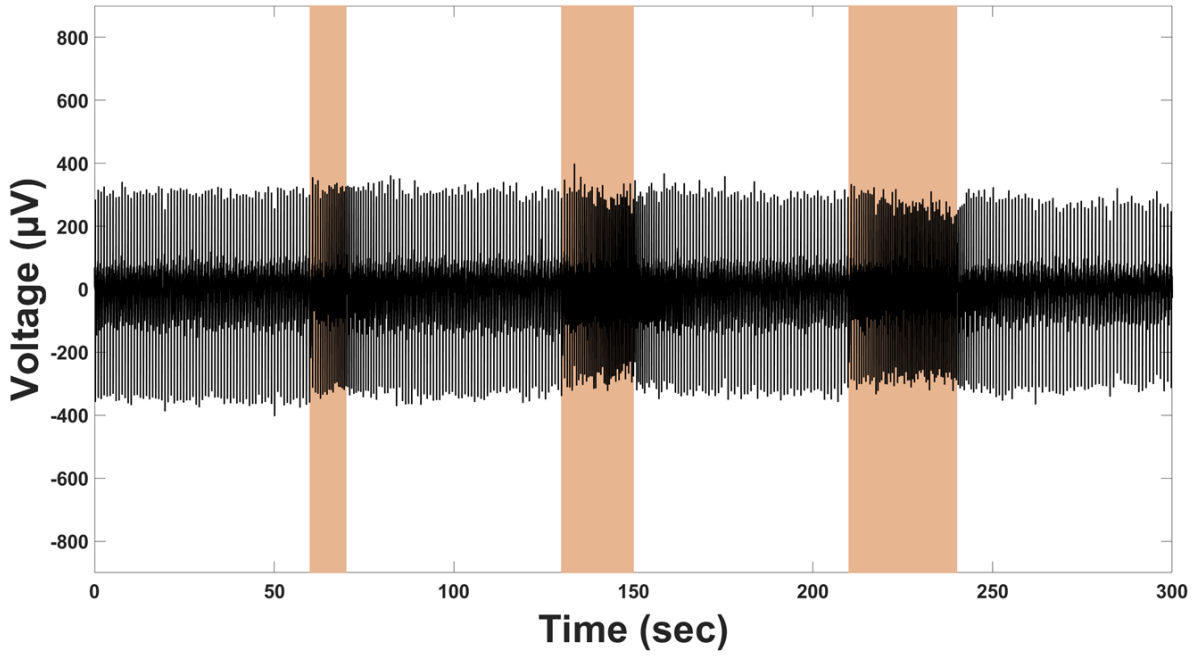

Figure S5. 6 The full trace of field potential recording of iPS-derived cardiomyocytes on MEA system. The iPS-CMs were seeded on MEA recording probe for 3 days until stable field potential was observed. The iPS-CMs was treated with PDA nanoparticle for 24 hours and washed off before recording. The full recording was 300-seconds long. The 808 laser was turned on for duration of 10, 20 and 30 seconds with power density of 14 $mW.mm^{-2}$.

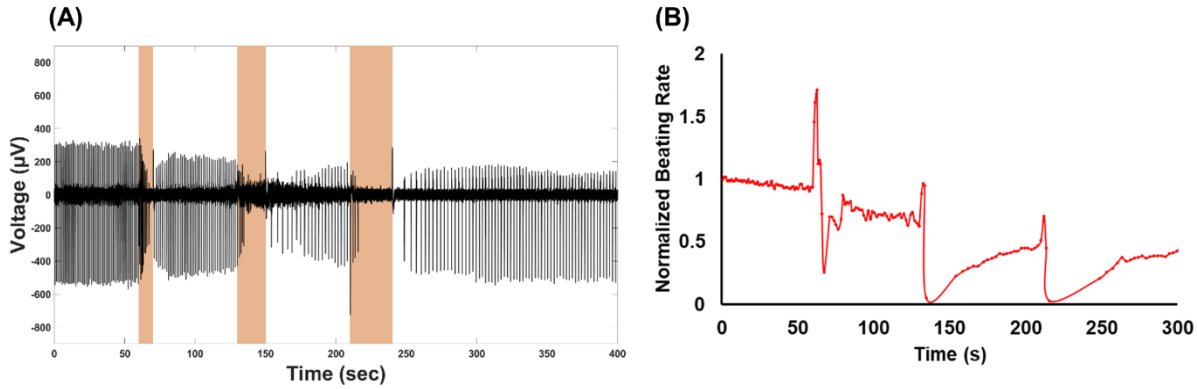

Figure S5. 7 Extreme heat effect on iPS-derived cardiomyocytes. (A) The full trace of field potential recording of iPS-CM treated with PDA nanoparticle for 24 hours and heated by 808 laser at power density of 25 $mW.mm^{-2}$. (B) The normalized beating rate of iPS-CMs showed the beating rate increased at the beginning of laser heating, but ceased beating shortly after increasing, experiencing complete stop of beating during the laser treatment. The activity recovered after the laser was turned off, and the frequency of the beating changed afterward.

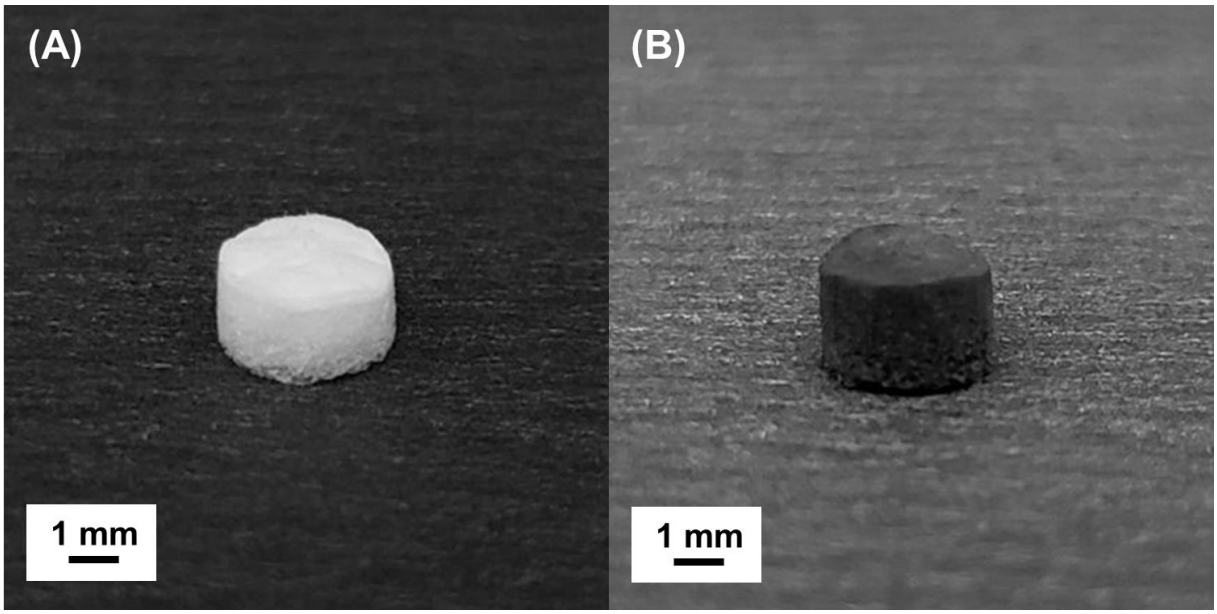

Figure S5. 8 Optical images of (A) pristine collagen foam and (B) collagen foam modified with PDA NP (dark color comes from PDA NP immobilization on collagen surface).

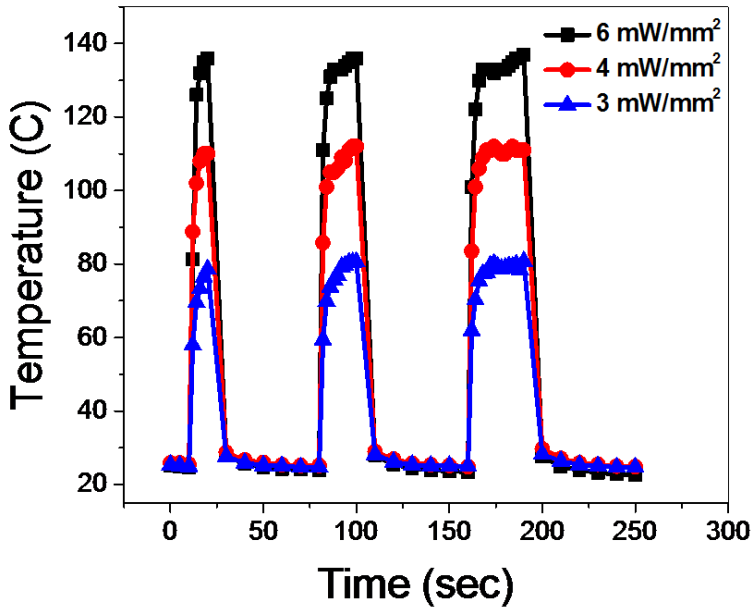

Figure S5. 9 Temperature changes of collagen foam + PDA NP in dry state at different laser power densities (808 nm laser duration for 10, 20 and 30 seconds).

Curriculum Vitae

Hamed Gholami Derami

EDUCATION

2020 **Ph.D.**, Mechanical Engineering and Materials Science, Washington University in St. Louis, St. Louis, Missouri, USA

Advisor: Professor Srikanth Singamaneni

Dissertation: Multifunctional Polydopamine Nanomaterials for Biomedical and Environmental Application (Dec 2020)

2015 **M.S.**, Mechanical Engineering, Southern Illinois University Edwardsville, Edwardsville, Illinois, USA

2013 **B.S.**, Mechanical Engineering, Sharif University of Technology, Tehran, Iran

RESEARCH EXPERIENCE

2015-2020 **Graduate Research Assistant,** Washington University in St. Louis, St. Louis, USA

2014-2015 **Graduate Research Assistant**, Southern Illinois University, Edwardsville, USA

2009-2013 **Undergraduate Research Assistant**, Sharif University of Technology, Tehran, Iran

PUBLICATIONS

Refereed Journal Publications

1. Seth, Anushree, **Hamed Gholami Derami**, Prashant Gupta, Zheyu Wang, Priya Rathi, Rohit Gupta, Thao Cao, Jeremiah J. Morrissey, and Srikanth Singamaneni.

"Polydopamine–Mesoporous Silica Core–Shell Nanoparticles for Combined Photothermal Immunotherapy." ACS applied materials & interfaces 12, no. 38 (2020): 42499-42510. (**equal contribution**)

2. **Gholami Derami, Hamed**, Prashant Gupta, Rohit Gupta, Priya Rathi, Jeremiah J. Morrissey, and Srikanth Singamaneni. "Palladium Nanoparticle-Decorated Mesoporous Polydopamine/Bacterial Nanocellulose as a Catalytically Active Universal Dye Removal Ultrafiltration Membrane." *ACS Applied Nano Materials* (2020).

3. **Gholami Derami, Hamed**, Qisheng Jiang, Deoukchen Ghim, Sisi Cao, Yatin J. Chandar, Jeremiah J. Morrissey, Young-Shin Jun, and Srikanth Singamaneni. "A robust and scalable polydopamine/bacterial nanocellulose hybrid membrane for efficient wastewater treatment." *ACS Applied Nano Materials* 2, no. 2 (2019): 1092-1101.

4. **Hamed Gholami Derami**, Prashant Gupta, Kuo-Chan Weng, Anushree Seth, Rohit Gupta, Jonathan R. Silva, Barani Raman*, and Srikanth Singamaneni*, "Reversible Photothermal Modulation of Electrical Activity of Excitable Cells using Polydopamine Nanoparticles ", In preparation.

5. Zhu, Yaguang; **Gholami Derami, Hamed**; Gupta, Prashant; Gupta, Rohit; Singamaneni, Srikanth; Jun, Young-Shin, "Ionic Surface Propensity Controls pH in Nanopores", Submitted paper. (**equal contribution**)

6. **Derami, Hamed Gholami**, Ravindra Vundavilli, and Jeff Darabi. "Experimental and computational study of gas bubble removal in a microfluidic system using nanofibrous membranes." Microsystem Technologies 23, no. 7 (2017): 2685-2698.

7. Jiang, Qisheng, **Hamed Gholami Derami**, Deoukchen Ghim, Sisi Cao, Young-Shin Jun, and Srikanth Singamaneni. "Polydopamine-filled bacterial nanocellulose as a biodegradable interfacial photothermal evaporator for highly efficient solar steam generation." Journal of Materials Chemistry A 5, no. 35 (2017): 18397-18402.

8. Mamouri, S. Jahangiri, **H. Gholami Derami**, M. Ghiasi, M. B. Shafii, and Z. Shiee. "Experimental investigation of the effect of using thermosyphon heat pipes and vacuum glass on the performance of solar still." Energy 75 (2014): 501-507.

9. Masterson, Adrianna N., Thakshila Liyanage, Hristos Kaimakliotis, **Hamed Gholami Derami**, Frédérique Deiss, and Rajesh Sardar. "Bottom-Up Fabrication of Plasmonic Nanoantenna-Based High-throughput Multiplexing Biosensors for Ultrasensitive Detection of microRNAs Directly from Cancer Patients' Plasma." *Analytical Chemistry* (2020).

10. Luan, J., Seth, A., Gupta, R., Wang, Z., Rathi, P., Cao, S., **Derami, H.G.,** Tang, R., Xu, B., Achilefu, S. and Morrissey, J.J., 2020. Ultrabright fluorescent nanoscale labels for the femtomolar detection of analytes with standard bioassays. Nature Biomedical Engineering, 4(5), pp.518-530.

11. Kolluru, Chandana, Rohit Gupta, Qisheng Jiang, Mikayla Williams, **Hamed Gholami Derami**, Sisi Cao, Richard K. Noel, Srikanth Singamaneni, and Mark R. Prausnitz. "Plasmonic Paper Microneedle Patch for On-Patch Detection of Molecules in Dermal Interstitial Fluid." ACS sensors 4, no. 6 (2019): 1569-1576.

12. Cao, Sisi, Qisheng Jiang, Xuanhao Wu, Deoukchen Ghim, **Hamed Gholami Derami**, Ping-I. Chou, Young-Shin Jun, and Srikanth Singamaneni. "Advances in solar evaporator materials for freshwater generation." Journal of Materials Chemistry A 7, no. 42 (2019): 24092-24123.

13. Luan, Jingyi, Jeremiah J. Morrissey, Zheyu Wang, **Hamed Gholami Derami**, Keng-Ku Liu, Sisi Cao, Qisheng Jiang et al. "Add-on plasmonic patch as a universal fluorescence enhancer." Light: Science & Applications 7, no. 1 (2018): 1-13.

14. Xu, T., Jiang, Q., Ghim, D., Liu, K.K., Sun, H., **Derami, H.G**., Wang, Z., Tadepalli, S., Jun, Y.S., Zhang, Q. and Singamaneni, S., 2018. Catalytically Active Bacterial Nanocellulose-Based Ultrafiltration Membrane. Small, 14(15), p.1704006.

15. Liu, Keng-Ku, Qisheng Jiang, Clayton Kacica, **Hamed Gholami Derami**, Pratim Biswas, and Srikanth Singamaneni. "Flexible solid-state supercapacitor based on tin oxide/reduced graphene oxide/bacterial nanocellulose." RSC advances 8, no. 55 (2018): 31296-31302.

PATENTS

1. Majid Ashoury , Hamed Gholami Derami, MB Shafii, MH Saidi “ Method and apparatus of piston micro-pump by using magnetic stimulation of Ferrofluid” I.R.I Patent Application Serial No. 72462 , 2011.